MODELING DWARF GALAXIES OF THE LOCAL VOLUME WITH THE SEMI-ANALYTIC MODEL GALACTICUS

by

SACHI WEERASOORIYA

Bachelor of Science, 2018
Midwestern State University
Wichita Falls, TX

Master of Science, 2020
Texas Christian University
Fort Worth, TX

Submitted to the Graduate Faculty of the
College of Science and Engineering
Texas Christian University
in partial fulfillment of the requirements
for the degree of

Doctor of Philosophy

August 2023

MODELING DWARF GALAXIES OF THE LOCAL VOLUME WITH THE SEMI-ANALYTIC MODEL GALACTICUS

by

Sachi Weerasooriya

Dissertation Approved:

Dr. Mia Sauda Bovill

Dr. Andrew Benson

Dr. Peter Frinchaboy

Dr. Kat Barger

Dr. Hana Dobrovolny

For The College of Science and Engineering

Acknowledgments

To my ever-loving sisters Udayanthi Weerasooriya and Sandamali Weerasooriya, who have always been there for me and whose path I walk, and my non-biological sister Binita Hona who guided me towards Astronomy

First and foremost, I would like to thank my advisor Dr. Mia Sauda Bovill, who has guided me through my journey as a graduate student. She has taught me how to be a good researcher, science communicator, and a kind and supportive colleague in Astronomy. She also showed me how to incorporate my science illustration skills to strengthen my science communication and understanding of concepts. At times when I have struggled as an international student living alone, she has always been there to support me and comfort me. For that, I am forever grateful! Special thank you to my undergraduate advisor Dr. Jacqueline Dunn who first introduced me to research Dwarf Galaxies and motivated me to connect art with Physics. I am grateful for her guidance and support throughout this journey.

Thank you, Dr. Andrew Benson, for actively helping me to understand Galacticus and giving me feedback on countless questions I have asked. In times when computational resources limited us, he has kindly run Galacticus models for us. Over the last few years, Dr. Benson has been an extremely helpful mentor in the progress of my thesis project. He has always been responsive, answering questions regarding the installation and usage of Galacticus, even debugging as necessary, and providing additional control of parameters. I would also like to thank Dr. Matthew A. Taylor for helping us with the project on Centaurus A and giving us valuable input from the observer's perspective and access to SCABS data. Thank you, my department committee: Dr. Peter Frinchaboy, Dr. Kat Barger, and Dr. Hana Dobrovolny, for taking the time to review this dissertation to make it better.

Thank you, Dr. Robyn Sanderson, for adopting me during conferences where my advisor could not attend and making me feel welcome and supported. I am also thankful to Dr. Tjitske Starkenburg, Dr. Helmer Koppelman, and Dr. Kathryn Johnston for mentoring me at Galactic Dynamic Summer School 2021 at CCA on stellar streams and Dr. Emily Cunningham for her input and guidance for the continuation of the project.

My heartiest gratitude goes to Mrs. Jean Sauda Bovill and Binita Hona for carefully proofreading my dissertation and my friend Sophia Lilleengen for being a great dissertation writing companion on Zoom sessions. I would also like to thank all the present and past graduate students in the Department of Physics and Astronomy at Texas Christian University, particularly Alessa I. Wiggins, Amy Ray, Taylor Spoo, and Natalie Myers. Special thanks to my best friend Shermali Ratnasinghe for keeping me sane for the past 18 years and Christian Douglas for being a supportive ex-boyfriend. I owe a tremendous amount of gratitude to my parents Muthu Weerasooriya, and Wijeratne Weerasooriya, my sister Udayanthi Weerasooriya, and my brothers Rasika Kumarasinghe and Sachintha

Gurudeniya for supporting me to come to the USA 9 years ago to fulfill my dreams. Thank you for taking care of me despite being thousands of miles apart. I am also grateful for the support of my uncle Tissa Weerasooriya, aunts Bandaramenike Atempawala and Theja Senevirathne.
Last but not least, I am thankful to my role model, my sister Sandamali Weerasooriya whose path I followed to become an Astrophysicist. Finally, I want to thank my high school Physics teacher, Mrs. Gayathri de Silva, for always encouraging my dreams of becoming an Astronomer.

The content of this dissertation is gathered from three papers, Weerasooriya et al. (2023), Weerasooriya et al. (in prep. a;b). Parts of this work are drawn verbatim from these three papers, where Weerasooriya et al. (2023) is accepted to Astrophysical Journal (ApJ) and Weerasooriya et al. (in prep. a;b) will be submitted to ApJ.

Parts of Chapter 1 are verbatim from the introductions of Weerasooriya et al. (2023; in prep. a;b). Parts of Chapter 2 is written verbatim drawn from simulations sections of the same papers. Chapters 3, 4, and 5 draws verbatim from Weerasooriya et al. (2023).

Contents

List of Figures

List of Tables

List of Abbreviations

Active Galactic Nuclei	AGN
Cenaturus A	Cen A
Circum Galactic Medium	CGM
Cold Dark Matter	CDM
Dark Energy Survey	DES
Extended Press Schechter	EPS
Milky Way	MW
Nine-Year Wilkinson Microwave Anisotropy Probe	WMAP9
Local Group	LG
Local volume	LV
Ordinary Differential Equation	ODE
Semi-Analytic Model	SAM
Sloan Digital Sky Survey	SDSS
Star Formation History	SFH
Star Formation Rate	SFR
Super Massive Blackhole	SMBH
Ultra Faint Dwarf	Ultra Faint Dwarf

Chapter 1

Introduction

Dwarf galaxies are the most common and ubiquitous galaxies in the universe. Their shallow gravitational potential wells make them extremely susceptible to internal and external feedback (*e.g.*, Dekel and Silk 1986, Thoul and Weinberg 1996, Benson et al. 2002, Okamoto et al. 2010), making them excellent probes of the internal and external physical processes governing star formation. Dwarfs are galaxies that are fainter than $M_B \sim -16\ mag$ in absolute B band magnitudes (Tammann 1994) [1]. They are very small in both size and mass, at least ten thousand times smaller than the size of the Milky Way. [2] Large galaxies like our Milky Way are surrounded by populations of satellite dwarf galaxies (Frebel et al. 2010), and the majority of *currently* known dwarf galaxies are these satellites.

While we understand the large-scale structure of the universe relatively well, star formation physics of small-scale structures such as dwarf galaxies is poorly understood

[1] B band magnitude represents brightness in blue colors

[2] The absolute magnitude is a measure of the luminosity of a celestial object on the inverse logarithmic astronomical magnitude scale.

in a cosmological context. Our understanding of dwarf galaxies and their star formation physics is based on nearby dwarf galaxies surrounding the Milky Way (e.g. SMC, Canes Venatici, Phoenix, etc. Belokurov et al. 2007a, Zucker et al. 2006b, van de Rydt et al. 1991). However, in order to understand their nature, it is important to explore how these fundamental structures are affected by their host environment, local volume density, and mass. This work will explore the star formation physics of dwarf galaxies in different host mass environments using Semi-Analytic Models (SAMs) of galaxy formation.

1.1 Underlying Cosmology

The universe we live in today consists of medium-sized galaxies like the Milky Way to ellipticals like Centaurus A. Yet, only 4.9% of the energy density is in the baryonic, normal matter we can see. Indeed, 69.2% of the energy density of the universe is made up of dark energy and 25.2% of dark matter (Planck Collaboration et al. 2020). This means that the proportion of non-baryonic matter in the universe is much higher compared to the baryonic matter that we can observe.

Dark matter provides a framework for star formation in galaxies. Dark matter overdensities and underdensities in the universe provide a scaffolding to hold stars and gas. Quantum fluctuations frozen out during inflation, 10^{-36}s after the Big Bang, grow over time until it becomes gravitationally unstable and collapses to form gravitationally bound clumps of dark matter, called dark matter halos (Dalal et al. 2010). Baryonic gas follows gravity and thus also condenses into the gravitational potential wells of dark matter halos. Eventually, this gas formed the first stars. Light from these first stars began

the process of reionizing the hydrogen in the universe, and metals from their supernova explosions enriched their host galaxies and the surrounding intergalactic medium. The epoch of reionization lasted from approximately a billion years, from $z = 15 - 6$. This was followed by the formation of the progenitors of the modern galaxies (first galaxies).

Over the next 12.5 billion years, smaller galaxies merge to form the more massive galaxies seen today, a process called hierarchical merging. The large-scale structure formation of the universe predicted by the hierarchical structure formation based on ΛCDM (Cold Dark Matter) has been observed in filament like structure of galaxies in surveys such as 2dF Galaxy REdshift Survey (Colless 2002) and Sloan Digital Sky Survey (Albareti et al. 2017, Aguado et al. 2019, See Figure 1.1). Cosmological simulations based on ΛCDM such as Millenium (Boylan-Kolchin et al. 2009) and Illustris (Vogelsberger et al. 2014) reproduce the large scale structure.

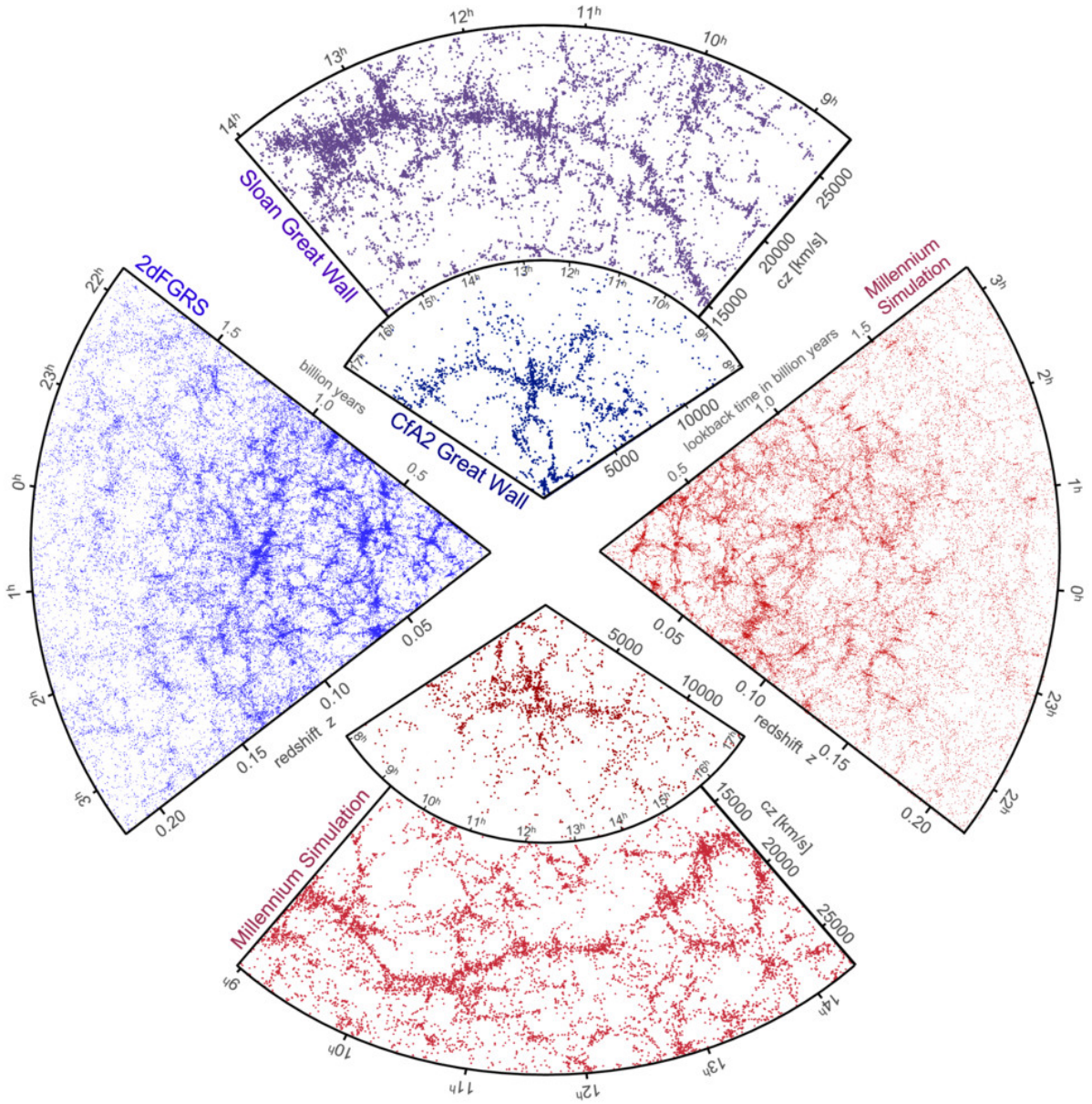

Figure 1.1: This figure shows a plot by Gerard Lemson & the Virgo Consortium (2020). It shows a comparison of galaxy distribution of the universe as predicted by the Millenium simulation with observations. The left and top slices shown in blue color are the observed galaxy distribution in our universe, gathered from the 2dF Galaxy Redshift Survey and the Sloan Digital Sky Survey respectively. Each dot inside the filaments represents a galaxy. The Earth is at the centre of the circle with distance increasing outward from the center. A redshift of 0.15 is approximately equal to a distance of 2 billion light years. Right and bottom slices of the circle colored in red shows the galaxy distribution on large scales computed using the Millennium Simulation assuming ΛCDM (Gerard Lemson & the Virgo Consortium 2020).

Dwarf galaxies are the "building blocks" of the universe. The signature of hierarchical merging is seen most strongly in the populations of dwarf satellite galaxies around more massive galaxies like our Milky Way. In fact, fossils of these first galaxies are preserved today as the faintest dwarf satellites. (Gnedin 2000, Bovill and Ricotti 2009). Satellite dwarfs around larger galaxies merge with other dwarf galaxies to form bigger structures.

Before we discuss dwarf galaxies in greater depth, we briefly provide additional information about dark matter and dark energy.

1.1.1 Dark Matter

Dwarf galaxies are the most dark matter dominated galaxies known (Mateo et al. 1998, Kleyna et al. 2001, Wilkinson et al. 2006). Dark matter content in a galaxy is determined by the dark matter mass to light ratio of a galaxy. Mass to light ratio is calculated using the central velocity dispersion and half-light radii. However, it is not possible to observe dark matter directly, as it does not interact with light or electromagnetic radiation. This odd property results in the name 'dark' matter. The presence of dark matter is inferred through its gravitational effects on the stars and gas we can observe.

Observational evidence of dark matter comes from the study of missing mass in galaxies and galaxy clusters. In 1933, Zwicky (1933) stated that the mass predicted by velocity dispersions of the galaxies of the Coma Cluster is much higher than the mass inferred by visible matter. This hinted at the mysterious matter in galaxy clusters. However, observed evidence of dark matter did not come until 29 years after. Rubin et al. (1962), Rubin and Ford (1970) found flat rotation curves implying that the circular velocities

of objects in the inner and outer parts of large spiral galaxies are the same, which is opposite to the expectation that the circular velocities are higher in the center and lower in the outskirts. Note that these rotational velocities assumed circular motion only. This implied that the total mass inferred by these velocities was much higher than the total visible mass in the galaxy, and thus there has to be some missing mass to account for the motion of stars. In addition to this, gravitational lensing also provides a method to infer the masses of galaxy clusters (Hoekstra et al. 2013). Gravitational lensing is the effect of distorted and magnified effect on clusters of galaxies. This is a result of the bending of light as the light passes through the inhomogeneous distributions of matter. Thus, it is a great way to map the distribution of dark matter in galaxy clusters. This concept was first indicated by Walsh et al. (1979) and first observed in galaxy clusters by Soucail et al. (1987). However, we do not know the nature of dark matter (Bertone et al. 2005).

1.1.2 Dark Energy

If the nature of dark matter is a mystery, dark energy is a mystery wrapped in several layers of enigma. It accounts for 68.2% of the energy density of the universe (Planck Collaboration et al. 2020) and is driving the acceleration of the expansion of the universe. Dark energy impacts the large-scale structure, formation, and evolution of the universe.

The first strong observational evidence of acceleration of the universe came with the use of type Ia supernova[3] as a standard candle in measuring the expansion of space using

[3]Type Ia supernova is a type of explosion of stars that occurs in a binary system of which one is a white dwarf star. All stars with initial masses up to 10.5 solar mass (Smartt 2009), i.e. more than 97 percent of the stars in the Galaxy, end their lives as white dwarfs (Althaus et al. 2010). All white dwarfs are less than $1.4M_{\odot}$(Chandrasekhar limit). A white dwarf will accrete mass from its binary companion to reach the Chandrasekhar limit where it will reach ignition temperature for carbon fusion. This nuclear fusion process will start a runaway reaction that will result in a supernova explosion. Type Ia supernovae

Hubble Law. Prior to this, it was believed that the expansion of the universe was slowing down. However, the supernovae observed were fainter than expected, and thus further away. The distances measured was used to calculate cosmological redshifts. Redshifts obtained using this method were tested on different cosmological models using cosmological parameters Ω_M (total matter density) and Ω_Λ (dark energy density). Analysis of the Ω_M vs. Ω_Λ plane revealed that confidence regions in this plane was consistent with an expanding universe regardless of the curvature of the universe (Perlmutter et al. 1999). Thus, it was concluded that the universe is accelerating (Riess et al. 1998, Perlmutter et al. 1999). As fundamental structures, dwarf satellite galaxies evolve under the influence of dark energy dominated by dark matter.

1.2 Dwarf Galaxies in ΛCDM

Dwarf galaxies can be divided into two types depending on their environment: isolated dwarfs and satellite dwarf galaxies. Isolated dwarf galaxies are located in regions devoid of other galaxies while satellite galaxies are found around a host galaxy. As a result, isolated dwarfs have very little external influence while the satellites are influenced by the host galaxy. Both isolated dwarfs and satellite dwarfs have been detected in our own neighborhood of the Milky Way (see Figure 1.2), Andromeda, and beyond our local neighborhood. Examples of such isolated dwarfs in the Local Group include Phoenix, Cetus, Leo T, WLM, Leo A, Tuscana, etc. and satellite galaxies include Draco, Sculptor, Carina, Fornax, Leo I/II, etc (Higgs and McConnachie 2021).

have uniform peak intrinsic luminosity making them excellent standard candles to determine distances.

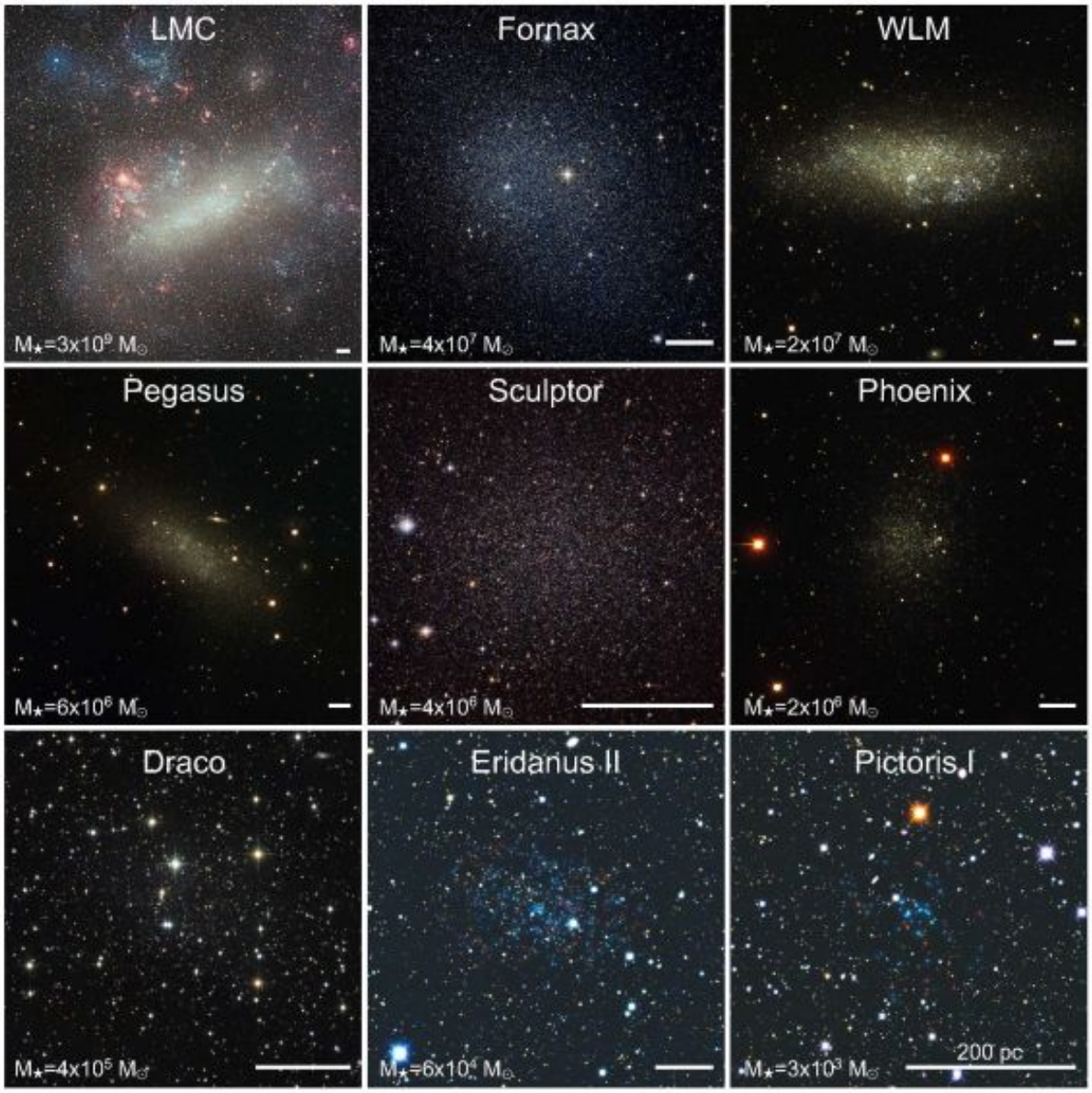

Figure 1.2: This figure shows a few dwarf galaxies of the Milky Way. LMC (Eckhard Slawik); Fornax (ESO/Digitized Sky Survey 2); WLM, Pegasus, Phoenix (Massey et al. 2007); Sculptor (ESO); Draco (Mischa Schirmer); Eridanus II, Pictoris I (Vasily Belokurov and Sergey Koposov). Picture credit: Crnojević and Mutlu-Pakdil (2021)

In this work, we focus on satellite dwarf galaxies around hosts. The sensitivity of dwarf systems to their external environment will help us get a better understanding about their host environment, and on the dependence of dwarf galaxy properties on the

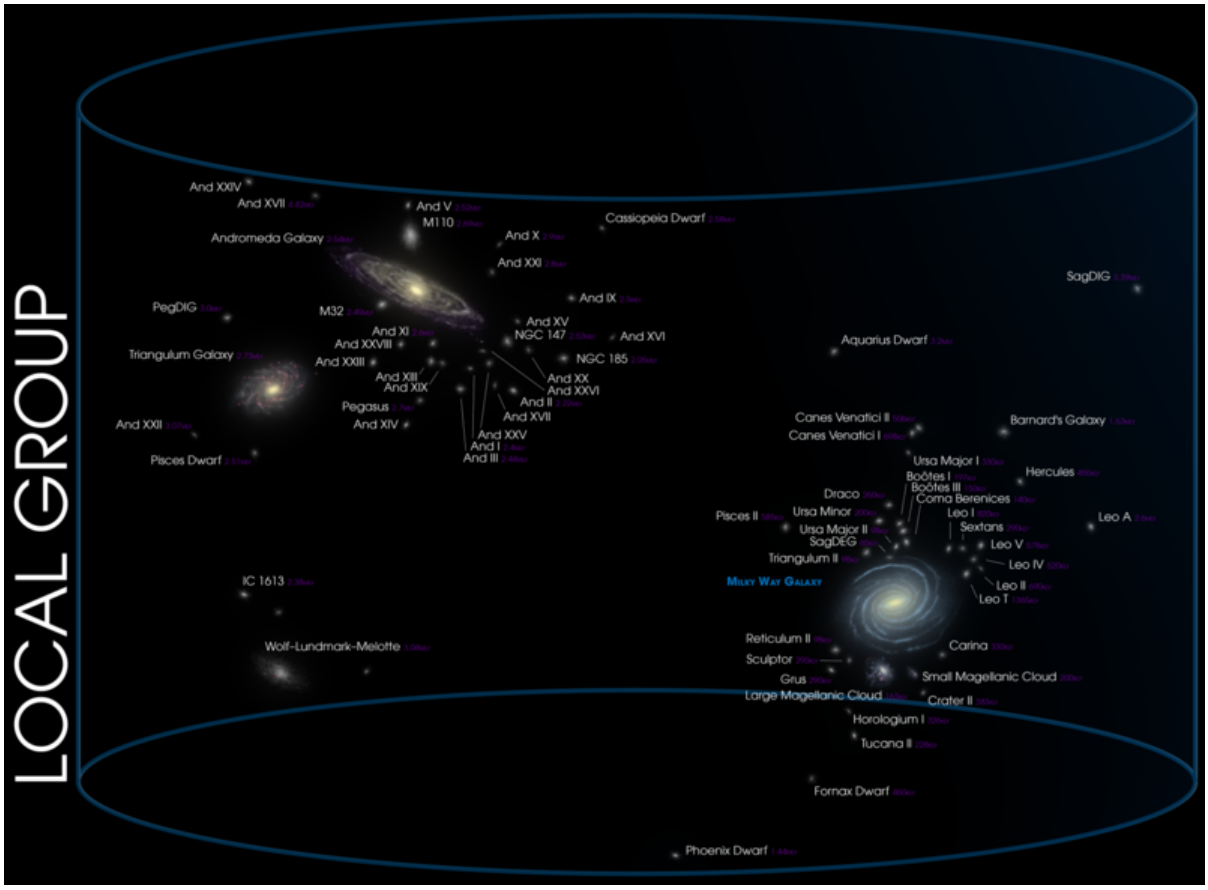

Figure 1.3: This figure shows the Local Group consisting of the Milky Way, Andromeda (M31), and M33 galaxies. Picture credit: Andrew Z. Colvin https://commons.wikimedia.org/wiki/File:06-Local$_{G}roup_{(}LofE06240).png$

environment.

1.2.1 The Local Group

Satellite dwarf galaxies are abundant in our local neighborhood, especially in and around the Milky Way and Andromeda (M31). The region that encloses the Milky Way, M31, and M33 spiral galaxies up to 1 Mpc from the center of the Milky Way (see Figure 1.3) is known as the Local Group (LG) (Mateo 1998, Karachentsev et al. 2002). The total mass of the LG is approximately $M_{LG} \geq 4 \times 10^{12}\,\mathrm{M}_{\odot}$. However, there are many discrepancies in the mass measurements among different methods (Chamberlain et al. 2023).

In the last fifteen years, the census of dwarf galaxies in the Local Group has more than doubled, approximately up to 144 (e.g. Karachentseva and Karachentsev 1998, Karachentseva et al. 1999, Whiting et al. 1997, Zucker et al. 2006a, Belokurov et al. 2006, Willman et al. 2005, Walsh et al. 2007, Irwin et al. 2007, Belokurov et al. 2007b, Drlica-Wagner et al. 2015; 2016, Torrealba et al. 2018; 2019). Observational studies such as McConnachie (2012), Drlica-Wagner et al. (2020), Albareti et al. (2017), Aguado et al. (2019), Martin et al. (2016), Abbott et al. (2018) have further contributed to the exploration of dwarf galaxies in the Milky Way. Some of the newly discovered dwarf galaxies include Boötes V, Leo Minor I, and Virgo II (Cerny et al. 2022).

1.2.2 The Local Volume

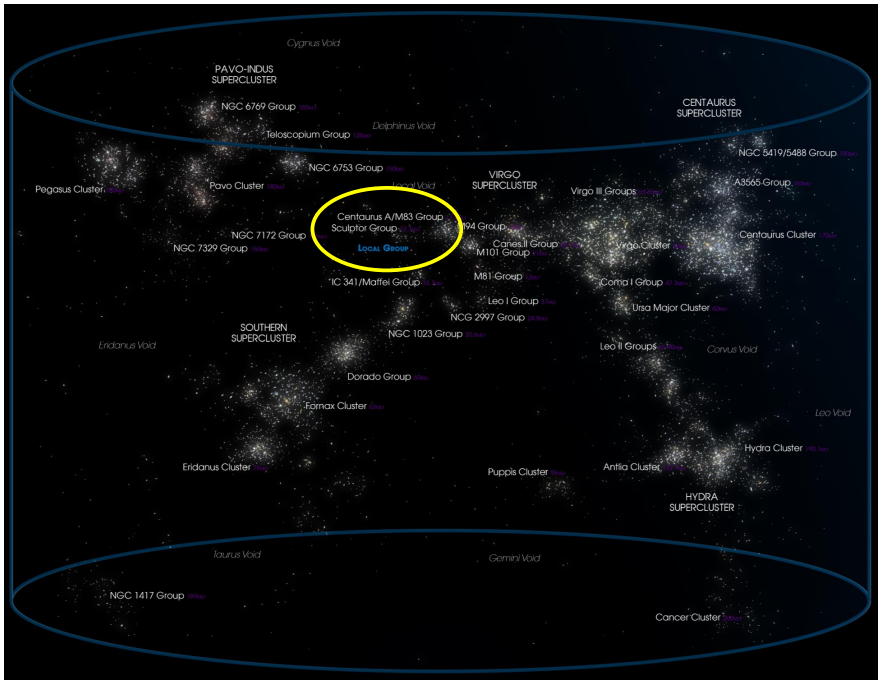

Figure 1.4: This figure illustrates the galaxies in Local Volume. Circled region shows the Cen A and Local Group (Colvin,A.Z. 2020).

While LG dwarf galaxies provide vital information to understand the nature and evo-

lution of dwarf galaxies, galaxies in the local neighborhood alone cannot provide a bigger picture since both the Milky Way and M31 have similar mass environments (Pawlowski et al. 2014). The dwarf satellites of the Local Group also show similar characteristics (Sawala et al. 2012), though recent work has shown some potential differences between the quenching times of dwarfs in the Milky Way and M31 (Weisz et al. 2019). Given the variations in the satellite systems, there is a possibility that studying just the Milky Way and M31 could lead to a bias. Therefore, we need to look beyond the LG. The Local Volume (LV) is the region within 10 Mpc of the Milky Way. It contains multiple massive galaxies and their dwarf satellites, providing numerous systems to study star formation in dwarf galaxies in a variety of environments. The LV is composed of a few hundred galaxies, major galaxy clusters such as Virgo and Fornax, the Local Group, and individual galaxies such as Centaurus A (Cen A, see the circled region in Figure 1.4).

Ongoing and upcoming surveys are pushing the frontiers of observational studies of dwarf galaxies beyond the Local Group. These include, among others, targeted surveys of Cen A (Taylor et al. 2016, Crnojevic 2020, Müller et al. 2015; 2017; 2019), M81/M82 (Sorgho et al. 2019), and wider surveys such as SAGA that explore satellites around Milky Way analogs (Geha et al. 2017, Mao et al. 2021).

In addition, Ferrarese et al. (2012) and Eigenthaler et al. (2018) have surveyed cluster scale environments such as Virgo ($\sim 10^{15}\,M_\odot$) and Fornax ($\sim 10^{14}\,M_\odot$), respectively. While there is an effort to extend observations beyond the LG, the extent of observations beyond the LG is not nearly as complete compared to observations around the Milky Way. Observational and theoretical studies on dwarf galaxies are focused on systems similar to the LG ($\sim 10^{12}\,M_\odot$, McConnachie 2012, Richardson et al. 2011, Geha et al.

2017, Mao et al. 2021) and cluster scale environments such as Virgo ($\sim 10^{15}\,M_{\odot}$, e.g. Ferrarese et al. 2012, Paudel et al. 2017) and Fornax ($\sim 10^{14}\,M_{\odot}$, e.g. Eigenthaler et al. 2018, Rong et al. 2019, Venhola et al. 2019). However, few have explored dwarfs of intermediate mass hosts like Cen A (Müller et al. 2015; 2017; 2019).

Larger hosts can change the star formation physics of dwarf galaxies in many ways, i.e. through stronger tidal stripping, ram pressure stripping, or even reionizing at an earlier time. These effects have been studied in galaxy clusters such as Virgo and Fornax. Larger mass host can impose a stronger tidal field on the dwarf satellites, stripping both dark matter and stars. This would result in low brightness of satellite galaxies around these host galaxies. Fornax cluster is populated with giant early type galaxies and intra cluster X-ray gas indicating strong tidal forces (Venhola et al. 2019). According to Venhola et al. (2019) dwarfs become rounder towards the center of the cluster, thus they conclude that the cluster environment transforms the morphology and structure of satellite dwarfs and is dependent on the mass of the host.

Dwarf galaxies are influenced by larger hosts as they fall into their deeper gravitational potential wells and undergo stronger ram pressure stripping effects. Ram pressure stripping drain gas supply from dwarfs and change their morphology e.g., Virgo cluster galaxy IC 3418 has transformed from a dwarf irregular into a dwarf elliptical galaxy (Kenney et al. 2014). In addition to these quenching mechanisms, gas accretion into dwarf galaxies may also be affected by reionization redshift. Deeper gravitational potential wells of higher mass hosts accrete baryons at earlier redshifts than smaller hosts and thus forms first stars and reionize early on suppressing gas accretion at earlier redshifts. How these mechanisms can affect star formation in dwarf galaxies hosted by larger hosts in cluster

environments has been studied well. Yet, there is a lack of investigation of intermediate-mass hosts in dwarf galaxies. Therefore, the question of how dwarf galaxy physics is affected by different mass hosts needs to be explored further in the intermediate mass host environments.

1.2.2.1 Centaurus A

Cen A also known as NGC 5128, provides the most accessible opportunity to study dwarf galaxies within a higher mass host and in an environment that sits in between the group and cluster scales. It is the closest observable elliptical galaxy, located 3.8 Mpc from the Milky Way (Harris et al. 2010), and has a poorly constrained mass of $4.7 \times 10^{12}\,\mathrm{M}_{\odot}$ -$1.8 \times 10^{13}\,\mathrm{M}_{\odot}$ (van den Bergh 2000a, Pearson et al. 2022).

In recent years, the halo of Cen A has been targeted by several surveys including Survey of Cen A's Baryonic Structures (SCABS, Taylor et al. 2016; 2017; 2018) and the Panoramic Imaging Survey of Cen & Sculptor) (PISCeS, Sand et al. 2014, Crnojević et al. 2014, Crnojevic et al. 2016). These are the first systematic surveys of the dwarf satellites of Cen A. As a result of these surveys, the number of known dwarf galaxies has almost doubled over the 5-10 years.

Several studies have predicted Cen A's virial mass[4] using a variety of methods. For example, Woodley et al. (2007) have computed the mass of Cen A (pressure supported and rotational supported mass) using a Globular Cluster (GC) population within 50 *kpc* ($1.3 \times 10^{12}\,\mathrm{M}_{\odot}$). van den Bergh (2000a) has calculated it using the virial theorem ($1.4 \times 10^{13}\,\mathrm{M}_{\odot}$) and projected mass method out to 640 kpc ($1.8 \times 10^{13}\,\mathrm{M}_{\odot}$). Müller et al. (2022)

[4]Virial mass is the mass of a gravitationaly bound astrophysical system, where $M_vir = \frac{4}{3}\pi r_{vir}^3 \rho(< r_{vir})$.

estimate a dynamical mass of $1.2 \times 10^{13}\,\mathrm{M}_{\odot}$ within 800 kpc. Pearson et al. (2022) have constrained the lower limit ($4.7 \times 10^{12}\,\mathrm{M}_{\odot}$) on the mass of Cen A using stellar stream models. The upper range of virial masses measured for Cen A is $\sim 10^{13}\mathrm{M}_{\odot}$ (van den Bergh 2000a, Peng et al. 2004b, Woodley et al. 2007, Łokas 2008, Harris et al. 2015a), which falls between the masses of the Milky Way and large clusters such as Virgo and Fornax.

1.3 Properties of Dwarf Galaxies

Dwarf galaxies and their properties can be illustrated in many ways to better understand the relations that exist between them. Some of these relations include the luminosity function, luminosity-metallicity, half-light radii, velocity dispersions, mass to light, etc.

Cumulative Luminosity Function: The luminosity function is the cumulative distribution of luminosities for a sample of galaxies. This gives the number of galaxies per absolute V band magnitude bin ($N(< M_V)$). Typically, the number of satellites decreases with increasing brightness. This shows that we should observe more fainter galaxies and fewer brighter galaxies at a given point in time. The cumulative luminosity function for absolute V band scale is given by

$$N(< M_V) = \int_{-M_V}^{\infty} \phi(M_V) dM_V, \tag{1.1}$$

where $\phi(M_V)$ gives the fraction of galaxies per unit magnitude.

Luminosity-metallicity: The luminosity-metallicity relation is an excellent constraint for our model since it forms a smooth function across luminous spiral galaxies to

less luminous dwarf galaxies. Metallicity gives the proportion of elements heavier than Helium in stars of the satellite dwarf galaxies. Metallicity for observations is defined by,

$$[Fe/H] = log_{10}\left(\frac{N_{Fe}}{N_H}\right)_* - log_{10}\left(\frac{N_{Fe}}{N_H}\right)_\odot, \tag{1.2}$$

where N is the number of atoms of each species. Unlike luminosity, which depends on stellar mass of the galaxies at the present day, metallicity leaves an imprint of the peak mass of galaxies even if tidal and ram pressure strips stars and gas. This is because the metallicity of a galaxy is determined by the depth of the potential well and M_{Peak}. [5]

Half Light Radii: Sizes of galaxies and their boundaries are difficult to measure. Galaxies also get fainter further away from their centers. In order to overcome this problem, astronomers define the half light radius or the effective radius. The half light radius is the radius at which half of the light is observed in a galaxy. This is a measure of galaxy sizes. Observed half-light radii are derived by integrating under the appropriate profile (e.g. exponential profile, Sérsic profile, etc.) and ellipticity.

Velocity Dispersions: The stellar central velocity dispersion (σ_*) of a galaxy measures the random line-of-sight motion of stars due to the gravitational potential of the total mass enclosed in within the radius of the stars. It is used to measure the mass of a galaxy, probing the depth of galactic gravitational potential wells where stars are captured, and hence is a good indication for how dark matter dominated a galaxy is.

Mass to Light Ratios: The total mass relative to the total light within a given radius specifies the strength of the dark matter component to the mass of a particular

[5] M_{peak} is the maximum mass a halo gains during its evolution and the galaxy's subsequent ability to hold onto enriched ejecta from supernova.

galaxy. It can be used to convert observed light distributions in galaxies into estimates of mass distributions, thereby providing information for dynamical analysis. Mass to light ratios of the Milky Way satellites fall in the range $10 \leq M/L \leq 1000\ \mathrm{M}_{\odot}/L_{\odot}$.

Star Formation Histories (SFHs): The cumulative star formation history provides the total stellar mass of satellite galaxies from past to the present. Each point in time represents the sum of stellar mass at time t from 0 Gyrs to t Gyrs. Stellar mass at any point across history presents evidence for quenching effects throughout the galaxy's history. The SFH of a galaxy can be used to compute quenching times such as τ_{90} which is the time taken to gain 90% of stellar mass we see today and τ_{50}, the time taken to gain 50% of stellar mass we see today.

All these observed properties of galaxies discussed above give valuable information on their star formation, metallicity, history, sizes, etc. These properties have to be compared with theoretical models that test various star formation physics to further understand them. In this next section, we will discuss the computational methods that are used to study galaxies.

1.4 Computational Methods

Observations are crucial to our understanding of dwarf galaxies, but they only provide us one snapshot in galaxy evolution. Therefore, observed data alone cannot give us a clear picture of their star formation physics. However, we can use computational techniques such as simulations and models to evolve galaxies in a simulated universe. Such techniques include N-body simulations, hydrodynamic simulations, and SAMs among others.

These are extremely useful in modeling physics of star formation and their evolution in dwarf galaxies, which cannot be achieved in real time.

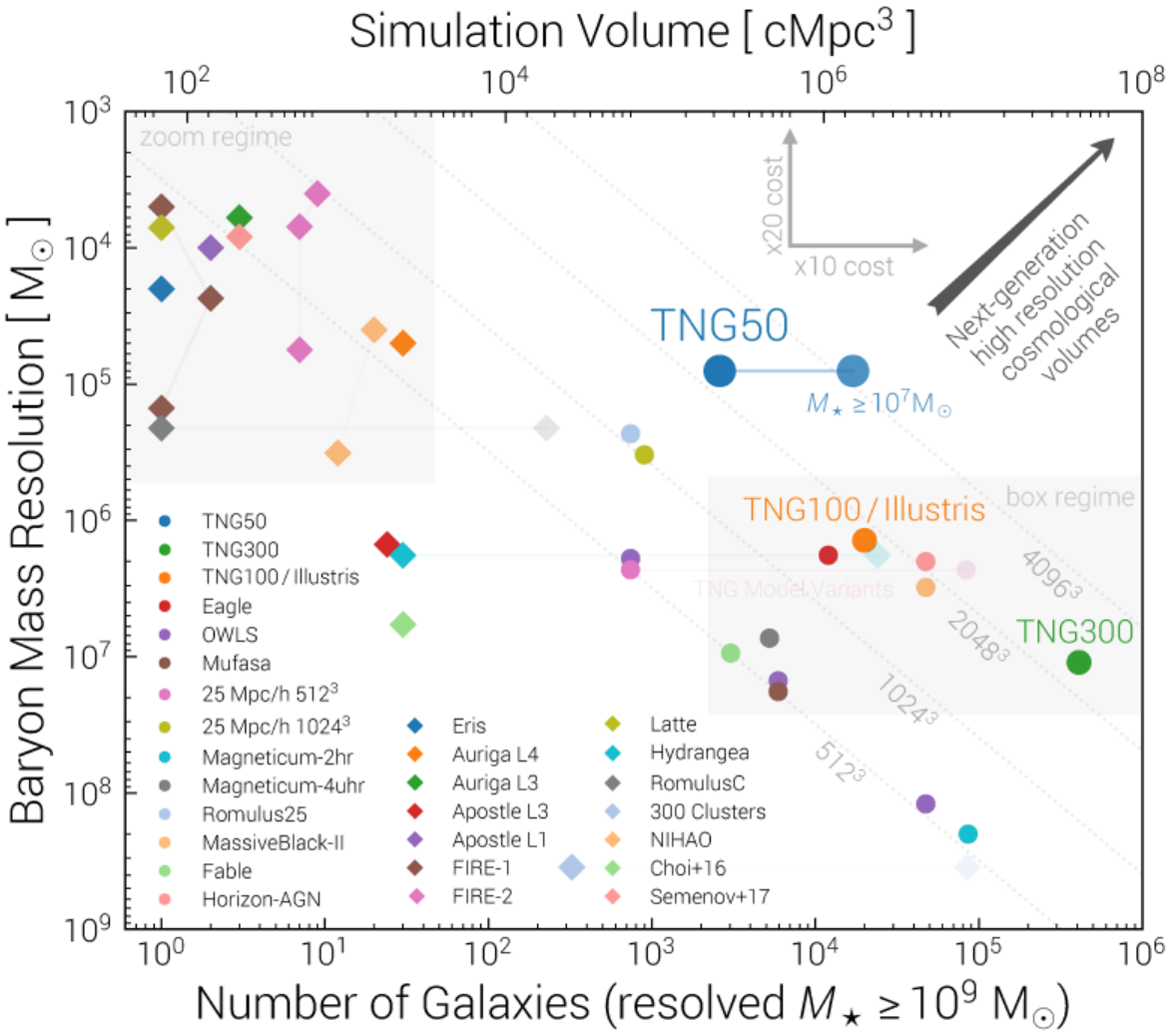

Figure 1.5: This figure shows a plot by Nelson et al. (2019). Baryonic mass resolution vs. number of galaxies that resolves stellar mass $\geq 10^9\,\mathrm{M}_\odot$ for several hydrodynamic simulations. Notice that higher resolution small box simulations are in the top left corner, while the low resolution simulations providing larger statistics are on the right hand side. Also notice the limitations of hydrodynamic simulations to gain higher resolution and larger statistics/box sizes simulataneously. The upper right hand corner shows where the next generation of high resolution cosmological simulations are expected.

1.4.1 Cosmological Simulations of Dwarf Galaxies

In concert with our increased understanding of the observational properties of dwarf galaxies, theoretical studies of the fossils of the first galaxies (Bovill and Ricotti 2009, Ricotti et al. 2016, Wheeler et al. 2019) and of dwarf satellites around the Milky Way using hydrodynamical simulations have come of age (Hopkins et al. 2018b, Applebaum et al. 2021). Hydrodynamic simulations are simulations that model the interaction of dark matter, stars, and gas using smooth particle hydrodynamics (Springel et al. 2005). They self consistently resolve hydrodynamics, star formation, stellar evolution and feedback, black holes, etc. These simulations are much more complex when compared to N-body simulations, and capture non-linearities and non-equilibrium processes that simpler models cannot. These complexities are challenged with limitations in the dynamic range of simulations. Dynamic range for any simulation are factors that limit a simulation: e.g., mass resolution limits, simulation box size, etc. Thus, hydrodynamic simulations are extremely computationally expensive when simultaneously resolving dwarf galaxies while evolving them in a larger simulation box (Qin et al. 2019).

The advanced physics in these simulations involve challenging computations. Therefore, one must compromise either resolution or complexity of the physics simulated. Their cost limits the freedom to explore parameters governing physical processes (Côté et al. 2018). As a result, most hydrodynamic simulations fall into two categories: (1) simulations with larger volumes to study statistics and (2) simulations with smaller volumes with sufficient mass resolution and softening to study small scale structures.

The Milky Way dwarfs have been simulated with hydrodynamical simulations (Hopkins et al. 2018b, Akins et al. 2021, Applebaum et al. 2021, Wetzel et al. 2022). Hopkins et al. (2014a; 2018a), Wetzel et al. (2022) simulates Milky Way analogs resolving star formation physics down to low mass dwarfs ($M_V < -8$, $M_* \geq 1.6 \times 10^3\,\mathrm{M}_\odot$). The Mint Justice League simulations have reproduced properties of the Milky Way satellite system, including the half-light radii, velocity dispersions, and metallicity of the ultra-faints (Applebaum et al. 2021). These simulations have small box sizes and high mass resolutions that can resolve dwarf galaxies. While they are able to resolve these smaller dwarfs, any physics that occurs below parsec scales or the resolution limit is calculated via a semi-analytic approach. Thus any calculation of star formation, feedback, and AGN treatment is at a "sub-grid" level where effects of small scales are introduced by solving differential equations.

Simulations of massive systems outside our galaxy neighborhood up to $z = 0$ do not meet the resolution required to resolve star formation physics in these dwarfs. However, these types of simulations provide large statistical samples of galaxies. Such large scale simulations include Illustris-TNG (Weinberger et al. 2017, Pillepich et al. 2018b), TNG300, TNG100 (Nelson et al. 2018, Naiman et al. 2018, Pillepich et al. 2018a, Springel et al. 2018, Marinacci et al. 2018), TNG50 (Nelson et al. 2019, Pillepich et al. 2019), MilleniumTNG (Hernández-Aguayo et al. 2022). Both TNG300 and TNG100 are simulations with larger box size of 300 Mpc and 100 Mpc respectively, and resolve larger galaxies and clusters. TNG50 has a smaller box of 50 Mpc, resolving galaxies down to Small Magellanic Cloud (SMC) - Large Magellanic Cloud (LMC) scale dwarf galaxies.

The limitations in simulating large volumes present the challenge of modeling dwarf galaxies in these larger mass environments. Given the similarities of dwarfs in the LG and their properties, it is imperative that we look beyond the LG to understand whether properties in dwarf galaxies are independent of the environment or not. With the upcoming unprecedented amount of observations through Roman, it is essential that we explore dwarfs beyond the Local Group with theoretical models. Yet, simulating larger systems that resolve the stellar physics of dwarf galaxies with hydrodynamic simulations is still beyond current capabilities. As our observational sample of dwarf galaxies expands beyond the Local Group, there is a need to simulate dwarf satellite systems in a wider range of environments that currently cannot be explored by hydrodynamical simulations. It is crucial to model the baryonic physics in dwarf galaxies in order to understand the effect of the local environment on the dwarf galaxies' feedback mechanism. Therefore, we need to use alternative methods of modeling these dwarf galaxies.

1.4.2 SAMs To The Rescue

With the limitations of hydrodynamic simulations to resolve star formation physics of dwarf galaxies noted above, we need to use other techniques to model these fainter dwarfs. One of the most efficient and feasible methods for this task are SAMs. They are computationally inexpensive and allow us to explore the parameter space of larger systems beyond the Milky Way. In SAMs, the baryonic physics is approximated by a set of interconnected differential equations to model the baryonic evolution of galaxies

through cosmic time. This is an efficient way of modeling galaxies (e.g. Henriques et al. 2009, Benson and Bower 2010, Bower et al. 2010) and permits rapid modeling of dwarf galaxies in a range of environments. While SAMs are computationally efficient and use relatively straightforward physics, formulated via simple Ordinary Differential Equations, their underlying assumptions and simplifications must be tested against more sophisticated hydrodynamic simulations.

Various studies have used SAMs to model galaxies. These analytic models were first proposed by White and Rees (1978), and advanced by White and Frenk (1991), Kauffmann et al. (1993), Somerville and Primack (1999), Cole et al. (2000b), Hatton et al. (2003), Monaco et al. (2007), Somerville and Davé (2015), and others. While the first SAMs were built on Extended Press-Schechter (EPS) merger trees (Press and Schechter 1974), they can now be applied to merger trees from N-body simulations (e.g. Kauffmann et al. 1999, Helly et al. 2003). Previous studies modeling dwarf galaxies with SAMs include Li et al. (2010), Font et al. (2011), Starkenburg et al. (2013), Lu et al. (2017), Pandya et al. (2020), Bose et al. (2020), Jiang et al. (2021), Chen et al. (2022). Macciò et al. (2010) have reproduced the luminosity function of the Milky Way satellites down to the ultrafaints. Starkenburg et al. (2013) reproduce the luminosity function and the luminosity-metallicity relation down to $M_V < -5$. They also reproduce the SFHs of some satellites, although models do not match all of their observed properties. Jiang et al. (2021) have used `SatGen` to produce a statistical sample of Local Group satellites. Bose et al. (2020) have used the Durham SAM with high resolution N-body simulations to explore the relation between the abundance and the assembly history of the host.

These authors have also reproduced the radial distribution of satellite galaxies. Pandya et al. (2020) have tested the Santa-Cruz SAM (Somerville and Primack 1999) against the FIRE-II cosmological simulations (Hopkins et al. 2018b; 2014b, Wetzel et al. 2022). Although their stellar-halo mass relations and stellar mass assembly histories agree well with FIRE-II, Inter Stellar Medium (ISM) masses agree only for higher mass halos. In order to reproduce gas accretion efficiencies of FIRE-II dwarfs, they implement a mass dependent preventative feedback model to suppress accretion of gas into halos. Note that "preventative feedback" here means preventing accretion of gas onto halos via stellar feedback (Lu et al. 2017, Pandya et al. 2020). However, details between implementations in the Santa Cruz SAM (Pandya et al. 2020) and the SAM by Lu et al. (2017) vary. The recent study by Chen et al. (2022) has reproduced the stellar mass to halo mass relation of the Milky Way satellites at $z = 0$ down to the ultra faints while providing a framework to study stellar properties and SFHs of metal-poor stars. These previous studies show that SAMs are an efficient method to study dwarf galaxies and their star formation processes. Therefore, in a time where hydrodynamic simulations are limited by their resolution or volume to solve dwarf galaxy physics in larger hosts along with their host environment, SAMs come to the rescue.

1.5 Outlook for This Thesis

This dissertation investigates the star formation physics of the dwarf galaxies across different mass environments, i.e., environments with different local volume densities (see Figure 1.6 for systems with a range of mass environments) using the Galacticus (Ben-

son 2012). Chapter 2 describes the N-body simulations and development of merger trees used to model dwarf galaxies of the Milky Way and Cen A. Chapter 3 presents the observations and constraints of the star formation physics of the Milky Way satellites. Chapters 4 and 5 present the properties of the Milky Way satellites at $z = 0$ followed by their SFHs. Chapter 6 describes the observational sample of Cen A dwarf galaxies and the resulting dwarf galaxy models for Cen A satellites, their properties at $z = 0$ and SFHs. Chapter 7 explores the curious case of dwarf galaxies within the inner region of Cen A. These dwarf galaxy models test whether the star formation physics of dwarf galaxies is universal or if is dependent on their host galaxy environment.

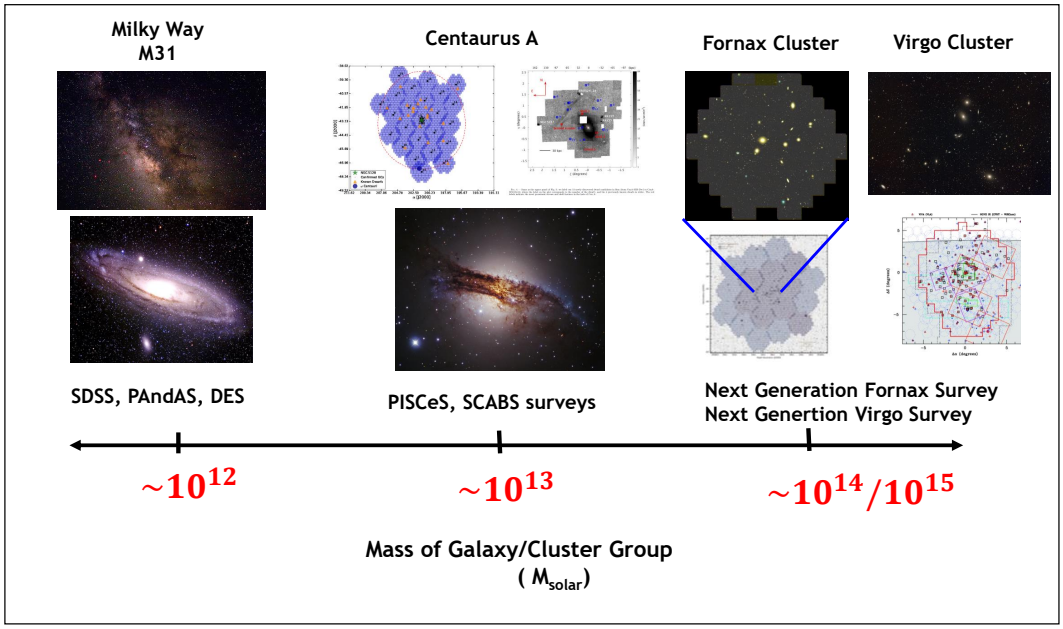

Figure 1.6: This figure shows the mass range of galaxies and clusters available through SDSS (Kollmeier et al. 2017), PAndAS, PISCeS (Crnojevic et al. 2020), SCABS (Taylor et al. 2016, Taylor et al. 2018), NGFS (Rong et al. 2019), NGVS (Cantiello et al. 2018). Left: Milky Way and Andromeda, middle: Cen A, right: Fornax and Virgo cluster. This figure is assembled with figures from Ferrarese et al. (2012), Ordenes-Briceño et al. (2018), Taylor et al. (2017; 2018)

Chapter 2

Simulations

In this Chapter, we describe the process of generating merger trees in our simulation and methods of processing them before applying baryonic physics using a SAM in Chapter 3. We are building merger trees using two methods; N-body simulations and EPS formalism. Parts of this chapter are extracted verbatim from Weerasooriya et al. (2023; in prep. a;b).

2.1 N-body Simulations

An N-body simulation models a dynamical system of N particles. The N-body code integrates and solves the equations of motion for N particles under gravity. The dynamic range of N-body simulations are dependent on mass resolution and volume or box length. Mass resolution is the mass of a dark matter particle in the simulation while the softening length is a trick used in cosmological N-body simulations to avoid close encounters of particles that would result in unphysical motion of particles. The non compact force for

particles F_i^{inc} is given by,

$$\vec{F_i^{inc}} = \sum_j^N \frac{G m_i\, m_j}{(r_{ij}^2 + \varepsilon^2)^2} \frac{\vec{r_{ij}}}{|\vec{r_{ij}}|}, \tag{2.1}$$

where ε is the softening length.

Thus softening length limits the substructure resolved in an N-body simulation. Therefore, both of our simulations have dark matter particles of mass $m_p = 1.4 \times 10^5\,\mathrm{M}_\odot$ and softening length $\varepsilon = 200\,\mathrm{kpc}$ in the highest resolution region since we are interested in halos of $\sim 10^7 - 10^8\,\mathrm{M}_\odot$. Note that these cosmological simulations can suffer from overmerging due to inadequate softening. For example, van den Bosch and Ogiya (2018) recommend sub-halos be simulated with at least 10^6 particles with softening length 0.03 times their Navarro–Frenk–White (NFW) scale radius ($R_s = R_{vir}/c$, where c is the concentration parameter) in order to properly track their dynamics and disruption. However, implementing that level of resolution is computationally prohibitive. We use dark matter only N-body simulations with Nine-Year Wilkinson Microwave Anisotropy Probe (WMAP9) cosmology ($\sigma_8 \sim 0.821$, $H_0 \sim 70.0 km/s/Mpc$, $\Omega_b \sim 0.0463$, $\Omega_\Lambda \sim 0.721$, Bennett et al. 2013, Hinshaw et al. 2013). All simulations described in this work were run on the Maryland High Performance Computer Cluster Deepthought 2 [1]). All dark matter halo densities in our simulation are assumed to follow a NFW profile (Navarro et al. 1997),

$$\rho(r) = \frac{\rho_0}{\frac{r}{R_s}\left(1 + \frac{r}{R_s}\right)^2}$$

,

where r is the distance from the center, R_s is the scale radius of the halo, and ρ_0 is the

[1] http://hpcc.umd.edu

density parameter unique to each halo.

2.1.1 Simulation Box

Particles of an N-body simulation are in a cubic box with comoving coordinates. This is because proper physical distances can change with time due to expansion of the universe. Comoving coordinates accounts for this expansion and make sure galaxies remain at the same position in space, i.e. simulation coordinates moves with the galaxy as its position is changing. Comoving distance x is related to physical distance r by $x = r/a$, where $a(t) = 1/(1+z)$ is the scale factor. Then the comoving velocity is given by dx/dt. Each simulation box is given a box length L in comoving coordinates in units of $\mathrm{Mpc\,h^{-1}}$. The effective resolution of the simulation box is given by $N_{eff} = \sqrt[3]{N_{tot}}$, and thus an effective resolution of $N_{eff} = 4096^3$ is higher than $N_{eff} = 256^3$.

2.1.2 Generating Initial Conditions

Initial conditions for all N-body simulations are generated with Multi Scale Initial Conditions (MUSIC) by Hahn and Abel (2011). The first step is to run a pre-flight simulation with desired resolution, random seed, starting redshift, cosmological parameters, and input transfer function. Note that the set random seed cannot be changed, nor can new seeds be added. Once the simulation is run, we then identify the Lagrange region. This is the region where the particles of the desired halo at $z = 0$ are found back in time at the starting redshift (see Figure 2.1). Positions of these particles are then saved to an initial conditions file. Finally, we compute the bounding box of the simulation and set

boundaries.

2.1.3 Building a Zoom Simulation

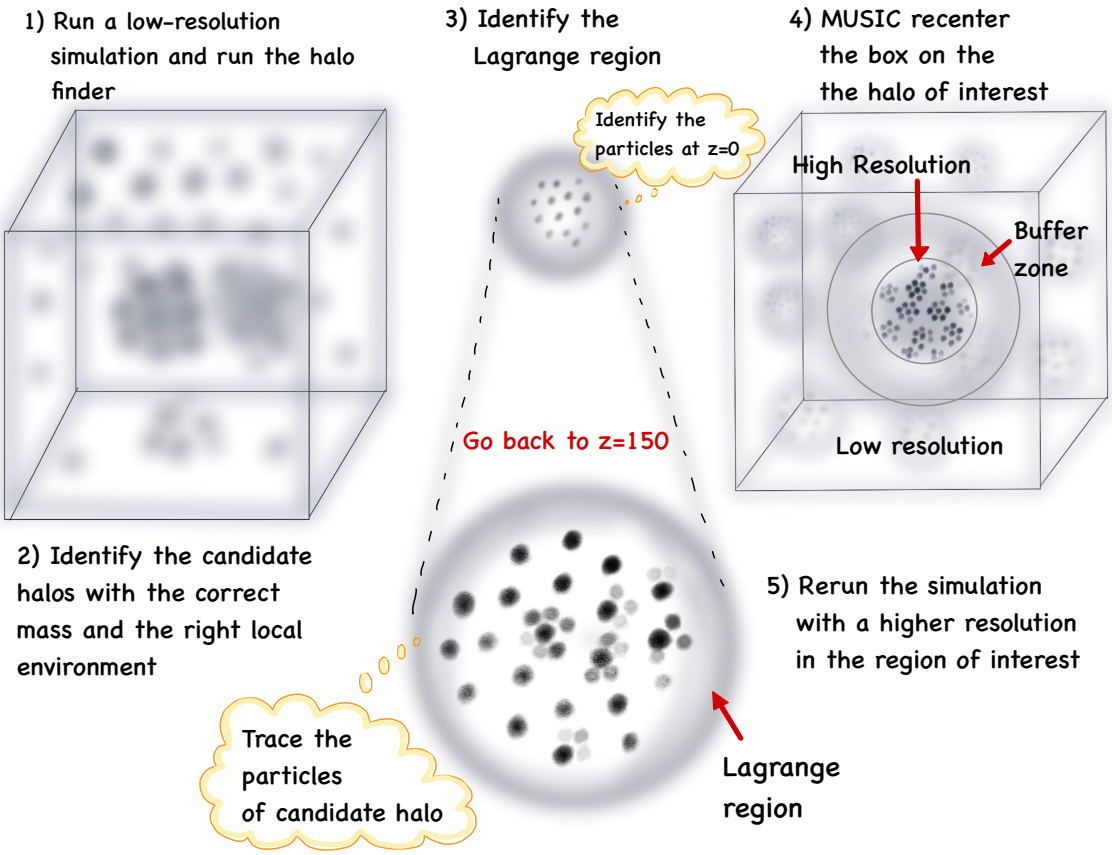

Figure 2.1: Process of producing a zoom simulation. Step 1: Run a low resolution simulation and run the halo finder, Step 2: Identify candidate halos with the correct mass and right local environment, Step 3: Identify the Lagrange region. This is the region where progenitor particles of the present day host halo resides in the past, Step 4: Recenter the simulation box on the halo of interest using MUSIC (Hahn and Abel 2011), Step 5: Rerun the simulation with a higher resolution in the region of interest including a buffer zone.

Simulating a single Milky Way galaxy is computationally expensive and simulating the entire simulation volume is even more computationally expensive. Therefore, a feasible way to achieve the required resolution is to zoom into specific regions of interest within

a low resolution cosmological simulation and rerun at a higher resolution in a smaller region as shown in Figure 2.1. The first step is to identify dark matter halos with correct mass and local environment based on the mass of the host halo and the volume with no large halos in the region. Then, the host halo particles are traced back in time from $z = 0$ to the beginning of the simulation ($z = 150$). This region where these progenitor particles reside is called the Lagrange region. Next, the host halo is recentered on the Lagrange region and new initial conditions are generated using MUSIC (Hahn and Abel 2011). Finally, the new zoom-in simulation is rerun at a higher resolution.

2.1.4 Halo Finding

The next step after running a simulation is to identify the halo boundaries and calculate their properties. We identify the dark matter halo boundaries in our simulations and calculate their halo properties such as virial radius, mass, circular velocity, etc. using halo finders. We achieve this using two types of halo finders, Robust Overdensity Calculation using K-Space Topologically Adaptive Refinement, (ROCKSTAR, Behroozi et al. 2013a) and Adaptive Mesh Investigations of Galaxy Assembly, (AMIGA, Knollmann and Knebe 2009). The two halo finders use distinct algorithms, specifically the phase space Friends of Friends (FOF) and the spherical overdensity algorithms.

2.1.4.1 Friends Of Friends (FOF)

As illustrated in Figure 2.2, Friends of Friends algorithms employ 6D space positions and velocities to identify particles within an adaptive linking length and group them into halos. In particular, ROCKSTAR (Behroozi et al. 2013a) uses this algorithm by initially

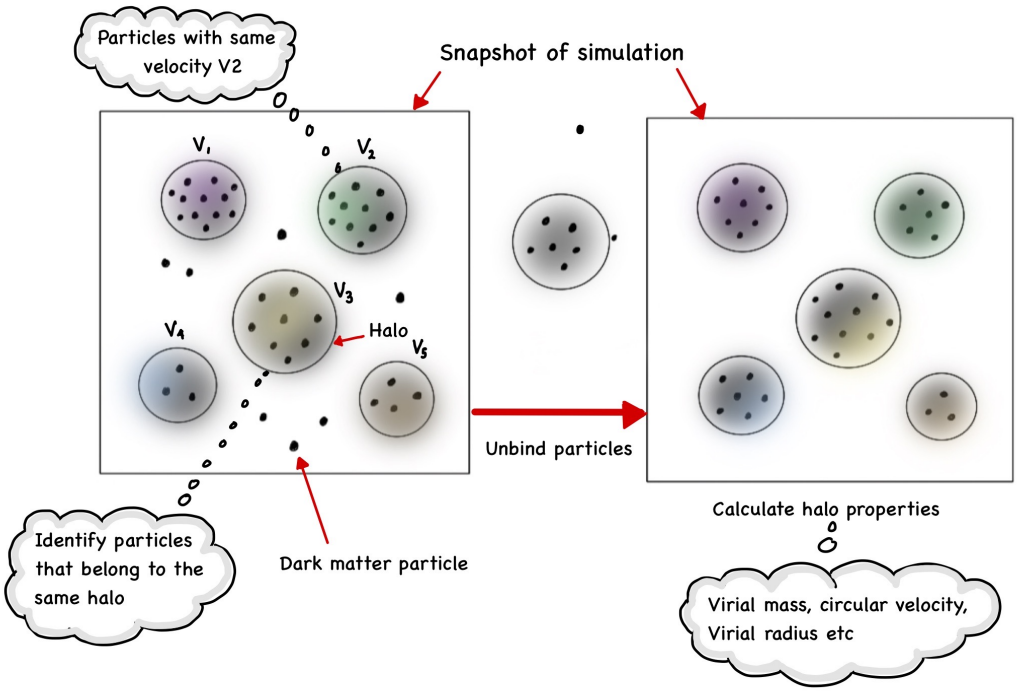

Figure 2.2: Process of halo finding using Friends of friends (FOF) algorithm. Left: Simulation snapshot with dark matter particles: First, particles are grouped together based on their physical proximity and velocities. Here, the distance between particles and their velocities are used to calculate a linking length. If distance between a particle and a halo or two particles is less than this linking length, then they are grouped together. Right: Loosely bound particles are unbound using relative error in potential energy. Once, halo boundaries are identified the algorithm then calculate various properties of dark matter halos such as their mass, velocity, radius, etc.

dividing the simulation volume into 3D FOF groups, where particles are positioned within the linking length. Subsequently, for each 3D FOF group, particle velocities and positions are normalized by the group positions and velocity dispersion. This process continues for each subgroup, and a new level of substructure is computed. Once all levels of substructure have been identified, particles are assigned to the nearest halo in both position and velocity space in a hierarchical manner. Unbound particles are subsequently eliminated based on their minimum gravitational potential. Finally, halo properties such as maximum circular velocity, virial mass, virial radius, etc., are determined.

2.1.4.2 Spherical Overdensity Algorithms

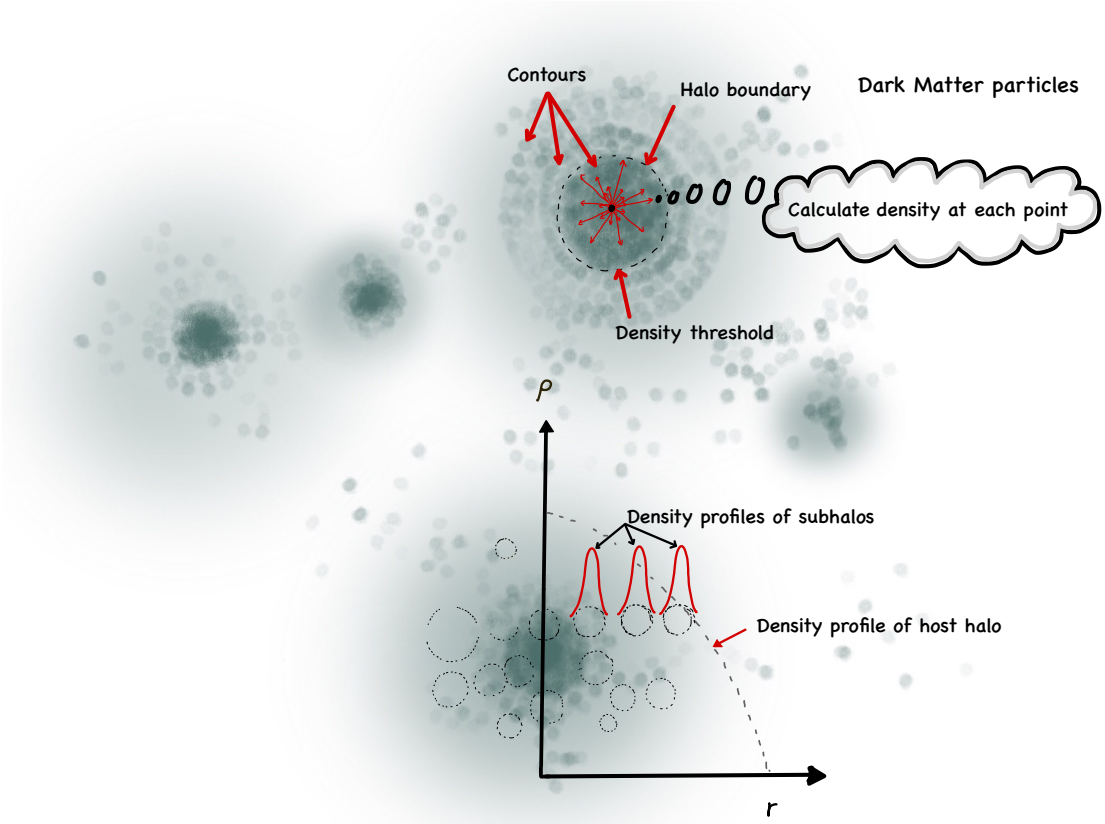

Figure 2.3: Cartoon of a spherical overdensity algorithm process. Top part of the figure shows how a halo boundary is identified. First, it calculates the density of the dark matter particles in the simulation and draws density contours. Once a threshold density is reached, it identifies the region enclosed as a halo. Loosely bound particles are unbound if the velocity of the particles are greater than their escape velocity. The plot below shows the density profile which gives the density of halos as a function of radius. Black dotted lines shows the density profile of the host halo while the red peaks shows density peaks of the sub halos. The algorithm identifies the density peaks of the sub-halos easily if they are located away from the center of the host halo.

Spherical overdensity algorithms identify density peaks and establish density contours around them until a particular overdensity threshold is achieved (Knollmann and Knebe 2009, see Figure 2.3). The AMIGA halo finder, developed by Knollmann and Knebe (2009), employs a spherical overdensity algorithm and analyzes the simulation utilizing

Adaptive Mesh Refinement (AMR). AMR technique selectively refines the current mesh in regions of higher density where precision is required.

2.1.4.3 Rockstar vs. AMIGA

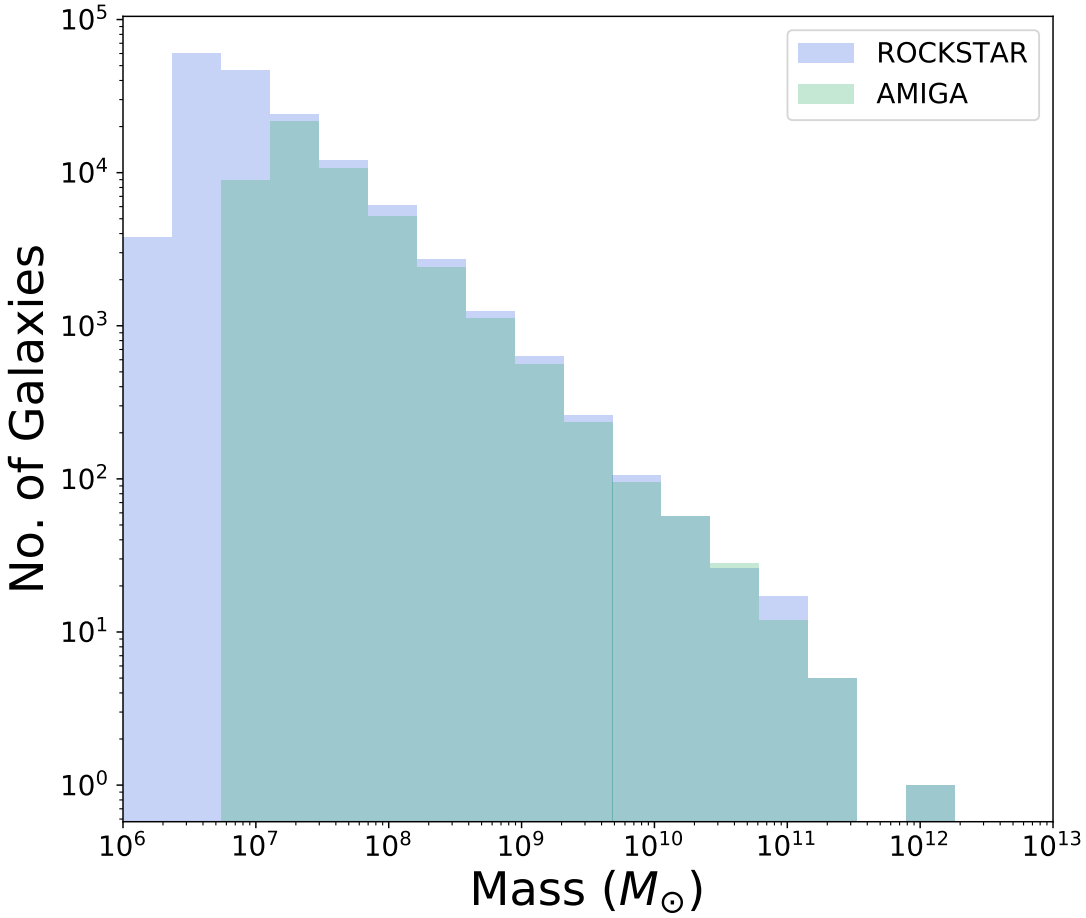

Figure 2.4: Dark matter halo mass function of all the halos in the simulation for AMIGA and ROCKSTAR. AMIGA halo mass function is plotted in green color and ROCKSTAR halo mass function is colored in blue.

The halo mass function of the number of galaxies per mass of each galaxy in the Milky Way analog for the two halo finding algorithms (in solar units, see Figure 2.4).

Note that Rockstar halo finder identifies smaller mass halos down to $\sim 10^6$ $M_\odot$ while AMIGA has halo masses down to $\sim 10^7$ $M_\odot$. Based on the the time taken to run each halo finder, ROCKSTAR is ~ 16 times more efficient than AMIGA. Despite being an efficient algorithm, ROCKSTAR and similar FOF algorithms may suffer from the issue of breaking large halos into smaller components.

Halo finder	*Algorithm*	*Time per snapshot*
ROCKSTAR	FOF	10 min
AMIGA	Overdensity	2.61 hrs

Table 2.1: This table summarizes information on the halo finders, their type of algorithm, and time required to analyze one snapshot on a Mac mini. Note, each simulation has > 200 snapshots.

2.1.5 Merger Tree Evolution

Once we identify the halo boundaries and their properties using a halo finder, next we determine the merger history of halos through cosmic time using the merger tree code, consistent_trees (Behroozi et al. 2019) (see Figure 2.5 for a schematic representation of a merger tree). Merger trees link each halo to their respective progenitors and allows exploration of their history. They identify the particles of each halo at $z = 0$ and track them back in time. At each time step in the simulation, the algorithm identifies and links halos that contain particles from a halo in the previous timestep. The halos with the highest number of particles in common with the previous halo are considered the most massive progenitor. This process is repeated for each snapshot until all the progenitor

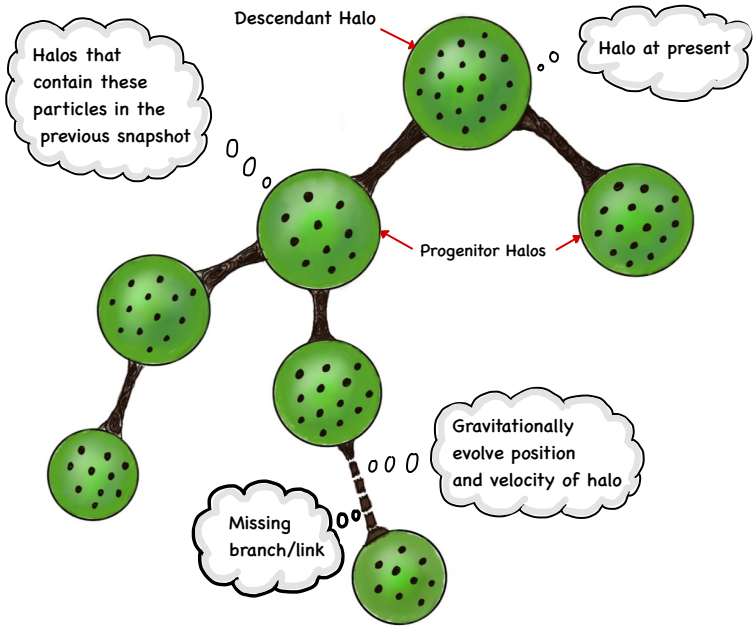

Figure 2.5: This figure shows the process of linking halos in the merger tree code consistent trees (Behroozi et al. 2019). First, it identifies the dark matter particles in a halo at the present day (descendant halo). Then, it goes back in time to previous snapshot in the simulation to locate the halo which contains the most number of these same particles. Halo that contain these particles is called the progenitor halo. This process is repeated until the algorithm reaches the beginning of the simulation. If certain progenitors cannot be located, then positions and velocity of halos are used to gravitationally evolve their future/past positions and velocities to fix these links. Once every dark matter halo in the simulation is linked to their progenitor, a complete merger history of the simulation can be obtained.

halos are identified from the formation of the first halos in the simulation. If a halo falls below the resolution limit in one snapshot, the algorithm approximates its properties in each time step, and connect broken links if necessary. It is removed if a halo has no descendants and its existence has low statistical significance.

Note that most dark matter halo properties (total mass, NFW scale length) used in Galacticus are preset from the N-body trees with the exception of halo spins. Halo spins are typically not well-measured in halos with fewer than of order 40,000 particles

(Benson 2017b).

2.1.6 Milky Way Analog

We run an N-body simulation of a Milky Way analog from $z = 150$ to $z = 0$. Here z refers to the cosmological redshift[2]. $z = 150$ correspond to about 9 mega years after the big bang and $z = 0$ correspond to present day. Initial conditions were generated with MUSIC (Hahn and Abel 2011) and the simulation was run with GADGET 2 (Springel 2005).

We select an isolated Milky Way analog from a 50 $\mathrm{Mpc}\,h^{-1}$ box with $N_{\mathrm{eff}} = 256^3$ run from $z = 150$ to $z = 0$, resolving the Milky Way candidates at $z = 0$ with $N > 1000$ dark matter particles. Our isolation criteria is a $M_{vir} \sim 10^{12} M_{\odot}$ halo, with no halos greater than $M_{vir} \sim 10^{12}\,\mathrm{M}_{\odot}$ within $3\,\mathrm{Mpc}\,h^{-1}$ at $z = 0$. We select a Milky Way analog with $M_{vir} \sim 1.8 \times 10^{12}$ $\mathrm{M}_{\odot}$ ($M_{vir} \sim 1.2 \times 10^{12}$ $\mathrm{M}_{\odot}/h$) following the above conditions. Note that our simulation has only one such Milky Way analog with the surrounding environment. Neither M31 or the Milky Way are within each others virial radii. Therefore, it is safe to assume that presence (or absence) of an M31 analog in our simulations will not affect the properties and distribution of the dwarf satellites within the virial halo of the Milky Way. In addition, we are constrained by the computational resources. Even if we have a Local Group analog in our low resolution box, it might not remain as a Local Group analog when the simulation is rerun at higher resolutions. As a result, it is standard practice to simulate isolated analogs of the Milky Way (e.g.

[2] z is the cosmological redshift defined by $z = \frac{\lambda_o - \lambda_e}{\lambda_e}$, where λ_o is the observed wavelength and λ_e is the emitted wavelength.

Springel et al. 2008, Gottloeber et al. 2010, Bovill and Ricotti 2011, Akins et al. 2021). The effects of small number statistics will be minimized if multiple zoom-in simulations were run. However, such exploration is a subject of future work.

Once a Milky Way analog is identified at $z = 0$, we rerun a dark matter only zoom in simulation centered on that chosen halo. The high resolution region at $z = 150$ is defined by the particles within 5 $R_{\rm vir}$ from the Milky Way analog at $z = 0$. The highest resolution region has $N_{\rm eff} = 4096^3$, resolving $M_{vir} \sim 10^7\ M_\odot$ halos with at least 100 particles and softening of $\epsilon = 200\,{\rm kpc}$ (physical units).

2.1.7 Cen A Analog

We use a high-resolution cosmological N-body simulation of an isolated Cen A halo from Bovill et al. (2016). This simulation is run from $z = 150$ to $z = 0$ with WMAP9 cosmology ($\sigma_8 \sim 0.821$, $H_0 \sim 70.0\,km\,s^{-1}\,Mpc^{-1}$, $\Omega_b \sim 0.0463$, $\Omega_\Lambda \sim 0.721$). Initial conditions were generated with `MUSIC` (Hahn and Abel 2011) and the simulation run with GADGET 2 (Springel 2005) and analyzed with the `AMIGA` and `CONSISTENT_TREES` (Behroozi et al. 2013b). The Centarus A analog is selected to be a $\sim 10^{13}\ M_\odot$ halo with no halos $M \geq 10^{12}$ M$_\odot$ within 3 $Mpc\,h^{-1}$ at $z = 0$. Cen A simulation suite include two resimulations. CenA.100M.8192 has a comoving periodic box of $100 Mpch^{-1}$ with 8192^3 particles run from $z = 150$ to $z = 0$. All initial conditions are generated with MUSIC (Hahn and Abel 2011). First, a simulation is run with 100 Mpc h^{-1} box with $N = 256^3$, resolving Cen A candidates at $z = 0$ with > 1000 particles. Then Cen A analog halo with total virial mass of 10^{13} M$_\odot$ is chosen. This value corresponds to the upper range of

virial masses measured for Cen A van den Bergh (2000b), Peng et al. (2004a), Woodley et al. (2007), Łokas (2008), Harris et al. (2015b). We estimate the LV and environment around Cen A using an isolation criterion of no dark matter halos $M_{vir} > 10^{12} M_{\odot}$ within 3 Mpc h^{-1} from a Cen A analog at $z = 0$. However, our simulation do not consider the existence of M83, which is located roughly 1 Mpc away from Cen A. Yet, it is unlikely to bias our results, given that M83 is situated at a distance of approximately 2-3 times the virial radius away from Cen A.

Next, we identify the Cen A analog using a halo finder and resimulate the Lagrangian region of approximately 4 times the virial radius (2.4 Mpc) at $z = 0$ to produce a higher resolution region that covers two times the virial radius at $z = 0$. The two resimulations has effective resolutions $N_{eff} = 4096^3$ and $N_{eff} = 8192^3$, respectively, and particle masses of $m_p = 1.13 \times 10^6 \mathrm{M}_{\odot}$ and $m_p = 1.4 \times 10^5 \mathrm{M}_{\odot}$, respectively. In addition, we set the corresponding force softening lengths to $\epsilon = 500$ pc physical and $\epsilon = 200$ pc h^{-1}. These resolutions ensure that halos greater than $10^7, 10^8\,\mathrm{M}_{\odot}$ are resolved with at least 100 and 1000 particles, respectively.

Run	N_{eff}	m_p ($\mathrm{M}_{\odot}$)	ϵ (pc h^{-1})	N_{part}	M_{host} ($10^{13}\mathrm{M}_{\odot}$)	v_{max} (km s^{-1})	R_{vir} ($kpch^{-1}$)
MW.50M.4096	4096	1.4×10^5	200	529	0.104663	177.61	165.11
CenA.100M.8192	8192	1.4×10^5	200	437	1.17269	437.78	369.46

Table 2.2: Summary of simulation characteristics for Milky Way and Cen A. Columns in order are (1) label for the simulation, (2) maximum effective resolution, (3) minimum dark matter particle mass, (4) physical softening length in pc/h, (5) Number of particles in the host halo, (6) Virial mass of the host halo in units of $10^{13}\mathrm{M}_{\odot}$, (2) maximum circular velocity of the host halo in km s^{-1} , and (7) Virial radius of the host halo in kpc/h. Note that values for Cen A is from Bovill et al. (2016).

2.2 Extended Press Schechter Trees

As seen above N-body simulations require high-performance computers, especially for higher mass galaxies like Cen A. Merger trees are inherently statistical. Another efficient method to generate merger trees is via Extended Press Schechter (EPS) theory.

EPS theory approximates the mass functions of virialized dark matter halos based on statistics of the density field. The concept behind this theory is that virialized structures form in regions where the density is above some threshold. It is an extension of the theory introduced by Press and Schechter (1974). Several studies have shown that the Press-Schechter formula agrees well with the results of N-body simulations (Efstathiou et al. 1988, Efstathiou and Rees 1988, Cole et al. 2008, Benson 2017c). The density field is filtered around a radius above a certain threshold. These models inherently do not have positional information.

EPS method uses a Monte Carlo Algorithm to populate a merger tree statistically. A progenitor halo (M_{prog}) that is less massive than its parent halo (M_{halo}) is generated as follows. First, it calculates P, the mean number of fragments with masses M_{prog} in the range $M_{res} \leq M_{prog} \leq M_{halo}/2$, where M_{res} is the mass resolution of the merger tree. Then, a time step is chosen such that $P << 1$ and a random number R is also generated between 0 and 1. If $R < P$, then the halo fragments into progenitor mass M_{prog}, and if $R > P$, then a particular halo M_{halo} does not fragment at that timestep. If a fragmented halo is less than zero, the loop is broken, and the next halo is processed. This process is repeated over steps back in time to build a merger tree Cole et al. (2000a).

EPS models are significantly more efficient compared to N-body simulations. For example, EPS model of a Cen A analog takes $\sim$ 1 day to run on a laptop whereas, a N-body simulation takes approximately three weeks on a supercomputer. However, EPS trees are unreliable for halos with $< 10^{10} M_{\odot}$ due to dynamic range limitations of EPS (Somerville and Kolatt 1999, Zhang et al. 2008). Mass fragmentation in a merger tree depends on the time step. Thus, larger step sizes could limit the dynamic variations in mass of halos in EPS merger trees. Consequently, limitations in mass result in limitations in the size of halos and their respective half-light radii.

We model several Cen A mass analogs using EPS merger trees for $5 - 9 \times 10^{12}\,\mathrm{M}_{\odot}$ and $1 \times 10^{13}\,\mathrm{M}_{\odot}$ masses. We build the EPS merger tree using Cole et al. (2000a) method with an accretion limit of 0.1, merge probability of 0.1, mass resolution $1.408407 \times 10^{7}\,\mathrm{M}_{\odot}$ and recalibrated merger rates from Parkinson et al. (2008). Then we generate the EPS merger tree halo mass functions by implementing the method by Tinker et al. (2008) available in GALACTICUS.

Chapter 3

Constraining Star Formation Physics of The Milky Way Satellites

In this chapter, we describe the process of constraining the star formation physics of the Milky Way satellites using the SAM Galacticus. Large components of this chapter are drawn verbatim from Weerasooriya et al. (2023).

We determine the set of Galacticus' parameters that best fits the observed luminosity function and the luminosity metallicity relation for dwarf satellites of the Milky Way. We compare the galaxy models to the updated McConnachie (2012) table as of Jan 2021. [1]. In addition, we have added a few satellites from Drlica-Wagner et al. (2020) that are missing from McConnachie (2012). Note, we do not do any formal fitting. Instead, we run a grid of models and choose the ones that produce the best match based on a "by-

[1] https://www.cadc-ccda.hia-iha.nrc-cnrc.gc.ca/en/community/nearby/

eye" judgement. We start from GALACTICUS' standard set of parameters [2] constrained to match the baryonic physics of massive galaxies. Unless mentioned below, we use the parameters given in the file above. The parameters for massive galaxies have been calibrated to observational datasets, including the stellar mass halo relation of Leauthaud et al. (2012) and its scatter from More et al. (2009), the $z < 0.06$ stellar mass function of galaxies from the GAMA survey (Baldry et al. 2012), the $z = 2.5 - 3.0$ stellar mass functions of galaxies from the ULTRAVISTA survey (Muzzin et al. 2013), the $z = 0$ HI mass function of galaxies from the ALFALFA survey (Martin et al. 2010), the $z = 0$ black hole mass-bulge mass relation of Kormendy and Ho (2013), size distributions of SDSS galaxies from Shen et al. (2003), $H\alpha$ luminosity functions from HiZELS (Sobral et al. 2013) and GAMA (Gunawardhana et al. 2013), g and r-band luminosity functions of SDSS galaxies (Montero-Dorta and Prada 2009), the gas-phase mass-metallicity relation (Blanc et al. 2019), and the morphological fraction as a function of stellar mass from GAMA (Moffett et al. 2016).

In the following sections, we discuss how we systematically modify the parameters (Figure 3.1) and reproduce the observed luminosities and metallicities of the Milky Way satellites. We divide our discussion of the modified parameters into two subsets, those that are well-constrained by astrophysics governing dwarf galaxies or their properties (Section 3.1), and those that are not (Section 3.2).

[2] https://github.com/galacticusorg/galacticus/blob/889ab5d347001c9623d74609b51850c080829f96/parameters/baryonicPhysicsConstrained.xml

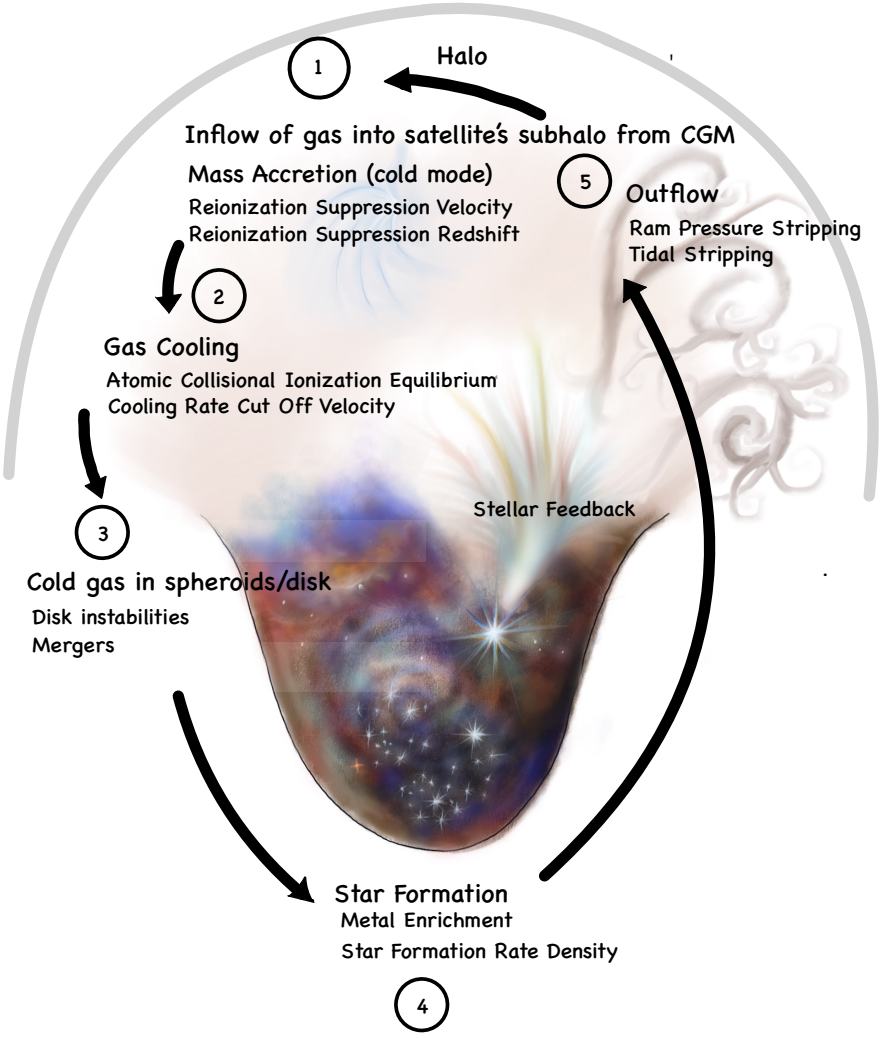

Figure 3.1: Diagram of the baryon cycle. Stage 1: Inflow of gas into the satellite's subhalo from CGM of parent Milky Way halo. Stage 2: Cooling of CGM gas in the subhalo and inflow to subhalo center to form a galaxy. Stage 3: the accreted material then provides gas for spheroid/disks. Stage 4: cold gas forms stars. Stage 5: finally, some of the gas within the satellite's subhalo flows back into the Milky Way halo's diffuse CGM due to tidal stripping, ram pressure stripping, and supernova feedback.

3.1 Parameters with Astrophysical Priors

We begin with parameters whose values are determined, or at least limited, by the astrophysics governing dwarf galaxies or the derived properties of the Milky Way.

3.1.1 Cooling velocity

Atomic hydrogen cooling is suppressed for low mass halos with virial temperatures below $\sim 10^4$ K. This is known as the atomic hydrogen cooling limit, which corresponds to a virial velocity of ~ 16 km/s (Fitts et al. 2017, Graus et al. 2019). To suppress star formation in the least massive halos, Galacticus uses a minimum $v_{\rm vir}$ below which gas in a halo will be unable to cool and form stars ($v_{\rm cooling}$). In this work, we choose $v_{\rm cooling}$ values to approximate this atomic cooling limit since gas accretion onto and star formation in halos below the atomic cooling limit is inefficient. Similar thresholds have been used in several high resolution hydrodynamic simulations (Sawala et al. 2016, Munshi et al. 2017, Benítez-Llambay et al. 2017, Fitts et al. 2017, Macciò et al. 2017). Note that the Collisional Ionization Equilibrium (CIE) cooling function does not drop entirely to zero below this threshold due to contributions from metal cooling. Modeling star formation in halos below the atomic cooling threshold requires accounting for the stochastic effects of H_2 cooling, and is beyond the scope of the current work. Therefore, we only consider halos that are above the atomic cooling limit and narrow our choices of velocities ($v_{\rm cooling} = 15 \ - \ 20$ km s^{-1}).

3.1.2 Reionization redshift

The redshift of reionization for the Milky Way and its local environment is set at $z_{\rm reion} = 9$. This value falls within the range of reionization redshifts calculated by previous works (Gnedin 2000, Bullock et al. 2000, Alvarez et al. 2009, Busha et al. 2010, Iliev et al. 2011, Spitler et al. 2012, Ocvirk et al. 2013, Li et al. 2014, Aubert et al. 2018).

3.1.3 Filtering velocity

During and after reionization the reheating of the IGM suppresses the accretion of gas onto low mass halos below the filtering mass (Ricotti and Gnedin 2005). Galacticus parameterizes this with the reionization suppression velocity $v_{\rm filter}$. Therefore, accretion of gas is suppressed in halos with $v_{\rm virial} \leq v_{\rm filter}$. Note that in this case accretion is completely turned off. When modelling the effects of reionization on halos across a range of redshifts, this criterion is the superior choice (compared to, for example, a halo mass-based criterion) since the virial velocity of a halo is a direct and redshift-independent measure of the depth of the potential well.

3.1.4 Star formation law in disks

We calculate the star formation rate density for the disks using the model of Blitz and Rosolowsky (2006). We choose this prescription because it is based on the astrophysics of molecular hydrogen as opposed to fits of observed data from more massive galaxies

(Kennicutt 1998, Shi et al. 2011). This method describes a star formation prescription based on hydrostatic pressure. It uses the linear relation between pressure and the ratio of molecular to atomic gas in galaxies. The star formation rate surface density is computed by

$$\dot{\Sigma}_*(R) = \nu_{\rm SF}(R)\Sigma_{\rm H_2,disk}(R). \tag{3.1}$$

Here the star formation frequency is given by $\nu_{\rm SF}(R) = \nu_{\rm SF,0}\left[1 + \left(\frac{\Sigma_{\rm HI}}{\Sigma_0}\right)^q\right]$, where Σ_0 is the critical surface density for formation of molecules and q is an exponent. Note that the star formation efficiency is suppressed in 'subcritical' regions where $\Sigma_{\rm HI} < \Sigma_0$. The surface density of molecular gas is given by

$$\Sigma_{\rm H_2} = \left(\frac{P_{\rm ext}}{P_0}\right)^\alpha \Sigma_{\rm HI}, \tag{3.2}$$

where P_0 is the characteristic pressure and α is the pressure exponent (we use $\alpha = 0.92$ as suggested by Blitz and Rosolowsky (2006)). External hydro-static pressure within a gas cloud in the disk is calculated by

$$P_{\rm ext} = \frac{\pi}{4} G\Sigma_{\rm gas}\left[\Sigma_{\rm gas} + \left(\frac{\sigma_{\rm gas}}{\sigma_*}\right)\Sigma_*\right], \tag{3.3}$$

where $\sigma_* = \sqrt{\pi G h_* \Sigma_*}$ is the surface density of the stars and h_* is the disk scale height. Note that this equation is valid only under the condition $\Sigma_* \gg \Sigma_{\rm gas}$. We do not vary any parameters for this prescription.

3.1.5 Star formation in spheroids

Star formation rates in spheroids are calculated using dynamical times with the same parameters used for the best fit to the more massive galaxies. The timescale for star formation is given by

$$\tau_* = \epsilon_*^{-1} \tau_{\rm dynamical} \left(\frac{V_{char}}{200\,{\rm km/s}} \right)^{\alpha_*}, \tag{3.4}$$

where ϵ_* (efficiency) and α_* (exponent velocity) are default input parameters, and $\tau_{\rm dynamical} = r/V$ where r and V_{char} are the characteristic radius and velocity of the spheroidal component, respectively. This timescale cannot fall below a minimum value of 7.579 Gyrs. Gas can be added to the spheroid via mergers and disk instabilities. In a major merger, both galaxies are destroyed and a new spheroid is created with combined gas from destroyed galaxies, while in a minor merger, gas from the merging satellite is added to the more massive spheroid. Note that we do not vary any parameters for this method. We use the default values for each parameter given in Galacticus documentation.

3.1.6 Accretion mode onto halos

Gas can accrete onto halos in one of two 'modes': 'cold' and 'hot'. In 'hot-mode' accretion, all accreted gas is shock heated to the virial temperature of the halo. Although this model describes the process of accretion well for higher mass halos, gas accretion in low mass halos (dwarfs) is never shock heated to the virial temperature (Fardal et al. 2001, Kereš et al. 2005; 2009). Studies such as Kereš et al. (2005; 2009) show that 'cold-mode' gas accretion dominates low mass galaxies (i.e. $< 10^{10.3}$ $M_\odot$) while 'hot-mode' accretion of

gas occurs in higher mass systems. In 'cold-mode' accretion, the gas accreted never forms a hydrostatic halo, and so does not need to cool and radiate its thermal energy before flowing into the galaxy. It instead flows into the galaxy on order of the dynamical time. Therefore, we implement 'cold-mode' accretion onto low mass halos, 'hot-mode' accretion onto high mass halos, and a mixture of both to intermediate mass halos. The transition between two modes is determined by two 'shock' parameters.

According to Birnboim and Dekel (2003), Benson and Bower (2010), the cold-mode fraction is defined by

$$f_{\rm cold} = (1 + r^{\frac{1}{\delta}})^{-1}, \tag{3.5}$$

where δ is the shock stability transition width, $r = \epsilon_{\rm crit}/\epsilon$ and $\epsilon = r_{\rm s}\Lambda\rho_s v_s^3$ where $r_{\rm s}$ is the accretion shock radius (set to the virial radius), Λ is the post-shock cooling function, $\rho_{\rm s}$ and $v_{\rm s}$ are pre-shock density and velocity (at the virial radius) respectively, and $\epsilon_{\rm crit}$ is the accretion shock stability threshold. Here, the pre-shock density is defined by

$$\rho_s = \frac{\gamma - 1}{\gamma + 1}\frac{3}{4\pi}\frac{\Omega_{\rm b}}{\Omega_{\rm m}}\frac{M}{r_{\rm s}^3}\left[1 + \frac{(\alpha + 3)(10 + 9\pi)}{4}\right]^{-1}, \tag{3.6}$$

where M is the total halo mass, $\gamma = 5/3$ is the adiabatic index of gas, and α is the exponent that corresponds to initial density perturbation (Birnboim and Dekel 2003). Note that while we choose the cold-mode method for accretion, the parameters above are not variable and are set by internal calculations.

3.2 Parameters without Astrophysical Priors

We next describe the parameters that are unconstrained by the underlying astrophysics of either dwarf galaxies or the Milky Way. Ram pressure and tidal stripping were constrained by comparisons to the observed and simulated (Applebaum et al. 2021, Shipp et al. 2022) luminosity functions of the Milky Way satellites. The physics of star formation feedback is constrained to best fit the slope and scatter of the luminosity-metallicity relation.

3.2.1 Ram Pressure Stripping

We use the model of Font et al. (2008) to model ram pressure stripping of hot halo gas in our dwarf galaxies as this method sets a physical radius within the dwarf galaxy halo. The ram pressure stripping radius of Font et al. (2008) is a solution to

$$\alpha_{rp}\frac{GM_{\rm satellite}(r_{\rm rp})\rho_{\rm hot,satellite}(r_{\rm rp})}{r_{\rm rp}} = \mathcal{F}_{\rm ram,hot,host}, \tag{3.7}$$

where $\mathcal{F}_{\rm ram,hot,host}$ is the ram pressure force due to the host halo, geometric factor α_{rp}. $\beta_{\rm ram} = \mathcal{F}_{\rm hot,host}/F_{gravity}$, and the total mass of the satellite within radius r, $M_{\rm satellite}(r)$. $\rho_{\rm hot,satellite}$ is the hot halo density profile of the node's host at pericenter radius $r_{\rm rp}$. The ram pressure force due to the hot halo is defined by

$$\mathcal{F}_{\rm ram,hot,host} = \rho_{hot,host}(r)v^2(r). \tag{3.8}$$

Mass loss rate in disks are computed using the equation

$$\dot{M}_{\rm gas,disk} = \min\left(\frac{\mathcal{F}_{\rm hot,host}}{2\pi G\Sigma_{\rm gas}(r_{1/2})\Sigma_{\rm total}(r_{1/2})}, R_{\rm max}\right)\frac{M_{\rm gas,disk}}{\tau_{\rm dyn,disk}}, \tag{3.9}$$

where $\beta_{\rm ram} = \mathcal{F}_{\rm hot,host}/F_{gravity}$ is the ram pressure stripping efficiency that scales the mass loss in the disk, $\Sigma_{gas}(r)$ is the gas surface density in the disk, $\Sigma_{total}(r)$ is the total surface density in the disk, $r_{1/2}$ is the disk half mass radius, $M_{gas,disk}$ is the total gas mass in the disk, $\tau_{dyn,disk} = r_{disk}/v_{disk}$ is the dynamical time in the disk, R_{max} is a unitless constant that determines the maximum rate of gas mass lost. A maximum flow rate is chosen as it is difficult to remove gas on a scale that is less than the sound crossing time. If the timescale for gas removal is too short, the step sizes becomes extremely small making it difficult to numerically solve equations. Therefore a minimum of two quantities for a flow rate is used. G is the gravitational constant.

In spheroids, the rate of gas mass loss is calculated using

$$\dot{M}_{\rm gas,sph} = -\max(\beta_{ram}, R_{\rm max})M_{\rm gas}/\tau_{\rm sph}, \tag{3.10}$$

where $M_{\rm gas}$ is the mass of gas in spheroid and $\tau_{\rm sph}$ is the dynamical time of the spheroid, and $\beta_{\rm ram} = \mathcal{F}_{\rm hot,host}/F_{gravity}$. The gravitational restoring force at half mass radius is given by,

$$F_{gravity} = \frac{4}{3}\rho_{\rm gas}(r_{1/2})\frac{GM_{\rm total}(r_{1/2})}{r_{1/2}} \tag{3.11}$$

3.2.2 Tidal Stripping

There is evidence for tidal stripping in dwarf satellites embedded in the scatter of the halo-stellar mass relation (Jackson et al. 2021) and the presence of tidal streams and debris (Bullock and Johnston 2005). Previous studies have shown that more dark matter must be stripped in order for stripping of stars to occur in galaxies with smaller disks (Peñarrubia et al. 2008, Smith et al. 2013). Simulations suggest that stars in dwarf spheroids are only stripped after $80 - 90\%$ of the dark matter is stripped (Smith et al. 2013). In addition, galaxies that lose 80% of dark matter mass lose about 10% of their stellar mass (Smith et al. 2016). As such, tidal stripping of dark matter precedes tidal stripping of stars.

We approximate stellar mass and ISM gas loss via tidal stripping treatment using the 'simple' model in Galacticus. This model assumes the stellar mass loss rate scales with the ratio of tidal force to restoring force in a galaxy at half mass radius, and is inversely proportional to the dynamical timescale

$$\dot{M}_* = \beta_{\rm tidal} \frac{F_{\rm tidal}}{F_{\rm res}} \frac{1}{T_{\rm dyn}} M_*, \tag{3.12}$$

where $\beta_{\rm tidal}$ is the strength of tidal stripping of ISM and stars, $F_{\rm tidal}$ is the tidal force, $F_{\rm res}$ is the restoring force, $T_{\rm dyn}$ is the dynamical time of stars, and M_* is the stellar mass. Note that this model only captures the effects of tidal stripping on the total mass and ignores the effects on the shape of the galaxy's density profile.

3.2.3 Stellar Feedback

We next determine the parameterization of stellar feedback that best produces the observed luminosity-metallicity relation. Stellar feedback from the disk and spheroid components are treated separately, but with the same model, parameterized by a characteristic velocity and exponent. The characteristic velocity defines the scale at which supernovae feedback results in a mass loading factor (the ratio of the outflow rate to the star formation rate) is one. The outflow rate is then given by

$$\dot{M}_{\rm outflow} = \left(\frac{v_{\rm charac}}{v_{\rm rs}} \right)^{\alpha_{\rm outflow}} \frac{\dot{E}_*}{\epsilon_{\rm cannonical*}}, \tag{3.13}$$

where $v_{\rm charac}$ (the circular velocity at which the mass outflow rate driven by supernovae equals the star formation rate in the disk/spheroid) at scale radius, $v_{\rm rs}$ is the disk/spheroid circular characteristic velocity at scale radius, and $\alpha_{\rm outflow}$, the disk/spheroid exponent. These are tunable parameters except for v_{rs}. $\dot{E}_*$ is the rate of energy input from stellar populations, and $\epsilon_{\rm cannonical*} = 4.517 \times 10^5 (km/s)^2$ is the total energy input by a canonical stellar population normalized to 1 $M_\odot$ after infinite time (Note that Galacticus calculates $\epsilon_{\rm cannonical*}$ for a Salpeter IMF and it serves only as a plausible scale). For a typical low mass dwarf, the ratio of v_{charac}/v_{rs} would be higher, thus more mass would escape its potential well, whereas a higher mass dwarf would have a lower ratio. The best fit parameters described above are summarized in Table 3.2.3.

We initially explore whether there is a set of input parameters for which running Galacticus on high resolution N-body merger trees can reproduce the luminosities and metallicities of the Milky Way dwarfs.

Table 3.1. Summary of the Semi-analytic Model Parameters

Notation	Meaning of Parameter	Range of Parameters	Best fit value
v_{filter}	Reionization suppression velocity	$20, 25, 30\ km/s$	$25\,km/s$
$v_{\rm cooling}$	Cooling rate cut off velocity	$15 - 20\ km/s$	$19\,km/s$
$\dot{\Sigma}_{\rm SF}$	Star formation rate surface density	Extended Schmidt	$e_* = 0.5$, $e_{\rm gas} = 1.09$
...	...	Blitz Rosolowsky	Blitz Rosolowsky $\alpha = 0.92$
...	...	$\alpha = 0.92$	
...	...	Kennicutt Schmidt	
...	...	$e_* = 0.5$, $e_{\rm gas} = 1.09$	
...	...	Krumholz McKee Tumlinson	
...	...	$f = 0.385$, $C = 5$	
v_{charac}	Characteristic velocity (disk)	$60, 160, 260\ km/s$	$160\ km/s$
v_{charac}	Characteristic velocity (sph)	$51, 151, 251\ km/s$	$151\ km/s$
$\alpha_{outflow,disk}$	Outflow velocity exponent (disk)	1.7,2.2, 2.7	1.7
$\alpha_{outflow,sph}$	Outflow velocity exponent (spheroid)	0.3,0.8,1.3	0.3
β_{ram}	Ram pressure stripping efficiency	0.01,0.1,1.0	1.00
β_{tidal}	Tidal stripping efficiency	0.01,0.1,1.0	0.01

Note. — The first column lists the notation for parameters used in the SAM. Second column explains the meaning of each parameter. Third column lists the range of tested values. Fourth column lists the best fit values found.

3.3 Cumulative Luminosity Function

We begin our exploration of the best fit GALACTICUS parameters by determining the combination of $v_{\rm cooling}$ and $v_{\rm filter}$ that best reproduce the observed luminosity function of the Milky Way dwarfs and the simulated luminosity functions from the Mint Justice League (Applebaum et al. 2021) and FIRE II mock observations (Shipp et al. 2022). For Mint Justice League, we use Sandra (2.4×10^{12} $M_\odot$) and Elena (7.5×10^{11} $M_\odot$) since they are the only simulations run at Mint resolution ($M_V < -5$). They also have virial masses closest to our Milky Way analog (1.8×10^{12} $M_\odot$ or 1.2×10^{12} $M_\odot/h$). We compare our models to 3 Milky Way analogs (m12f, m12m, m12i) of FIRE II hydrodynamic simulations These simulations resolve halos down to mass scales corresponding to a hosted galaxy luminosity of $M_V < -8$. Masses of m12f, m12m, m12i are 1.7×10^{12} $M_\odot$, 1.6×10^{12} $M_\odot$, 1.2×10^{12} $M_\odot$ respectively. While the luminosity functions of the hydrodynamical simulations might

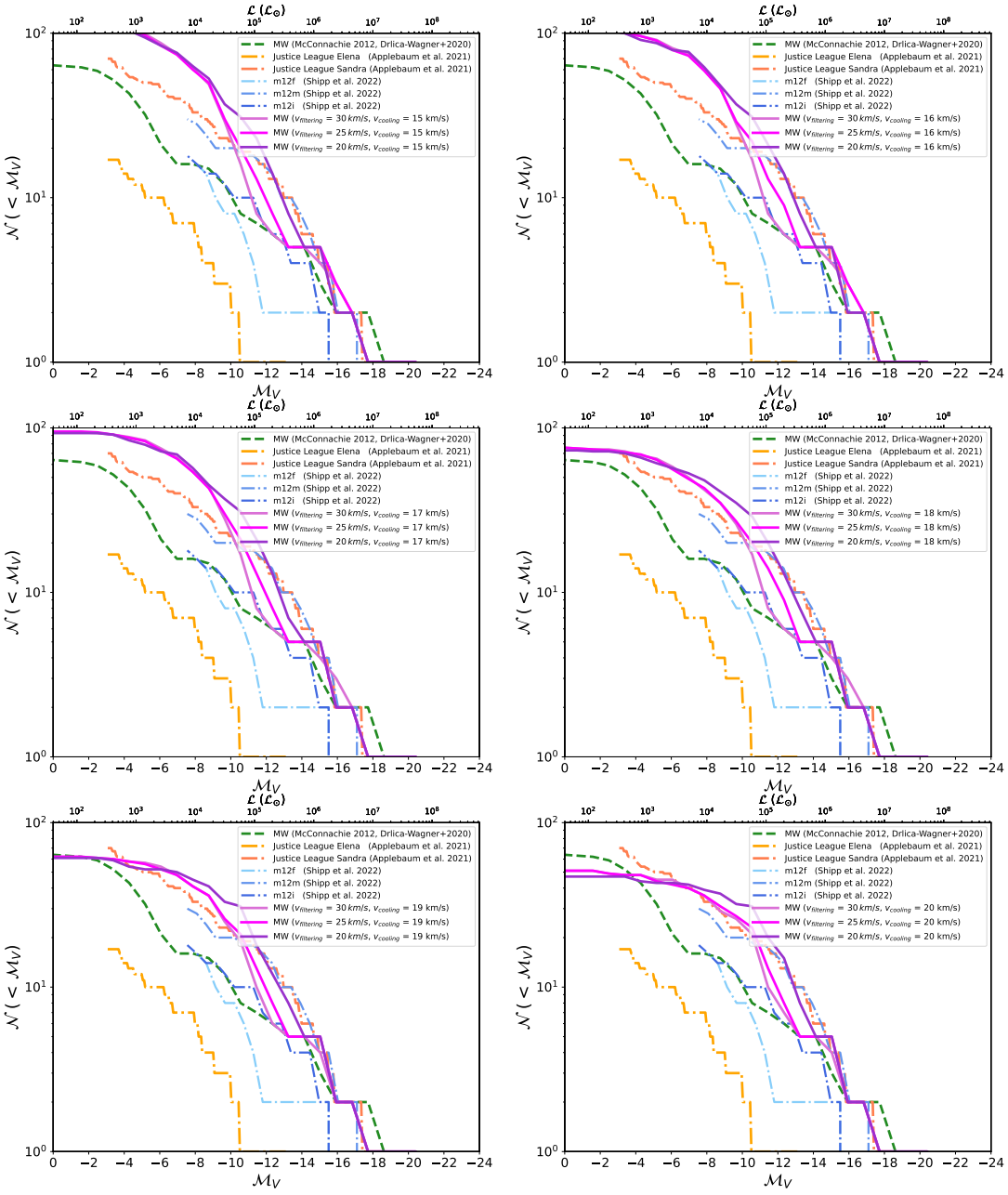

Figure 3.2: Cumulative luminosity function of the Milky Way dwarf satellite galaxies. M_V denotes the absolute V band magnitude and $\mathcal{N}$ denotes the cumulative number of galaxies fainter than M_V. The dark green dashed line shows the observed data from McConnachie (2012), Drlica-Wagner et al. (2020). Each figure corresponds to GALACTICUS runs with cooling rate cutoff velocities from $15 - 20\,km\,s^{-1}$. These predicted luminosity functions correspond to $v_{\rm filter} = 20, 25, 30\,km/s$ are then are compared to Justice League hydro simulations (shown in orange and coral), and mock observations of FIRE II hydro simulations (in shades of green) along with observations.

undercount the number of ultra-faint dwarfs due to over merging (Graus et al. 2019), they do not have the completeness issues of the observation sample (Drlica-Wagner et al. 2020). However, these Milky Way analogs of hydrodynamic simulations are of different masses and merger histories, thus may not necessarily resemble the exact Milky Way satellite population. Therefore, we cannot perform a quantitative comparison of curves for observations and different models. Instead, we compare all the luminosity function curves and determine an expected best fit curve 'by-eye'.

Figure 3.2 shows the luminosity function of the satellites in our Milky Way analog modeled by GALACTICUS with $v_{\rm cooling} = 15 - 20$ km s^{-1} and $v_{\rm filter} = 20 - 30$ km s^{-1}. It shows the effect of our choices of $v_{\rm cooling}$ and $v_{\rm filter}$, for $z_{\rm reion} = 9$. The filtering velocity is only allowed to range from 20 km s^{-1} to 30 km s^{-1} (Gnedin and Kravtsov 2006, Bovill and Ricotti 2011). The choice of the range of $v_{\rm cooling}$ and $v_{\rm filter}$ approximates the known physics that suppresses gas accretion and cooling in low mass halos. In this work, we hold the reionization redshift of the Milky Way constant.

To determine the combinations of $v_{\rm cooling}$ and $v_{\rm filter}$ that produce the best agreement with the known Milky Way satellite population, we compare our models to the observed luminosity function (McConnachie 2012, Drlica-Wagner et al. 2020) and the simulated luminosity function from the two halos in the Mint Justice League (Applebaum et al. 2021) simulations. The latter minimizes the complications due to the incompleteness of the sample of Milky Way satellites, especially at $M_V > -10$ (Willman et al. 2004). Note that we use the updated version of McConnachie (2012) as of January 2021. Drlica-Wagner et al. (2020) attempts to correct for the survey incompleteness to find the total number of dwarfs in DES and Pan-STARRS1(PS1) surveys. We find that $v_{\rm cooling}$ plays

a critical role in producing the correct number of dwarf galaxies fainter than $M_{\rm V} \geq -8$, while $v_{\rm filter}$ primarily affects brighter dwarfs. Our model produces the best fit to the luminosity function of the Milky Way satellites ($M_{\rm V} < -6$) and Sandra (Applebaum et al. 2021) for $v_{\rm cooling} = 18 - 19$ km s^{-1} with $v_{\rm filter} = 25$ km s^{-1}.

We note that the observed Milky Way satellites are certainly incomplete below $M_V \sim -10$. For our best fit model, we match galaxies brighter than $M_V = -6$ and fainter than $M_V = -12$. Note that we slightly overproduce the number of galaxies in the range of $M_V = -12$ and $M_V = -16$ (Figure 3.2 bottom left panel, Milky Way - $V_{filter} = 25\,km/s$, $v_{cooling} = 19\,km/s$). In addition, the number of brighter satellites are under-predicted in comparison to observations and hydrodynamic simulations (middle line shown in pink). As the number of bright satellites around a Milky Way mass host is low, this might simply be due to small number statistics.

Notice that there is more than one set of parameters for $v_{\rm cooling}$ and $v_{\rm filter}$ that will produce a reasonable fit to the luminosity function of the observed Milky Way satellites and the Mint Justice League. Specifically, our fit is not improved markedly for $v_{\rm filter} = 25$–30 km/s and $v_{\rm cooling} \sim 18$–20 km/s. We consider a reasonable fit/curve as a model that lies within observed luminosity function and the number of dwarf satellites predicted by hydrodynamic simulations of MW analogs. Note that we cannot perform direct comparisons among our models, hydrodynamic simulations and observations using simultaneous fitting as these MW analogs have different masses/merger histories. However, they are sufficient to estimate the number of satellites based on 'eye-judgement'. See Starkenburg et al. (2013), Font et al. (2011), Applebaum et al. (2021) for similar comparisons. In this work, we choose our best fit value for $v_{\rm cooling}$ to approximate the atomic cooling threshold

during the epoch of reionization. Our 'best fit' $v_{\rm filter}$ is chosen to be the average of the values used in Ricotti and Gnedin (2005) and Bovill and Ricotti (2011).

In Figure 3.3 we compare the cumulative luminosity function for the Milky Way satellites computed with the Font et al. (2008) ram pressure stripping model (pink), to that computed in a model with no ram pressure stripping (purple).

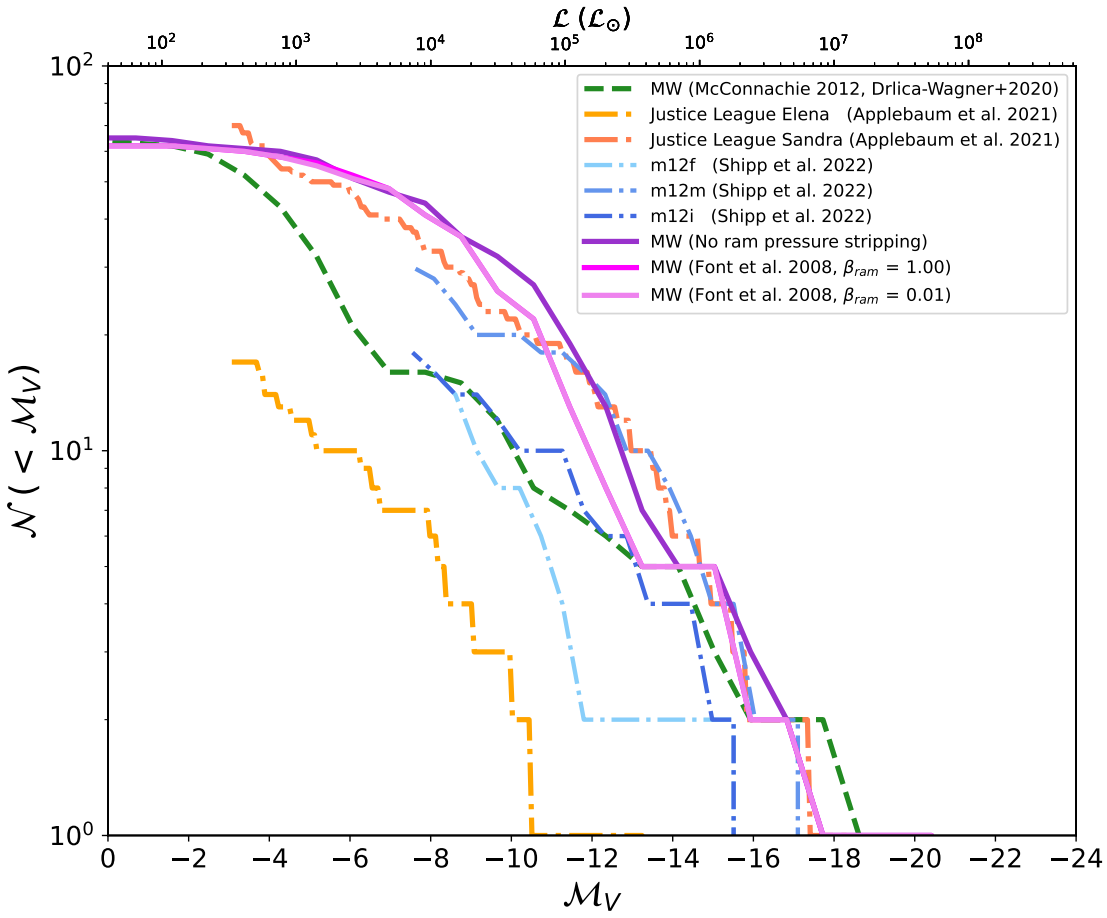

Figure 3.3: Cumulative luminosity function of the Milky Way satellites computed with ram pressure stripping methods (Font et al. 2008, pink) and $\beta_{ram} = 1.00$ (pink), no ram pressure stripping (purple), and the same method implemented with $\beta_{ram} = 0.01$ (blue). Other colors are the same as in Figure 3.2.

We now look at the effect of ram pressure stripping for our best fit cooling and filtering velocities. We vary the efficiency of the ram pressure stripping through its full

range from 0 to 1. However, the effect of $\beta_{ram} = 0.01$ seem to be same as $\beta_{ram} = 1.00$ i.e. the efficiency at which gas is stripped upon infall does not have a major effect on the luminosity except in the more massive dwarfs (see blue and pink curves of Figure 3.3). Note that, with the exception of some minor differences at high luminosity ($M_V < -14$), changing the efficiency of the ram pressure stripping does not significantly affect the luminosities of our modeled galaxies. This is expected, as only the most massive Milky Way dwarfs formed significant amounts of stars after their infall into the Milky Way halo (Rocha et al. 2012). While the effect of ram pressure efficiency is negligible, we chose the maximum ram pressure stripping efficiency of 1.0 as dwarf satellites undergo ram pressure stripping as they fall into their host galaxy.

We now move onto tidal stripping using the 'simple' model in GALACTICUS. Since, in the N-body simulation, there is already stripping of the dark matter halos, we do not implement any additional stripping of the dark matter.

The strength of tidal stripping of ISM gas and stars $\beta_{\rm tidal}$ can be varied from 0 to 1. Unlike ram pressure stripping, which was insensitive to our choice of β_{ram}, Figure 3.4 shows the effect on our luminosity function when the efficiency of tidal stripping is varied. While $\beta_{\rm tidal} \sim 0.1$ seems to better match with observed luminosity function, we select the model that is closest to Mint Justice League to account for the incompleteness of intermediate Milky Way satellites. We reproduce the observed and simulated (hydrodynamic) luminosity functions with $\beta_{\rm tidal} \sim 0.01$. We find a strong and direct, inverse relationship between the efficiency of the tidal stripping and the luminosity function of the Milky Way satellites (see Figure 3.4).

Note that the tidal force in the model is calculated at the pericenter of satellite's orbit.

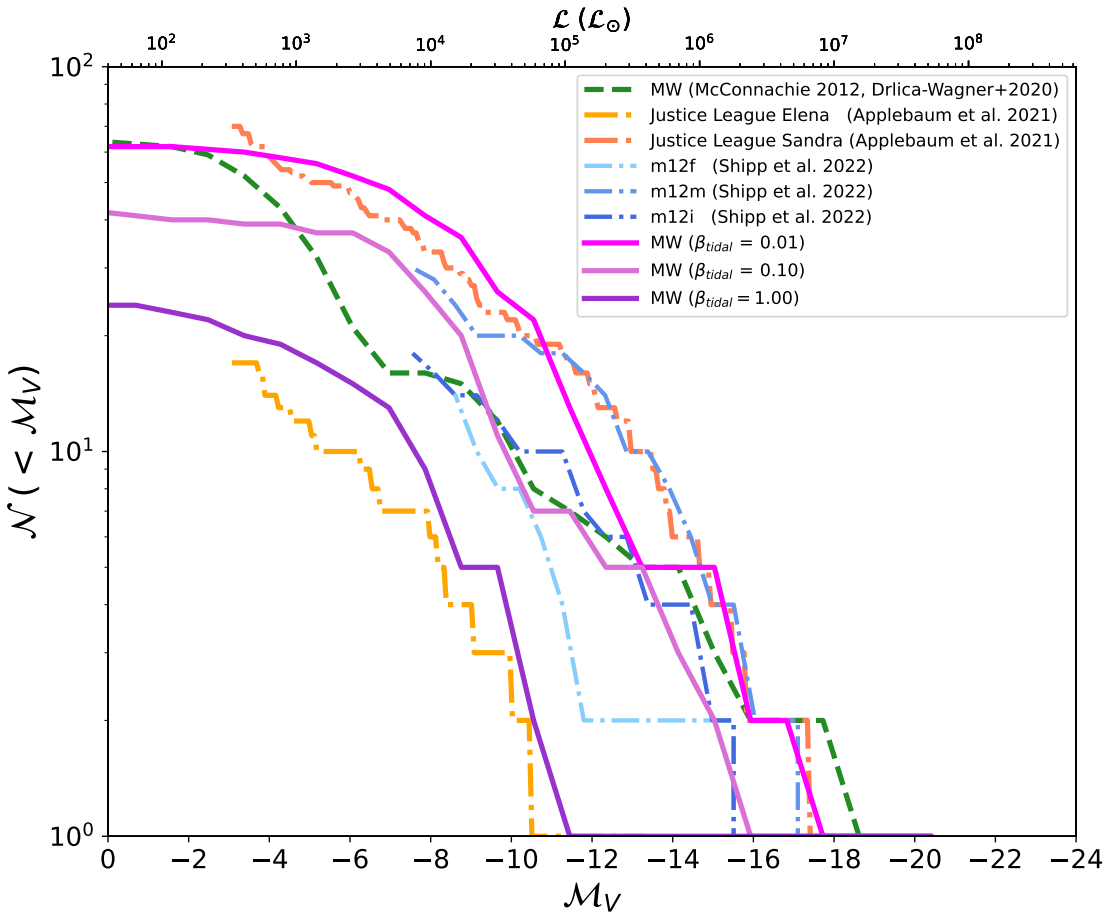

Figure 3.4: Luminosity function of Milky Way dwarfs for varying tidal stripping efficiencies. Three colors violet, fuchsia, and purple indicate tidal stripping efficiencies for stars and ISM gas ($\beta_{\rm tidal} = 0.01$, 0.1, and 1 respectively). Lower efficiency is in agreement with observations and results of 'Mint' resolution Justice League, and FIRE-II hydrodynamic simulations (colors are the same as in Fig 3.2).

Therefore the actual tidal force will likely be lower than our estimate. This means that $\beta_{\rm tidal} \ll 1$ is reasonable. In addition, models suggest the majority of the dark matter must be stripped before the stars are stripped (Peñarrubia et al. 2008, Smith et al. 2016). Since all the dwarf galaxies in our simulation exist in *intact* dark matter halos, this is in line with expectations from Peñarrubia et al. (2008) that $> 90\%$ of the dark matter halo needs to be stripped before the stars are significantly affected. Our model currently includes only a few halos that have been stripped to this level, thus low efficiency of tidal

stripping used here is in agreement with previous work.

We also note that our dark matter-only simulations may suffer from the missing satellite problem (Kauffmann et al. 1993, Klypin et al. 1999, Moore et al. 1999) and lack of modifications to halo concentrations due to baryonic effects. As such, correction models such as Schneider and Teyssier (2015) can be used to mimic the effects of baryons on the underlying dark matter halos.

3.4 Luminosity Metallicity

We next determine the combination of stellar feedback parameters that best reproduces the slope of the observed luminosity-metallicity relation (McConnachie 2012). We tune our model for $v_{\rm charac,disk} = 60, 160, 260\ km/s$ for the disk and $v_{\rm charac,sph} = 51, 151, 251\ km/s$ for the spheroidal component. Note that the values used in the standard set of parameters for the baryonic physics of higher mass galaxies described in section 2.1 are $v_{\rm charac,disk} = 160\ km/s$ and $v_{\rm charac,sph} = 151\ km/s$. Thus, we vary $\pm 100 km\, s^{-1}$ those values. We find that by tuning the existing stellar feedback recipes in Galacticus we can reproduce both the trend and scatter in the observed luminosity-metallicity relation (Figure 3.5). Critically, metallicities of the modeled dwarfs match well with observations down to the ultra-faint dwarfs. The two exponents, $\alpha_{\rm outflow,disk}$ and $\alpha_{\rm outflow,spheroid}$, and the characteristic circular velocity at the scale radius (v_{charac}) determine the scaling of the outflow rate of the corresponding disk/spheroid measured at the scale radius of that component. The characteristic velocity determines normalization of the luminosity-metallicity relation, and exponent of the disk, tunes the slope

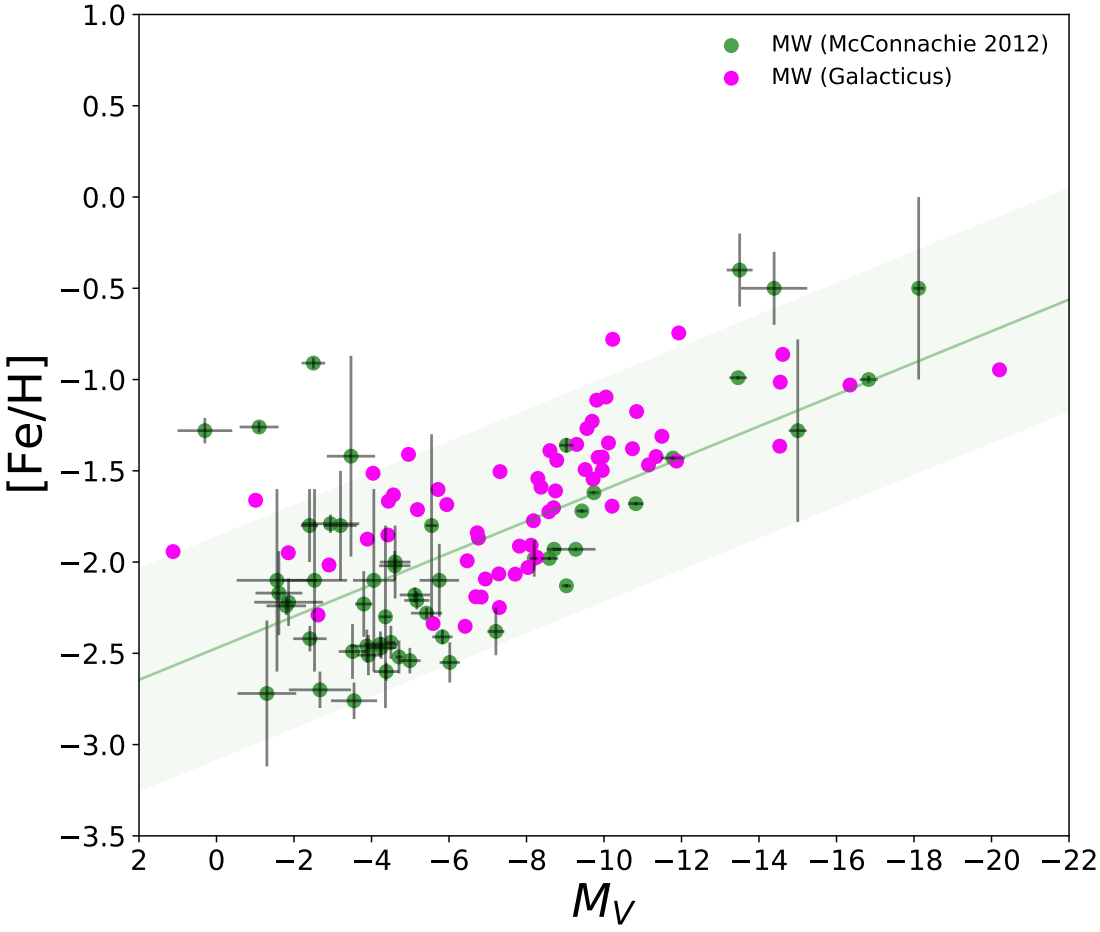

Figure 3.5: Iron abundance of the dwarf satellite galaxies as a function of absolute V-band magnitude. Observed data from McConnachie (2012) are green and dwarfs modeled with Galacticus are pink. Existing stellar feedback recipes in Galacticus have been calibrated to reproduce the luminosity-metallicity relation.

(Figure 3.6). Higher exponents correspond to steeper slopes and vice versa. In particular, low mass dwarf galaxies are sensitive to exponents controlling their supernova-driven outflows. We determine the slopes for luminosity metallicity relations using a Monte Carlo Marcov Chain (MCMC) fit and compare them 'by eye' judgement. The closest match to the slope to observed luminosity-metallicity relation is obtained for exponents $\alpha_{\rm outflow,disk} = 1.7$ and $\alpha_{\rm outflow,spheroid} = 0.3$ (see Figure 3.6).

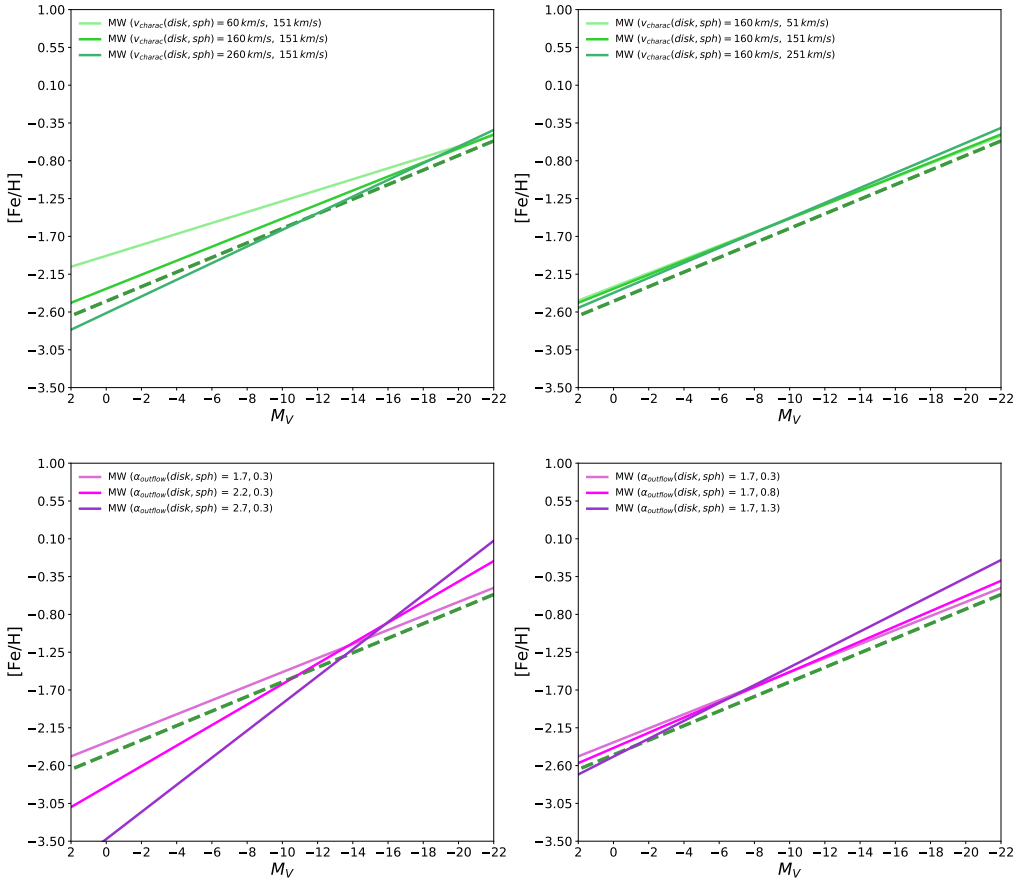

Figure 3.6: Modeled luminosity-metallicity relations for various characteristic velocities and exponents of stellar outflows. Top left and right figures show the effect of the characteristic velocity for the disk and spheroid components respectively. Bottom left and right figures show the effect of exponents on disk and spheroid components. Note that this relation is sensitive to both characteristic velocity (normalization) and exponents of the disk component (slope). The green dashed line shows the best fit line for the observed luminosity metallicity relation of McConnachie (2012).

As seen in Figure 3.6, while the exponent for the spheroid only marginally affects the slope of the luminosity-metallicity relation, the effect of tuning stellar feedback in the disk component is far greater. We find stellar feedback outflows to be a significant component for tuning the luminosity-metallicity relation. This agrees with Lu et al. (2015) who

demonstrated that metallicity of galaxies provides a constraint on the maximum outflow velocity ($\sim 141\ km/s$).

We have shown that with the correct set of astrophysical prescriptions and parameters Galacticus is able to reproduce the observed luminosity function and luminosity metallicity relation for the Milky Way dwarfs down to the ultra-faints. In Chapters 4 and 5 we explore whether those can reproduce other observed properties of the dwarfs at z = 0 and their star formation histories.

Chapter 4

Properties of The Milky Way Satellites at $z = 0$

In this chapter we present the properties of the Milky way satellites at $z = 0$ predicted by our dwarf galaxy models. Large parts of this chapter are drawn verbatim from Weerasooriya et al. (2023).

We have determined a set of parameters for Galacticus that reproduce the observed luminosities and metallicities of the Milky Way dwarfs. In this section, we determine if these parameters can reasonably reproduce other properties of the Milky Way dwarfs. Unlike the luminosity function and luminosity-metallicity relation discussed above, we have *not* tuned Galacticus to reproduce any of the dwarf galaxy properties below. All the observational data in this section comes from the updated table as of Jan 2021 originally published in McConnachie (2012).

4.1 Half Light Radii

As seen in Figure 4.1, we are able to match the observed half-light radii for the Milky Way satellites down to $M_{\rm V} \leq -6$. However, our modeled dwarfs have larger half-light radii for fainter, smaller dwarfs, and our modeled half-light radii do not reach below 200 *pc*. This 'floor' in our half-light radii roughly corresponds to the physical softening of our simulations (orange line in Figure 4.1).

In order to investigate this, we look at the half light radii as a function of dark matter halo mass (Figure 4.2). The vertical lines in Figure 4.2 show the dark matter halo masses for various numbers of particles per halo. Note that halos whose half-light radii are below the 'floor' corresponding to the physical softening of our simulation all have $>$ 1000 particles. As Galacticus calculates the $r_{\rm hl}$ of the halos by allowing the disk and spheroidal components to evolve within the gravitational potential of a dark matter profile, the determination of $r_{\rm hl}$ relies on a robust determination of the dark matter profile. The underlying NFW profile is set from scale radii of the simulation, where concentrations are calculated using the model by (Gao et al. 2008). The NFW profile describes the equilibrium radii for the disk and the spheroid components, and half-light radii are calculated in $g_{\rm SDSS}$ luminosity band. While the global properties of halos with $N < 1000$ particles are relatively certain (Trenti et al. 2010, Benson 2017a), the details of their dark matter profiles are not robust. For example, Mansfield and Avestruz (2021) show that convergence in measurements of half-mass radii of halos from N-body simulations requires $>$ 4000 particles. As the low mass halos that host the faintest dwarfs in our model have $N < 500$ particles, the uncertainties in the determination of

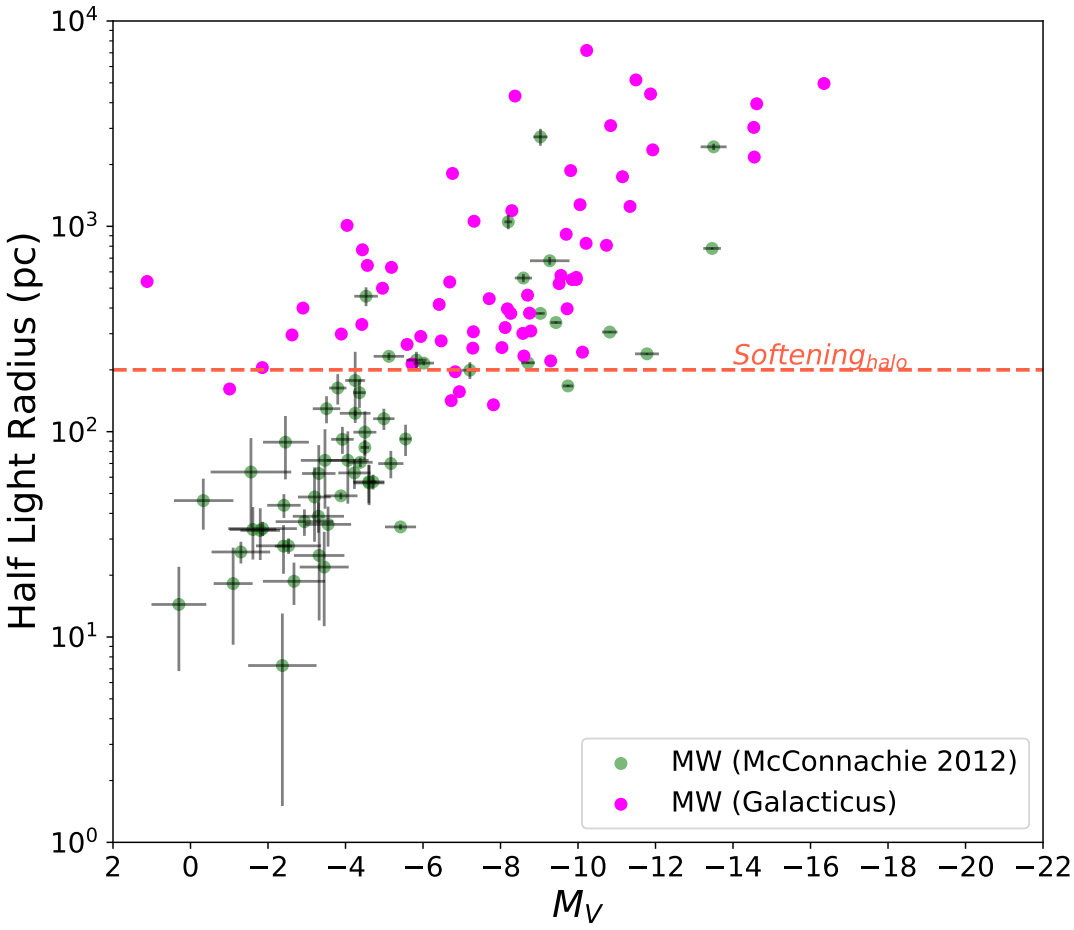

Figure 4.1: Half light radii of the dwarf satellite galaxies as a function of absolute V band magnitude. Observed data from McConnachie (2012) are colored in green, and simulated data are colored in pink. Orange dashed line shows the softening of the halo at 200 kpc in the N-body simulation.

their dark matter profile coupled with the physical gravitational softening used in the simulation produces a 'floor' of $\sim$ 200 *pc*. Similar effects of resolution are seen in the half-light radii of Mint Justice League simulations by Applebaum et al. (2021).

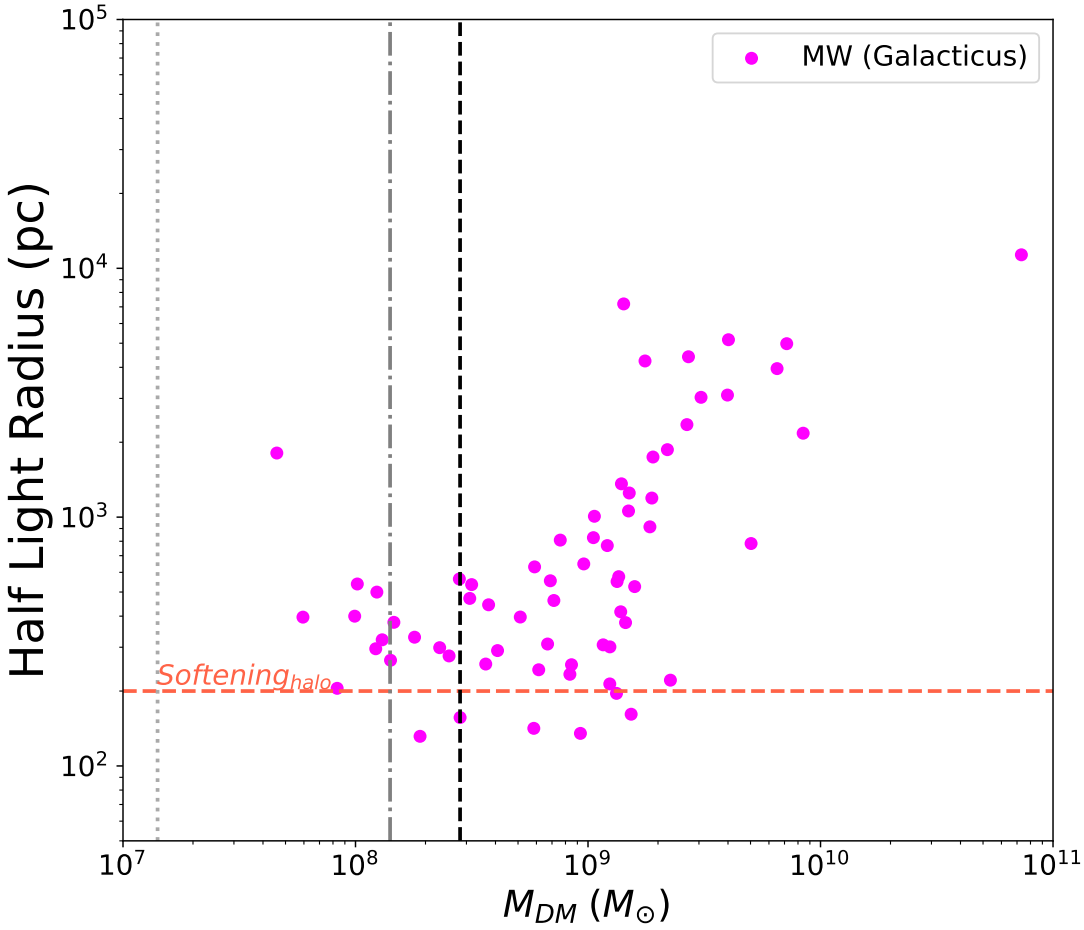

Figure 4.2: Half-light radii of the dwarf satellite galaxies as a function of dark matter halo mass. Here we show the dark matter mass of halos with 100 (light grey dotted), 1000 (dotted dashed line in dark grey), and 2000 (dashed line in black) particles. The orange dashed line shows the softening of the halo at 200 kpc in the N-body simulation. Note that most halos need $\sim$ 1000 dark matter particles in order to form luminous galaxies.

4.2 Velocity Dispersion

In this section, we look at the velocity dispersions of our modeled dwarfs at half-stellar mass radii compared to observations of McConnachie (2012) (updated as of Jan 2021) without any fitting. We determine any agreement between observations and our model 'by-eye'. Note that Galacticus calculates the velocity dispersion of each satellite galaxy

at its half mass radius. As seen in Figure 4.3, the stellar velocity dispersions of our predicted dwarfs agree well with observations. However, note that velocity dispersions of galaxies below $M_V \sim -8$ may be affected by the the floor in half-light radii discussed above.

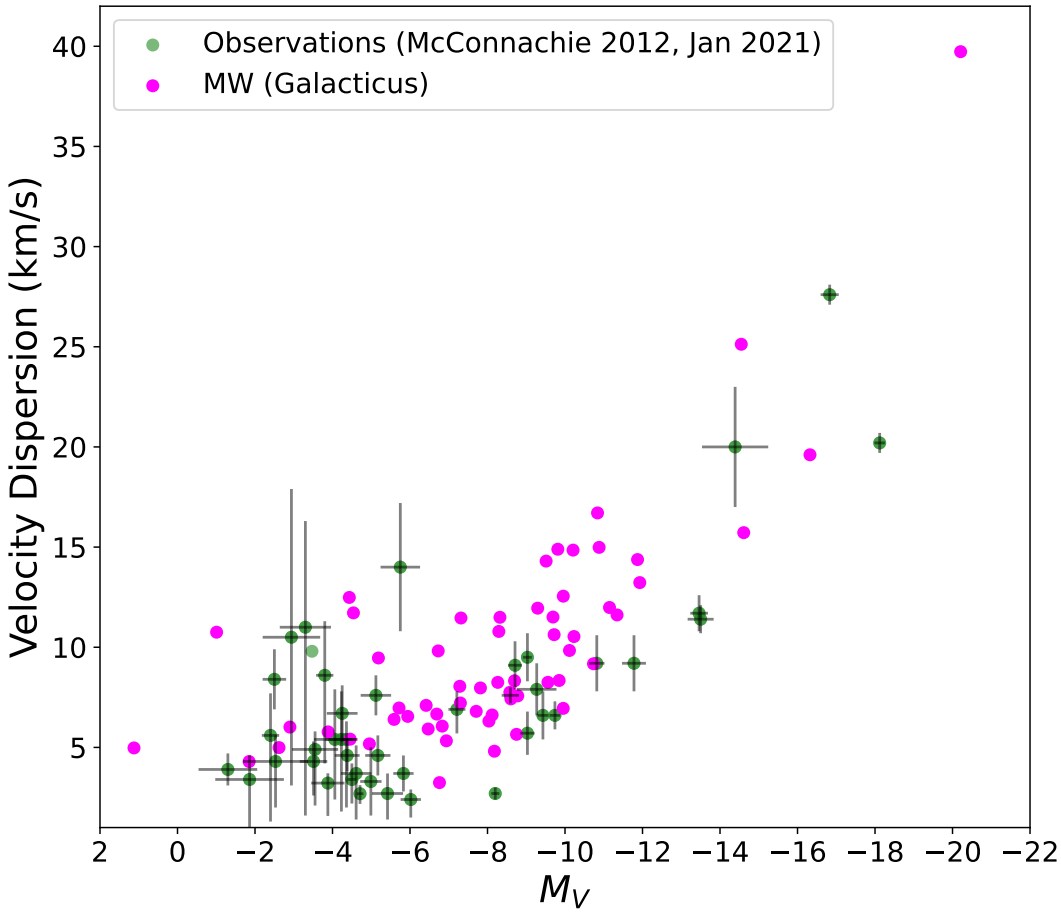

Figure 4.3: Velocity dispersion of the modeled and observed dwarf satellites as a function of absolute V band magnitude. Observed data from McConnachie (2012) are colored in green, and simulated data are colored in pink. Our model agree well with observations without additional tuning ('by-eye' judgement).

4.3 Mass to Light Ratios

Given that we are able to reasonably reproduce the half-light radii and velocity dispersion of the Milky Way dwarfs, we can estimate the mass-to-light ratios of the modeled Milky Way satellites using the equation 2 in Wolf et al. (2010).

$$M_{r_{1/2}} = 930\left(\frac{<\sigma^2_{los}>}{km^2 s^{-2}}\right)\left(\frac{r_e}{pc}\right) \tag{4.1}$$

where $r_e = 3/4 r_{half}$ is the 2D projected half light radius. While Galacticus does not calculate mass-to-light ratios directly, we use stellar velocity dispersions and half-light radii to calculate mass-to-light ratios. Our modeled mass-to-light ratios are in good agreement with values derived from observations (Figure 4.4). Critically, we are able to produce the dark matter domination of the ultra-faints dwarfs (Simon 2019). We quantify the offset in observational and simulation data using two regression lines (see Figure 4.4). The observations follow a slope of -0.182 and model follows a slope of -0.276. See Table 4.1 for slope and intercept of both model and observations. We find the root mean square error of 0.84 in log scale. While our model does not produce a good fit, this level of agreement is produced without further tuning of astrophysical prescriptions and parameters to our model. Previous SAMs have not reproduced or compared mass-to-light ratios of the Milky Way satellites. Therefore, this level of agreement with observations still exceeds our expectations.

Mass to Light	Slope	Intercept
Observations	-0.182	$10^{5.28}$
Model	-0.276	$10^{7.04}$

Table 4.1: Linear regression fit to mass to light ratios of observed and modeled dwarf galaxies of the Milky Way satellites.

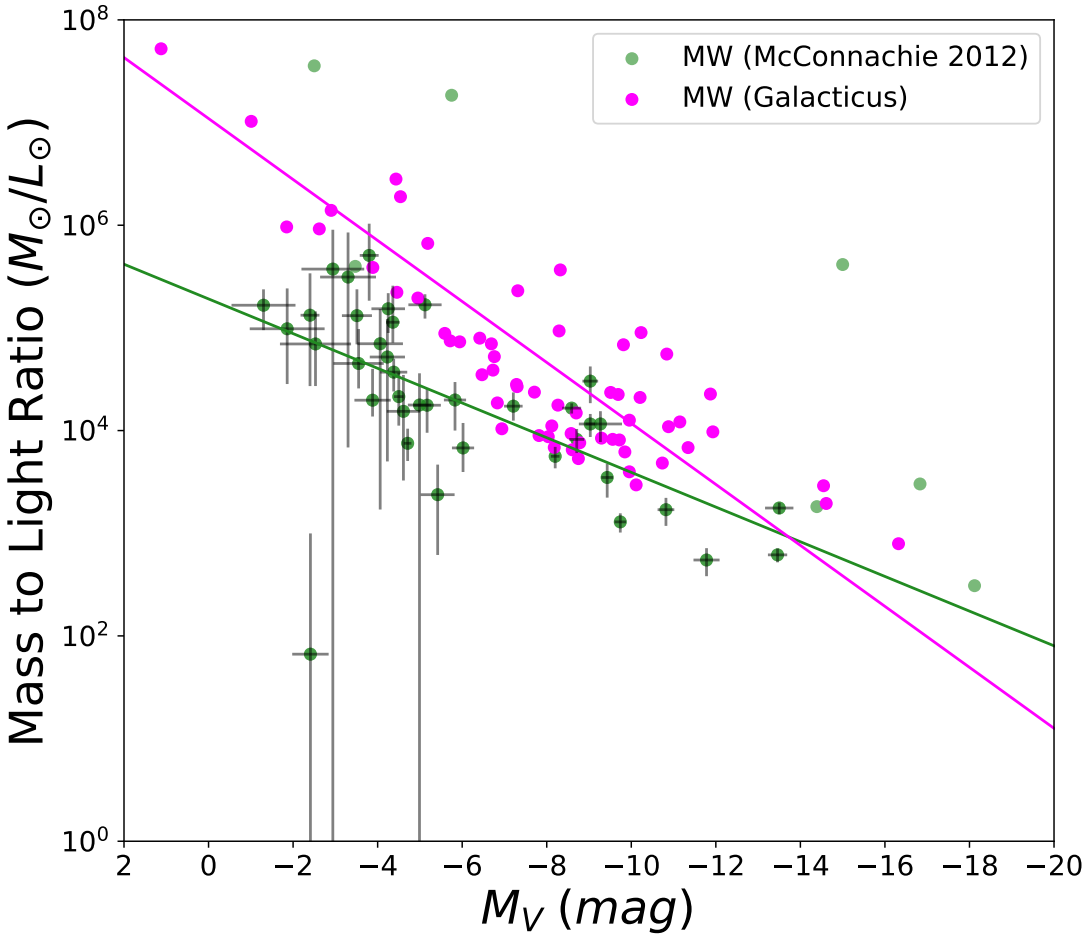

Figure 4.4: Mass to light ratios of the Milky Way satellites as a function of the velocity dispersion along the line of sight. Mass to light is calculated using the half mass with velocity dispersion and half-light radii as described in Wolf et al. (2010). We compare the modeled dwarfs (pink) to observed data from McConnachie (2012) (green). Green and pink lines show the linear regression lines for the observed and modeled dwarfs respectively. Mass to light ratios of the Milky Way satellites are in agreement down to the ultra faints, though our mass to light ratios are a bit higher than observed values.

4.4 Discussion

The well-studied Milky Way satellites are an ideal data set for constraining parameters of Galacticus to best model dwarf galaxies. The initial goal of this study was to build a viable model of the classical dwarfs in the Milky Way and explore predictions for their star formation histories with the standard implementation of Galacticus. However, in addition to successfully modeling the properties of the classical Milky Way satellites, we are also able to match the properties of the more luminous ultra-faint dwarfs. Reproducing the stellar properties of the Milky Way satellites, including the ultra-faint fossil galaxies, was unexpected due to the stochastic star formation processes that govern the evolution of the lowest mass galaxies (Guo et al. 2016).

Several previous studies of dwarf galaxies have been made using SAMs, most of which have found it challenging to reproduce a broad range of dwarf galaxy properties without significant modification to the SAM (e.g. Li et al. 2010, Macciò et al. 2010, Font et al. 2011, Lu et al. 2017, Starkenburg et al. 2013). For example, Lu et al. (2017) found that their SAM could not simultaneously produce a good match to the dwarf galaxy mass function and mass-metallicity relation without the introduction of a preventative feedback model that reduced the fraction of baryons accreting into a halo as a function of its mass and redshift of that halo. Note that Lu et al. (2017) use a relatively simple treatment of subhalos: their model removes Circum Galactic Medium (CGM) gas from a halo and transfer to the parent halo as soon as a halo becomes a subhalo. While Galacticus does stop accreting gas onto subhalos, it retains the remaining CGM gas that will continue to cool and supply gas to the subhalo, removing it only gradually via

ram pressure stripping etc.

The study by Pandya et al. (2020) found their SAM predicted gas accretion rates orders of magnitudes higher than those found in the FIRE II simulations (Hopkins et al. 2014a; 2018a), and were driven to allow stellar feedback to heat gas surrounding halos and thereby preventing it from accreting at such high rates. They also emphasized the possibility of obtaining the same final stellar/ISM mass with different combinations of outflows (e.g. high inflow + high outflow, low inflow + low outflow). Thus, they highlighted the importance of comparing the gas accretion, and outflow rates between models/simulations and observations rather than just bulk integrated properties. Note that their study focused on relatively isolated central dwarfs not satellites of Milky Way analogs. While we have not explored gas accretion rates in this paper, we *have* examined the luminosity function and mass-metallicity relation—essentially the diagnostics used by Lu et al. (2017). Interestingly, we do not find the need for any preventative feedback to simultaneously match both of these quantities.

The reasons preventative feedback is not necessary are not immediately clear. While the physics ingredients of the Galacticus SAM are fundamentally very similar to the SAMs of both Lu et al. (2017) and Pandya et al. (2020), there are differences in the details of the physics models. Additionally, there are differences in the numerical implementations of models (e.g. Galacticus uses an adaptive timestep ODE solver, while the SAMs of Lu et al. (2017) and Pandya et al. (2020) use fixed steps, often with each physical process applied in succession, rather than simultaneously). Identifying the primary reason preventive feedback is not needed in Galacticus is a key question, but one that requires an extensive study that is beyond the scope of this present work. Fortunately, the flexible,

modular nature of Galacticus allows the possibility of constructing models that mimic the SAMs of Lu et al. (2017) and Pandya et al. (2020)—this will allow us to explore in detail which physical or numerical choices lead to these different conclusions. We intend to undertake such a detailed study in a follow-up work.

4.5 Conclusions

Our conclusions on $z = 0$ properties are as follows.

- Despite the lack of H_2 cooling in our current model, we successfully model the properties of the most luminous of the ultra-faint fossil dwarfs.
- When our model is tuned to reproduce the observed luminosity function and luminosity-metallicity relation, we are able to independently reproduce several $z = 0$ properties of the Milky Way dwarfs, including half light radii, velocity dispersion and mass to light ratios without any additional tuning of the physics.

This chapter shows that the same astrophysical prescriptions and parameters that reproduce luminosity function and the luminosity metallicity relation down to the ultra faint dwarfs can also reproduce additional $z = 0$ properties of the Milky Way dwarf galaxies.

Chapter 5

Star Formation Histories of The Milky Way Satellites

In this chapter, we present the star formation histories of the dwarf galaxy models of our Milky Way analog. Large components of this chapter are drawn verbatim from Weerasooriya et al. (2023).

5.1 Cumulative Star Formation Histories (SFHs)

We have shown that by constraining Galacticus to reproduce the luminosities and metallicities of both the classical and ultra-faint dwarfs, we are able to successfully reproduce a wide range of observed Milky Way dwarf properties at $z = 0$. As a final test, we determine whether we are able to reproduce star formation histories that match those derived from observations (Weisz et al. 2014; 2015). Cumulative star formation history gives the total accumulated mass of stars in a particular galaxy throughout time.

We begin by looking at the cumulative star formation histories of the Milky Way dwarfs grouped by $z = 0$ absolute V band magnitude (Figure 6.7). Each curve is color-coded by absolute V band magnitude of a particular halo at $z = 0$.

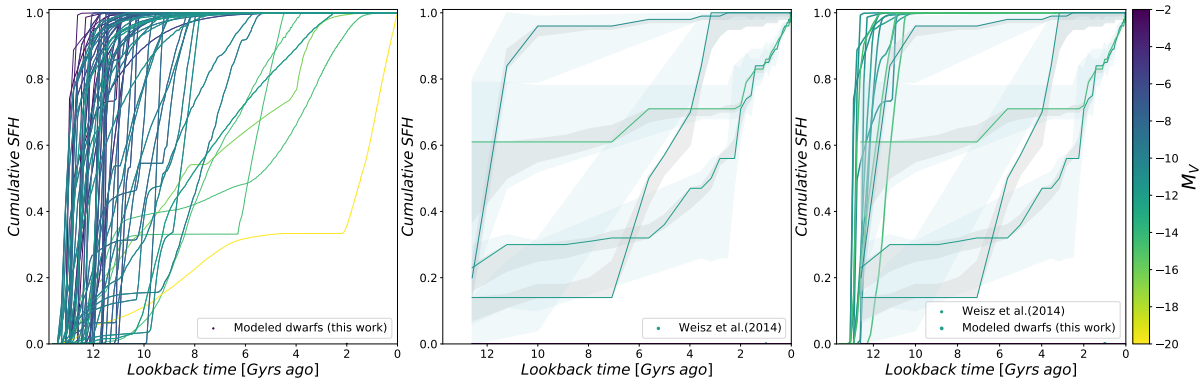

Figure 5.1: Cumulative star formation histories (SFHs) of the Milky Way satellites colored by absolute V band magnitude. The left panel shows the SFHs modeled with Galacticus and the middle panel shows observed SFHs for Leo A, Sagittarius, Sex A, and Sculptor by Weisz et al. (2014). Note that we plot only the SFHs of the Milky Way satellites from a list of combined SFHs of dwarfs of the LG with multiple fields in Weisz et al. (2014). While not intentional, brightness of this observed sample of galaxies are similar. The shaded regions in the middle and right panels show the region between the 16th and 84th percentiles in SFH uncertainties (grey for random uncertainty and blue for total uncertainty). In the right panel we plot SFH of models that have similar brightness to dwarfs of Weisz et al. (2014) along with observed SFHs from the 2nd panel (models are shown in thick lines while observations are shown in thin lines with envelopes for percentiles). While most observed dwarfs quench later except Sculptor, our models quench early ($\sim 11\,Gyrs\ ago$). Note, that Weisz et al. (2014) use isochrones older than the age of the universe, and sets the cumulative SFHs to 0 at $log(t) = 10.15\ Gyrs$. We have not made any correction to account for this in the modeled SFHs. Our cumulative SFHs are somewhat consistent with these results and the SFHs of the ultra-faints (Brown et al. 2014). However, since our models exclude H_2 cooling, we preclude comparison of modeled ultra faints to dwarfs of Brown et al. (2014).

As expected (Brown et al. 2014, Sacchi et al. 2021), fainter dwarfs ($M_V \geq -6$) accumulated the majority of their current stellar mass more than 11 ± 1 Gyrs ago. In contrast, the more luminous model dwarfs at $z = 0$ form their stars over longer periods of time, including some systems which are still star forming today. We note that some of the

modeled cumulative SFHs plateau around 0.1, 0.3, and 0.6 which is similar to observed SFHs of Weisz et al. (2014) shown in Figure 6.7. Note that all observed SFHs of dwarfs plotted in the middle and right panels of Figure 6.7 have similar luminosities. All of these dwarfs, other than Sculptor, quench later. However, our modeled dwarfs quench early, at $\sim 11 - 12\ Gyrs$. Cumulative star formation histories derived from GALACTICUS are consistent with the results of Mint Justice League simulations (Figure 11 of Applebaum et al. (2021)). Note that these 'mint' resolution DC justice league hydrodynamic simulations have the highest mass resolution Milky Way-like mass environments run to $z = 0$. Their SFHs agree well with observations of Brown et al. (2014), Weisz et al. (2014).

The faintest modeled dwarfs all have their star formation cut off at about the same time. This is expected as the faintest observed Milky Way satellites are the fossils of the first galaxies (Bovill and Ricotti 2011, Brown et al. 2012b). The larger range of the lookback time of the truncation of star formation for the more luminous dwarfs is consistent with their star formation being shut off upon accretion into the Milky Way halo. Note that these dwarfs are reflective of the surviving sample of dwarfs that we observe.

5.2 τ_{90} vs. τ_{50}

We next look at quenching times of these dwarf galaxies, specifically, the time for a galaxy to gain 90% its current stellar mass (τ_{90}) and for a galaxy to gain 50% its current stellar mass (τ_{50}). We reproduce the τ_{90} versus τ_{50} plot from Figure 3 of Weisz et al. (2019) to compare the overall distribution of star formation histories of the modeled versus ob-

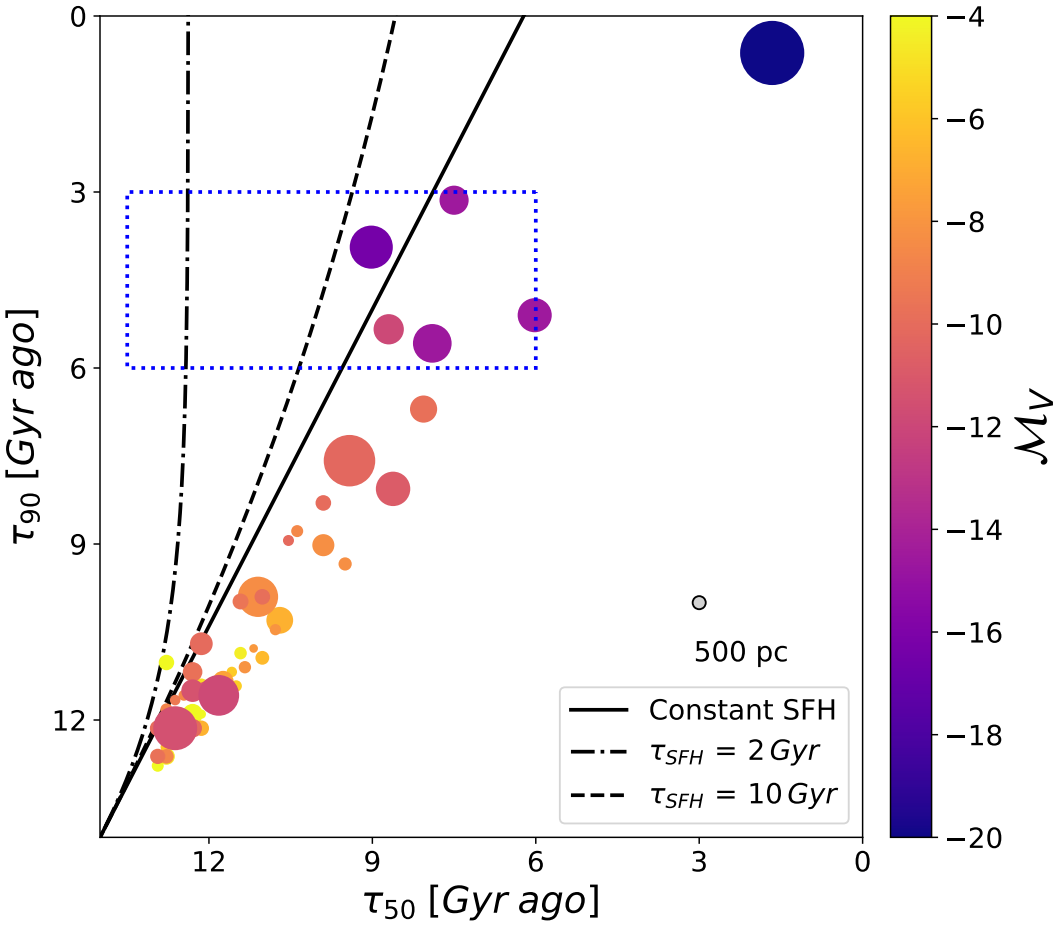

Figure 5.2: Look back time at which 90% of the stellar mass formed (τ_{90}) versus the look back time at which 50% of the stellar mass formed (τ_{50}). Each point is colored by its absolute V-band magnitude at $z = 0$ and sized relative to their half light radii in pc. The grey dot shows a point with half light radius of 500 pc. The solid line shows constant star formation history. The two dashed lines correspond to exponentially declining SFH (e.g. $SFH(t) = t_0 \cdot e^{-t/2\,Gyrs}$ and $SFH(t) = t_0 \cdot e^{-t/10\,Gyrs}$ respectively, where t_0 is a constant. Compare this plot to the Figure 3 in Weisz et al. (2019). Weisz et al. (2019) uses the rectangle shown in blue to show the region within which there are no Milky Way satellites, in contrast to the M31 system.

served dwarfs. Interestingly, we are unable to reproduce the lack of galaxies inside the blue dotted rectangle in Figure 5.2, which is a feature Weisz et al. (2019) identifies in the Milky Way dwarfs, however no such feature is seen for the M31 dwarfs, in agreement

with Figure 5.2.

Despite our overall good agreement, there are interesting distinctions between the modeled and observed $\tau_{90} - \tau_{50}$. Figure 5.2 shows that our τ_{90} values match well with quenching times for Milky Way satellites by Weisz et al. (2019). In Figure 5.3, we compare the τ_{90} distributions of Weisz et al. (2015) for the Milky Way, M31, and the Local Group as a whole using two-sample Kolmogorov–Smirnov (KS) test to determine if they come from the same distribution. A two-sample KS test on the observed distributions with models results in a $p = 0.28$ for the Milky Way, $p = 0.98$ for the Local Group, and $p = 0.66$ for M31 with $\alpha = 0.05$ respectively. Since all p–values are not less than α values the modeled distributions come from distributions of τ_{90} that are not very different. Yet, there may be disagreement between the modeled and observed star formation histories or inherent scatter in τ_{90} between halos. However a further exploration of this is beyond the scope of this work.

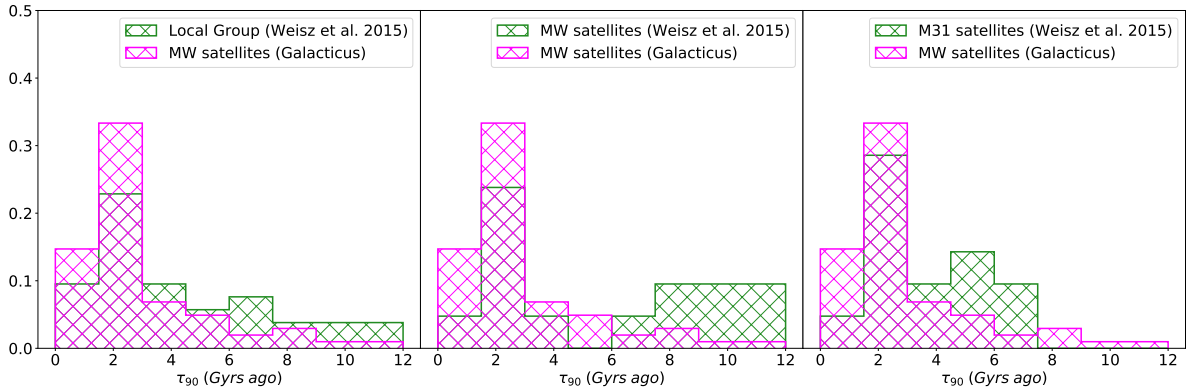

Figure 5.3: Normalized distribution of τ_{90} in Gyrs. Two curves show the predicted values from observations of Weisz et al. (2015) (green) and models (pink) respectively. Left panel: comparison of our model to the Local Group dwarfs. Middle panel: comparison of our model to Milky Way dwarfs. Right panel: comparison of our model to M31 dwarfs.

In contrast, we find a systematic delay of τ_{50} in our model of about 500 Myrs for the ultra-faint dwarfs. This delay may be due to the lack of molecular hydrogen cooling in our models, delaying the start of star formation until a halo has $v_{\rm vir} > v_{\rm cooling}$, with $v_{\rm cooling}$ chosen to approximate the atomic cooling threshold. While delaying star formation until after the atomic cooling limit does not create the same systematic effect for τ_{90}, it will take the halos longer to form 50% of their $z = 0$ stellar populations. We also find the most luminous satellites in our model to have $\tau_{50} < 2$ Gyrs. This is a peculiar case since most recent star formation in the Milky Way satellite system took place $3 - 6 \sim$ Gyrs based on Weisz et al. (2019).

5.3 Discussion & Conclusions

Well-studied Milky Way satellites are an ideal data set for constraining parameters of Galacticus to best model dwarf galaxies. The initial goal of this study was to build a viable model of the classical dwarfs in the Milky Way and explore predictions for their star formation histories with the standard implementation of Galacticus. However, in addition to successfully modeling the properties of the classical Milky Way satellites, we are also able to match the properties of the more luminous ultra-faint dwarfs. Reproducing the stellar properties of the Milky Way satellites, including the ultra-faint fossil galaxies, was unexpected due to the stochastic star formation processes that govern the evolution of the lowest mass galaxies (Guo et al. 2016). In addition to the properties at $z = 0$, we also reproduce the star formation histories and quenching times (τ_{90} vs τ_{50}) of the Local Group dwarfs.

Despite the success of GALACTICUS in modeling the dwarfs, the match between the $z = 0$ properties and star formation histories for the classical and brightest ultra-faints breaks down for the dwarfs below $M_{\rm V} \sim -6$). Dwarf galaxy halos modeled with GALACTICUS cool via atomic processes. As discussed in Section 3.1, we choose the minimum v_{vir} to approximate the atomic cooling cut off during reionization. The lowest mass dwarfs ($M < 10^8\ M_\odot$) initially cooled via the rotational and vibrational transitions of H_2 (Bromm et al. 2009). The lack of H_2 cooling in our model delays the start of star formation in all our dwarfs. Since the majority of stars in the more luminous dwarfs ($M_V > -8$) formed when their host halos were above the atomic cooling threshold, we are able to model their properties and star formation histories.

In contrast, as the luminosity, and halo mass (Santos-Santos et al. 2022), of the faintest dwarfs decreases, the fraction of the stars formed with $v_{vir} < v_{\rm cooling}$ increases. Since our model does not currently account for gas cooling via H_2, we are less able to reproduce the properties and star formation histories of the latter group. In addition, a subset of the faintest dwarfs never reach $v_{\rm vir} > v_{\rm cooling}$. As a result, they remain completely dark in our model, an effect seen by the turnover of the modeled luminosity function at $M_V > -4$. The question on whether star formation in halos with masses $< 10^8$ $\rm M_\odot$ at reionization (below the atomic cooling limit) is required to reproduce the observed properties of Ultra Faint Dwarfs (UFDs) is still an open question. A robust test of what is the minimum halo mass hosting luminous galaxies has been proposed in (Kang and Ricotti 2019, Ricotti et al. 2022) and relies on detecting ("ghostly") stellar halos in isolated dwarf galaxies in the Local Group (*e.g.,* Leo A, WLM, IC 1613, NGC 6822). The first results using this new method seem to indicate that halos with masses as low as

10^7 $M_\odot$ at $z \sim 7$ should be luminous. This is also in agreement with results from Dark Energy Survey (DES) (Nadler et al. 2020) using halo-matching (Behroozi et al. 2019). The inclusion of models of H_2 into GALACTICUS, and how it effects our modeling of the faintest dwarfs, will be a subject of parallel work.

Our conclusions are as follows.

- We reproduce star formation histories that are consistent with observations (Weisz et al. 2014; 2019). As with the additional $z = 0$ dwarf properties, this is done without any additional tuning of the baryonic physics.

- We find the quenching timescales (τ_{50} and τ_{90}) of our modeled dwarfs are in reasonable agreement with those for the M31 dwarfs.

This chapter shows that the same astrophysical prescriptions and parameters that reproduce $z = 0$ properties of the Milky Way dwarfs can reproduce their star formation histories as well.

Chapter 6

Modeling The Cen A Satellites

Previous Chapters 3,4,5 showed that Galacticus can reproduce the properties and SFHs of the Milky Way satellites. In this chapter, we present the modeling of dwarf galaxies of Cen A using the constrained astrophysical prescriptions and parameters of the Milky Way dwarfs discussed in Table 3.2.3, Chapter 3. Large components of this chapter are drawn verbatim from Weerasooriya et al. (in prep. a).

We run Galacticus (Benson 2012) on the N-body and EPS merger trees of Cen A analogs with the same star formation physics that reproduces the properties of observed dwarfs of the Milky Way down to ultra-faint dwarfs (Weerasooriya et al. 2023). This work aims to test whether our model can reproduce the observed cumulative luminosity function and the luminosity metallicity relation of Cen A dwarf satellites and make predictions of other properties and SFHs of Cen A satellites. This will allow us to investigate the effects of the host environment on dwarf galaxies.

6.1 Observational Sample

The observations for properties of dwarf galaxies of the Milky Way are well explored through many surveys and studies (Aguado et al. 2019, Albareti et al. 2017, Drlica-Wagner et al. 2020). However, as it is more distant, Cen A has fewer observations, scattered across different surveys and databases. In this section, we describe a sample of observational data of Cen A taken from the literature that we will compare to our models. We use observational data for Cen A satellites from a variety of sources Crnojević et al. (2010; 2014), Crnojevic et al. (2016), Crnojević et al. (2019), Karachentsev et al. (2013), Müller et al. (2015; 2017; 2019), Taylor et al. (2016; 2018). A compilation of observations from a variety of sources used in this study, along with their references, can be found in Appendix A. In addition to the dwarfs in the above sample, we also include 38 new dwarf galaxy candidates from Taylor et al. (2023, in prep.) in our overall analysis, but on do not list their properties in Appendix A. This sample only includes dwarfs with distance or velocity measurements that verify them as members of Cen A with distances $\leq 5.8\,Mpc$ (Appendix A).

The current sample of observations of Cen A is incomplete due to three major reasons: 1.) The lack of systematic surveys of Cen A and spatial incompleteness of current surveys. For example the PISCeS survey is spatially incomplete, and biased toward coverage of the Northeastern region of Cen A's halo. These non-uniformities in design or analysis make completeness calculations more complex. 2.) The detectability limits of different surveys, e.g. SCABS is limited to $M_V < -7.2$ within 150 kpc covering an area

of 50 square degrees and a surface brightness limit of 27.8 mag arcsec^{-2} in the g-band (Taylor et al. 2016; 2017; 2018), while PISCeS can detect dwarfs down to $M_V < -8$ within 150 kpc and a surface brightness limit of 28.5 mag arcsec^{-2} in the g-band (Crnojević et al. 2014; 2019). Detectability also limits the number of fainter dwarfs observed by current surveys. 3.) The lack of distance measurements in the outskirts (Müller et al. 2017, Taylor et al. 2018) also hinder determination of membership. Distances are essential to determine the membership of satellites, their shapes and brightness. Thus lack of distances can cause the data to have higher errors in their sizes and magnitude measurements. Note that while the virial radius of Cen A is $\sim$ 409 kpc, most of these satellites are beyond that limit, yet within Cen A's 'splashback radius'= 1.1 Mpc (Diemer and Kravtsov 2014). The splashback radius is a physically motivated halo boundary that eliminates spurious evolution of radius and mass caused by standard definitions of virial radius (Diemer and Kravtsov 2014).

The observational properties of known Cen A satellites are still largely unknown. Thus, our knowledge of these galaxies and their properties is nowhere near as extensive as of the Milky Way system. Quantitative estimates of incompleteness of Cen A dwarfs have not been made by previous studies, and such exploration is beyond the scope of our current work. A preliminary quantitative exploration of the completeness limits in SCABS limits Cen A satellites is currently underway by Leahy et al. (private communication). Their exploration of completeness using 5000 Monte Carlo dwarf galaxy realizations reveals a completeness of 96% for dwarf galaxies of $\lesssim 18\,mag$ in the g-band. They report 50% completeness at g-band magnitudes of 20.01 and 50% completeness at

surface brightness of $\sim 27.8\,\mathrm{mag\,arcsec^{-2}}$. In Figure 6.1, we compare our models within 150 kpc to the number of galaxies expected to be observed by this completeness test by Leahy et al. (private communication) for the SCABS data. Based on the comparison, our galaxy models agree with the observed luminosity function for dwarfs fainter than 16 mag ($M_g = -10$) and overproduces the brighter dwarfs.

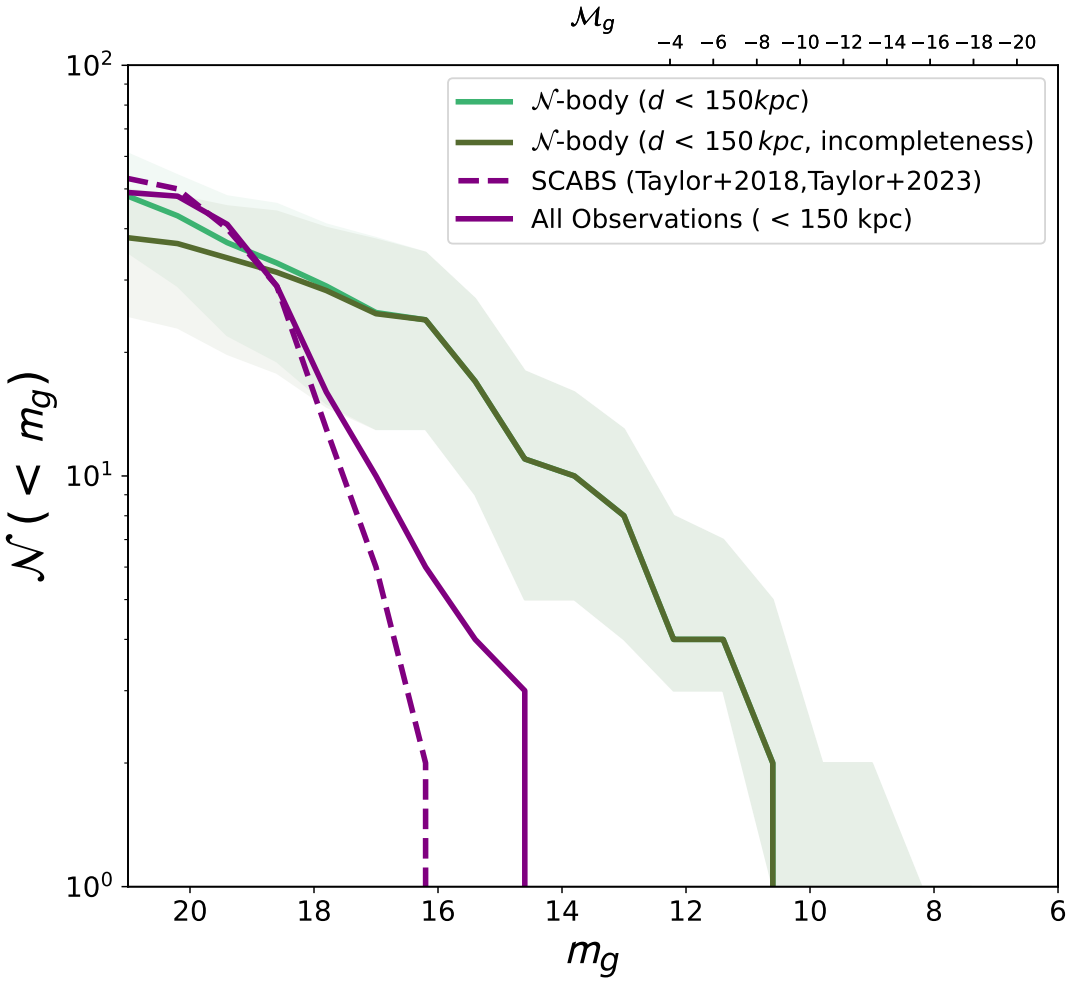

Figure 6.1: The number of galaxies per apparent magnitude in the g_{DES} filter. The seagreen curve shows our N-body galaxy models within 150 kpc, the olive green curve shows the number of satellite galaxies expected to be observed based on completeness tests run by Leahy et al. (private communication) for SCABS, and the purple dashed curve shows SCABS dwarfs (Taylor et al. 2018, Taylor et al.), and the solid line shows the observed luminosity function within 150 kpc.

6.2 Semi-Analytic Model

Despite the influx of observational data, high-resolution hydrodynamic simulations of a Cen A analog have not yet been run to $z = 0$, and are on the edge of current computational capabilities. Note that previous studies we discussed in the introduction 1.2.2 use a variety of methods to determine the mass of Cen A, while in this work we defined the virial mass of a halo in terms of the spherical overdensity given by Bryan and Norman (1998). Thus other studies are not necessarily consistent with methods used in our models. Due to significant uncertainties in the observational mass estimates of Cen A, we do not perform any conversion to our preferred mass definition. Instead we investigate a wide range of possible halo masses for Cen A.

Following the same method in Chapter 3, we model the baryonic properties of the Cen A system using the Semi-Analytic Model (SAM) Galacticus (Benson 2012). We apply the same astrophysical prescriptions and parameters that reproduced the Milky Way satellites. These include a reionization redshift of 9, filtering velocity of $25\,km\,s^{-1}$, a cooling velocity of $19\,km\,s^{-1}$. Please refer to Chapter 3 for further details. Of these parameters, quenching from ram pressure stripping, and tidal stripping, primarily effects determines how dwarf satellites are affected by a host environment. For example ram pressure stripping can strip gas out of galaxies resulting in a shortage of gas supply and eventually quench star formation. However, we would like to remind the reader that the effect of ram pressure stripping efficiency was negligible for the Milky Way satellites (Weerasooriya et al. 2023). Regardless, we implement a ram pressure with the same high

efficiency as in Weerasooriya et al. (2023).

While a few studies have explored the star formation histories of Cen A dwarfs (Côté et al. 2009, Crnojević et al. 2011), these SFHs remain largely unknown. Given the lack of known star formation histories and Cen A dwarf physics, we assume the astrophysics governing the star formation histories of the Cen A dwarfs is the same as for the Milky Way satellites. We apply the astrophysical prescriptions and parameters which reproduce the star formation physics and star formation histories of the Milky Way satellites (Weerasooriya et al. 2023) to the N-body merger trees and EPS merger trees of Cen A analogs. However, the models run with merger trees from the N-body simulation probe only one possible mass of Cen A. Therefore, we run several EPS trees with different mass Cen A analogs spanning the full range of possible Cen A halo masses. While the EPS trees allow us to efficiently probe a range of M_{vir} for the Cen A halo, they do not provide positional information on the satellites. As such, EPS trees do not allow us to look at the dependence of satellite populations on their distance from the host.

6.3 Results

In this section, we compare different properties of the modeled Cen A dwarfs with observational data described in Section 6.3.0.1. We start by exploring the properties of the Cen A dwarfs including the luminosities, half-light radii, and velocity dispersions.

6.3.0.1 Cumulative Luminosity Function at $z = 0$

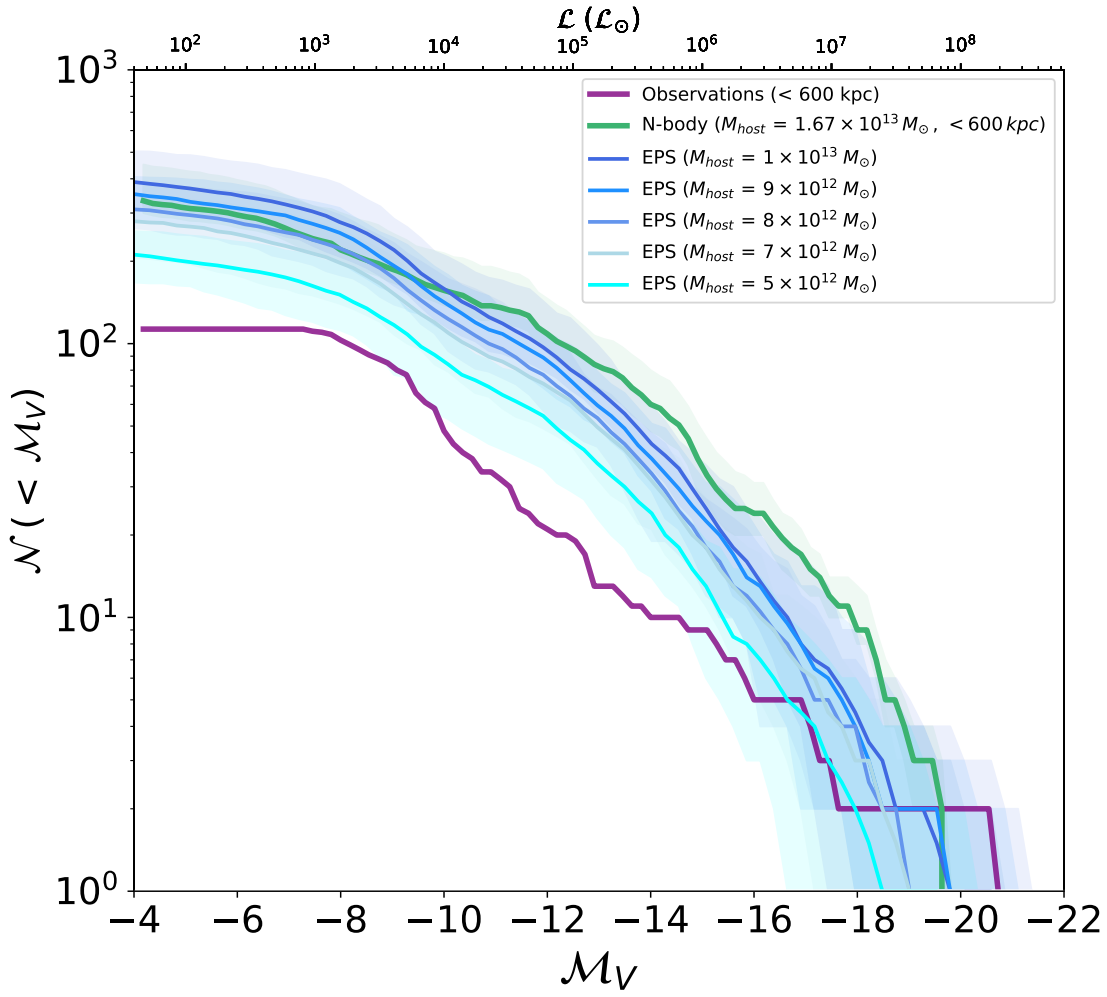

Figure 6.2: Luminosity functions for the Cen A satellites within $r_{vir} = 600\,\text{kpc}$ for models and observations. Purple plot shows the observational sample within 600 kpc projected radius. The predicted luminosity functions for Cen A satellites within 600 kpc and $M_V \leq -4$ in the y-z plane are shown in green (N-body). Plots shown in shades of blue represent EPS trees with different Cen A masses. Each blue line shows the median per M_V bin for 30 different EPS trees, and a shaded region of minimum and maximum.

In Figure 6.2, we plot the cumulative luminosity function of Cen A satellites for observations within $r_{vir} = 600\,\text{kpc}$ of the projected radius and for dwarfs modeled with Galacticus out to 600 kpc in the y-z plane. For the purpose of comparison of Centau-

rus A dwarfs, we analyze satellites viewed "in projection". This is because observations are viewed from a 2-D plane. We show models using two types of merger trees, N-body and EPS. We remind the reader that this selection can be done only when using N-body trees since positional information is available. Since we do not know the viewing angle of our modeled Cen A, we rotate the line of sight relative to the $\hat{x}$ direction of the simulation in 5-degree steps (note that the step size and direction of rotation chosen here is arbitrary). This essentially accounts for uncertainty in the luminosity function. The median luminosity function over all potential viewing angles is shown in green, while the maximum and minimum number of luminous galaxies per bin in M_V is shown by the shaded envelope.

We also run models using merger trees generated by Extended Press Schechter (EPS) to explain the mass range of Centaurus A's halo. EPS models for different mass merger trees are shown in shades of blue. These models inherently do not have positional information. We run EPS models for $5 - 9 \times 10^{12}\,\mathrm{M}_\odot$ and $1 \times 10^{13}\,\mathrm{M}_\odot$ halos with 30 merger trees for each halo mass. The solid curve shows the median per M_V bin with shaded areas indicating the minimum and maximum over 30 EPS trees. All of these models follow the general shape of the luminosity function for observations within 600 kpc. However, note that there is some variation in the shape of the luminosity functions between N-body and EPS merger trees.

While we cannot constrain the mass of Cen A from the models due to poorly understood completeness in the observations for fainter dwarfs, comparison with models at the

bright end of the luminosity function suggests that Cen A is likely to have a higher mass because the Cen A analogs with higher mass match with the observed luminosity function better. We find our models overproduce the number of dwarfs at all luminosities. However, the observed luminosity function within 600 kpc is still likely to be incomplete. However, our modeled dwarfs reproduce the overall shape of the observed cumulative luminosity function for N-body merger trees and EPS trees traced at all modeled host masses. Note that any such inference on the mass of Centaurus A halo from this approach is subject to the caveat that Galacticus predictions could be inaccurate.

Poorly understood completeness limits of the observations within 600 kpc of Cen A make exploration of these satellites and their properties limited. However, the observational sample is relatively complete within 200 kpc (Müller et al. 2019) down to $M_V = -10$. SCABS and PISCeS surveys cover a spatial region within a projected radius of 150 kpc down to dwarfs as faint as $M_V < -7.2$ (Taylor et al. 2016) and $M_V < -8$ Crnojević et al. (2014). We can assume completeness within 200 kpc down to $M_V \sim -10.0$ (see section 6.3.0.1 for a detailed completeness discussion). We plot the luminosity function within 150 kpc, which has a fairly complete sample of satellites from SCABS, PISCeS and other observations and match the number of luminous satellites within 150 kpc. However, our models do not match the steep slope of the observed luminosity function (Figure 6.3). Specifically, there is a dearth of observed luminous satellites with $M_V < -13$ mag steepening the brighter end of the luminosity function. This is consistent with other studies of the inner 200 kpc of the Cen A halo (Müller et al. 2019). The full implications of this result will be explored in Chapter 7.

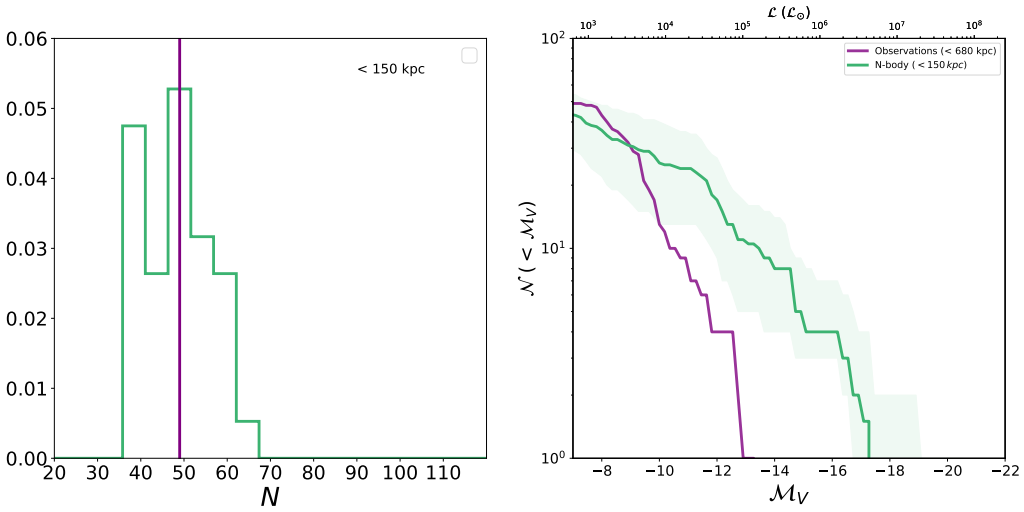

Figure 6.3: Left panel: Number of luminous satellites around Cen A brighter than $M_V \leq -6$ predicted within 150 kpc for different lines of sight as y-z plane is rotated (shown in green). Purple line shows the total number of satellites in the observed sample. Right panel: cumulative luminosity functions for the Cen A satellites within 150 kpc in the y-z plane are shown in green. We plot the median of the cumulative luminosity in green and shade within our uncertainty budget.

6.3.1 Properties of The Cen A Dwarf Galaxies at $z = 0$

Now that we have compared the luminosity function for Cen A satellites within 600 kpc of Cen A for both models and observations, let us explore other properties of these satellites at $z = 0$.

6.3.1.1 Half Light Radii

In Figure 6.4, we show the luminosity and half-light radii for the observed Cen A dwarfs and dwarfs modeled with EPS merger trees with $\sim 1 \times 10^{13}\,\mathrm{M}_\odot$. We compare our results with available Cen A dwarfs (Taylor et al., Crnojevic et al. 2016, Crnojević et al. 2019) and Milky Way dwarfs, M31 dwarfs (McConnachie 2012). Majority of observations beyond the Local Group do not go below 0.01 $\mathrm{L}_\odot\,\mathrm{pc}^{-2}$. We calculate the half light

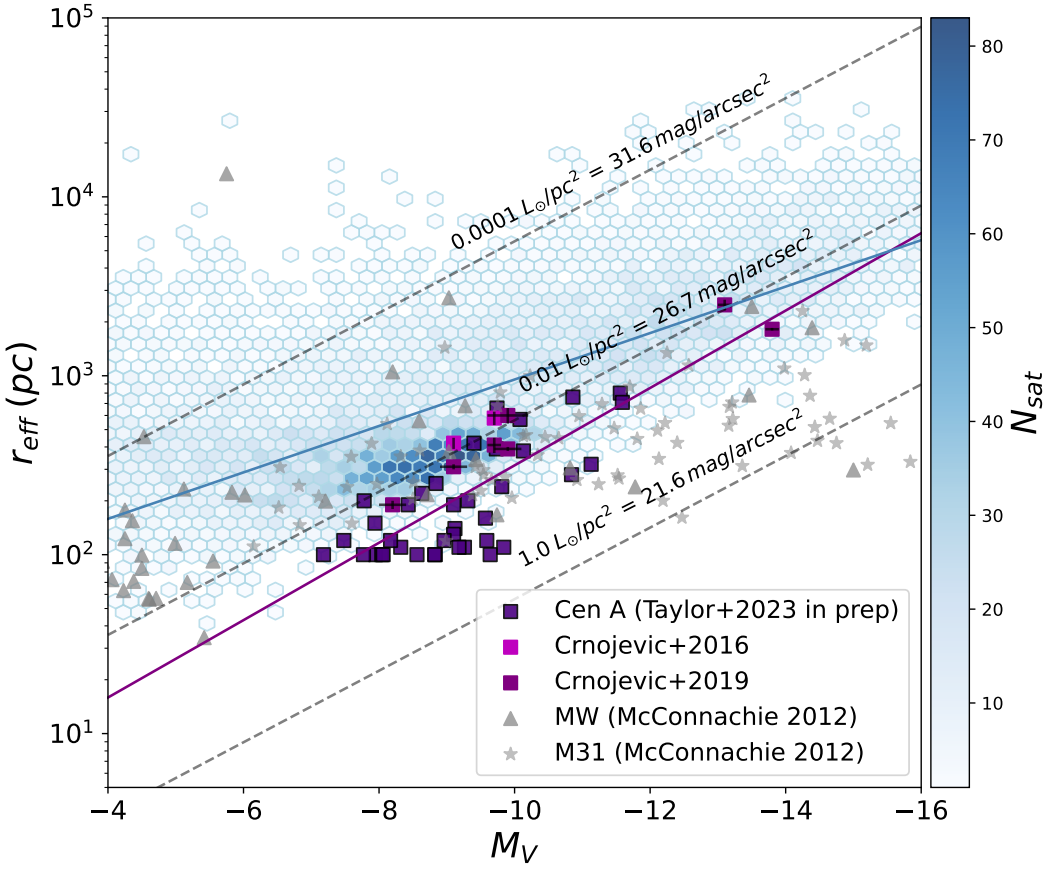

Figure 6.4: Half flight radii vs the absolute g_{DES} band magnitude of the Cen A satellites (green). We show the observed half light radii of Cen A dwarfs from Taylor et al. in prep (g' band), and Crnojevic et al. (2016), Crnojević et al. (2019) (V band). Peak wavelengths in DES g' and V bands are $\sim 550\,nm$ and $\sim 551\,nm$ respectively. Given the small differences in peak wavelengths among g' and V bands, we plot data available in respective bands. The observations of McConnachie (2012) for the Milky Way (V band) and M31 (V band) are also shown in blue stars and grey circles. Iso-surface brightness lines are shown in grey dashed lines. Linear regression lines for observations and our model is shown in purple and blue respectively. These results are consistent with models that we predicted for the Milky Way satellites (Weerasooriya et al. 2023).

radii of the modeled Cen A satellite galaxy in the g_{DES} band. We use DES filters since SCABS data are calibrated to the SDSS photometric system (Taylor et al.). We quantify the observations and our model using two regression lines in purple (slope = 0.22) and blue (slope = 0.15) respectively. We find a root mean square error of 0.19 in log scale.

At high luminosities, the modeled sizes of the dwarfs agree with observations of the Cen A dwarfs. However, modeled sizes for the fainter dwarfs are higher than that of the observed values. This is consistent with the systematically larger sizes of the fainter modeled dwarfs compared to observations of the Milky Way satellites (see Figure 6.4). Galacticus tends to overpredict the half-light radii with merger trees generated from EPS and N-body simulations. This likely results from limitations in the dynamic range of EPS merger trees (Somerville and Kolatt 1999, Zhang et al. 2008). Consequently, limitations in mass would result in limitations in the size of halos and their respective half-light radii. N-body trees can also overestimate half-light radii if a halo has $N < 1000$ particles (Weerasooriya et al. 2023). A study of how the resolution affects the size of the modeled dwarfs will be a subject of future study.

6.3.1.2 Metallicity

The current observed metallicities of the Cen A dwarfs are limited. In Figure 6.5 we have shown the observations of iron abundance for Cen A satellites from Crnojević et al. (2010; 2019), Müller et al. (2019). We show two linear regression lines for the observations (purple) and 30 EPS tree models (blue) with slopes 0.13 and 0.04 respectively. We find a good root mean square error of 0.27 between the two lines. Note that hexagonal bins with more satellites follow the observed linear regression line. Notice that Müller et al. (2019) finds a metallicity floor between -8 and -10. However, their error bars are $\sim 0.5\,dex$. Thus, these values are still consistent with our modeled values. While spectroscopic measurements of metallicities by Müller et al. (2021) agree well with Milky Way

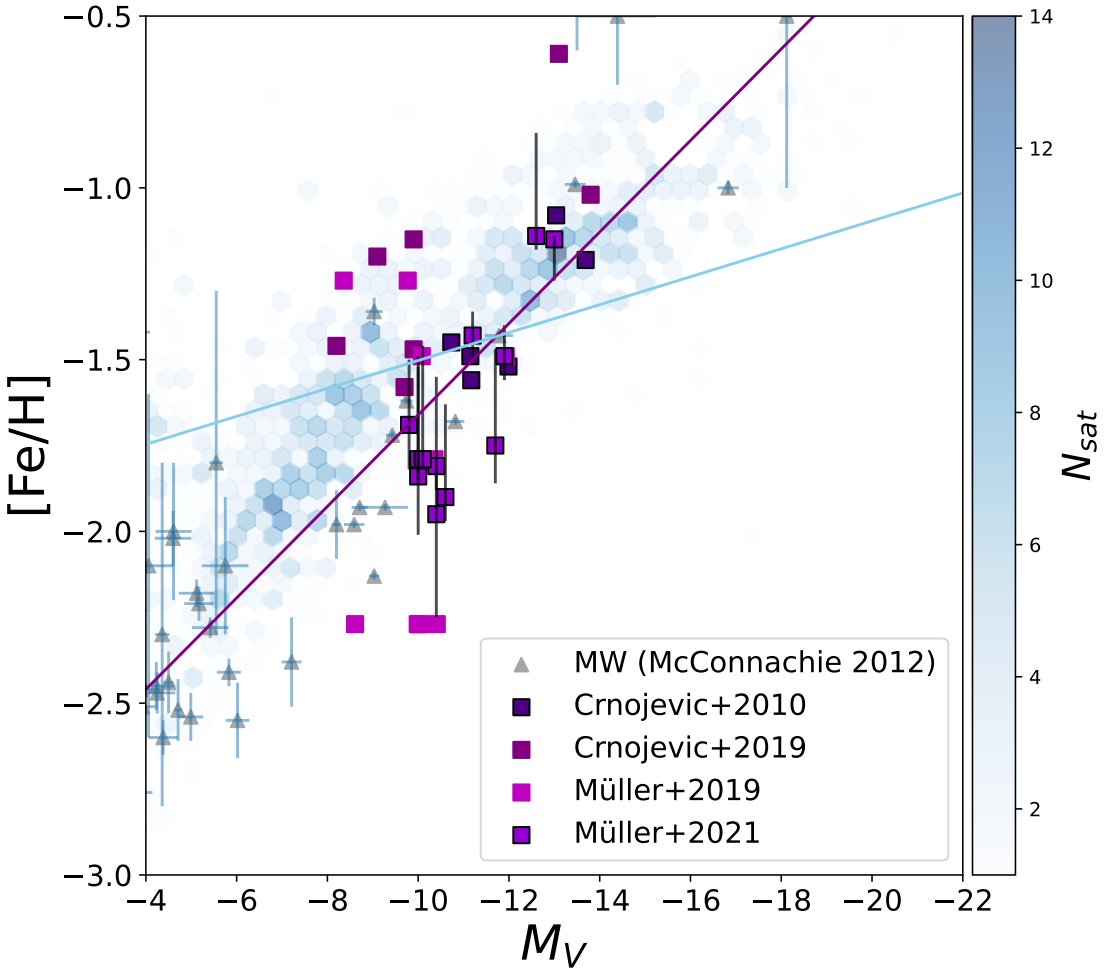

Figure 6.5: Luminosity–metallicity relation for the Cen A satellites. The observed values are shown by non-circle markers Crnojević et al. (2010; 2019), Müller et al. (2019; 2021). Metallicities of the Milky Way satellites are shown as grey triangles (McConnachie 2012). Predicted abundances for satellites from $10^{13}\,\mathrm{M}_\odot$ EPS merger tree are shown in blue. Each hexagonal bin may contain a number of satellites from 0 (light blues) to 14 (dark blues).

dwarfs, their photometric measurements are reported to have a larger scatter. The authors state that the scatter might be due to the age-metallicity degeneracy and incorrect assumptions of uniform old ($\sim 10\,\mathrm{Gyr}$) populations.

Using the same astrophysical prescriptions and parameters as those that reproduced

the luminosity-metallicity relations of the Milky Way dwarfs, we present the modeled metallicities of the Cen A dwarfs in the $1 \times 10^{13}\,M_{\odot}$ EPS tree. The metallicities of the modeled dwarfs in this work agree well with currently available observations of Cen A satellites (Crnojević et al. 2010; 2019, Müller et al. 2019). This could potentially mean that the Cen A satellites have a similar enrichment history to that of the Milky Way's satellites. This could also imply that dwarf metallicities are independent of their local environment. Based on our models, we expect 38 new fainter dwarfs of SCABS (Taylor et al. 2023, in prep) to have a metallicity of -2.0 dex at $M_V \sim -7\ mag$.

6.3.1.3 Velocity Dispersions

Velocity dispersion of satellite galaxies probes the dark matter mass of the host Wake et al. (2012), Bogdán and Goulding (2015), Schechter (2015), and consequently its gravitational potential. However, velocity dispersions of Cen A satellites are unknown except for KK197. As such, additional data is required to comment on the velocity dispersions of the Cen A dwarfs population as a whole.

In Figure 6.6, we show the velocity dispersion of KK197 (Müller et al. 2021), and those of the Milky Way satellites (McConnachie 2012). We calculate the velocity dispersion of the modeled dwarfs (σ_{sat}) at stellar half-mass radii for the modeled dwarfs. While no theoretical studies have looked at the velocity dispersions of the Cen A dwarfs, most of our modeled sample fall within the observed velocity dispersions of the Milky Way satellites (McConnachie 2012). Note that the scatter increase for dwarfs $M_V > -10$. This might be due to the stochastic nature of star formation histories in the low mass

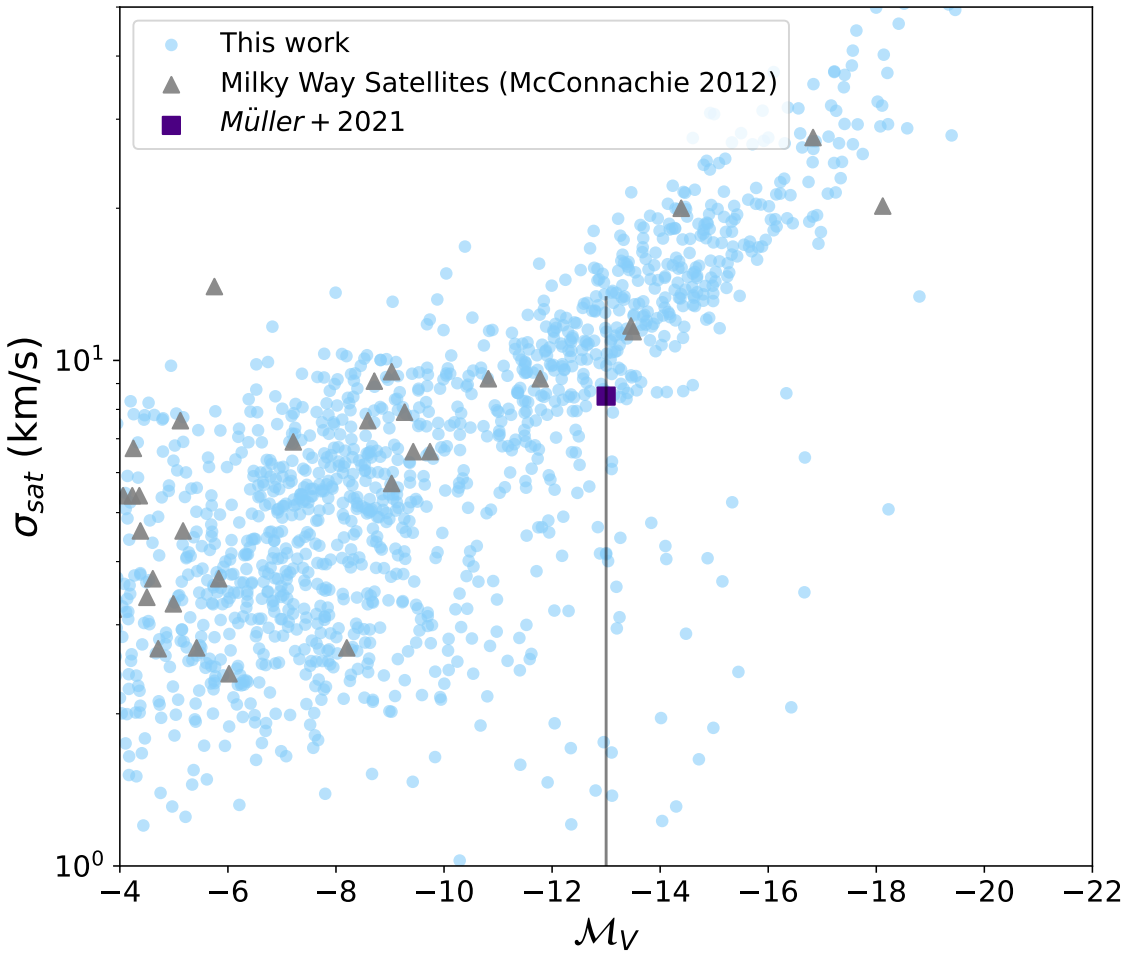

Figure 6.6: Predicted σ_{sat} of Cen A satellites (blue hexagons). These σ_{sat} are calculated at radii enclosing half of the stellar mass of each satellite galaxy. Grey triangles show the observed velocity dispersion of the Milky Way satellites (McConnachie 2012). Note that the predicted values of Cen A satellites are consistent with the velocity dispersion of the observed Milky Way satellites.

dwarfs, and uncertainties coming from half light radii. Given that velocity dispersion probes dark matter halo mass and evolution of these galaxies, it might be possible that Cen A dwarf galaxies evolved in a way that was similar to that of the Milky Way dwarf satellites.

6.3.2 Predicted SFHs of The Cen A Dwarfs

Next we explore the modeled star formation histories of dwarfs for our modeled dwarfs. We remind the reader that due to dearth of SFHs for the known Cen A satellites, we have used the star formation physics of Weerasooriya et al. (2023). Given our success reproducing the star formation history of the Milky Way satellites in Weerasooriya et al. (2023), overall shape of the luminosity function, and properties at $z = 0$ of Cen A satellites, we consider it worthwhile to present SFHs for the Cen A dwarfs.

Unlike the Milky Way satellites, extensive observational studies on star formation histories of Cen A satellites are not available, except for KK197, ESO-269066, ESO-381018 (Makarova et al. 2007) and five dwarf irregulars KK182 (Cen6), ESO269-58, KK196 (AM1318-444), HIPASS J1348-37, ESO384-16 (Crnojević et al. 2012). Both KK197 and ESO-269066 are dwarf spheroidals, while ESO-269066 is a dwarf irregular. Dwarf spheroidals typically have old Red Giant Branch (RGB) stellar populations while dwarf irregulars are metal-poor and have little ongoing star formation. Crnojević et al. (2012) states KK197 and ESO-269066 have unusual RGB color scatter, which shows active star formation with high metallicity, while ESO-381018 is a typical dwarf irregular. Two of the dwarf irregulars KK196 and ESO269-58 studied are within $600\,kpc$ (see Figure 6 of Crnojević et al. (2012)). Positioned in the middle of Cen A's southern radio lobe, KK196 has a SFR of $0.0046 \pm 0.0004\,\mathrm{M}_{\odot}\,yr^{-1}$ and formed more than $60\%^{+20\%}_{-30\%}$ of stars 5 Gyrs ago (Crnojević et al. 2012).

Meanwhile, ESO269-58 located $300 \pm 50\,\mathrm{kpc}$ has few blue-loop, red supergiants and

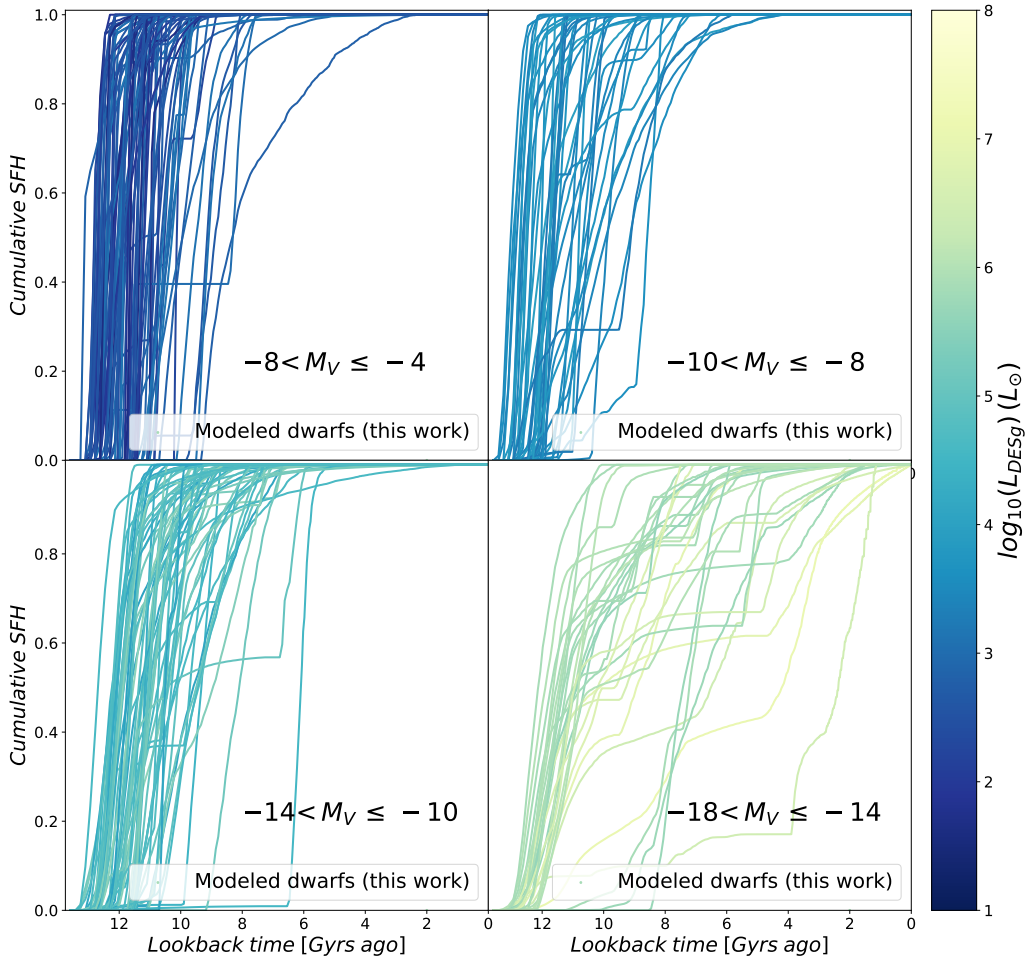

Figure 6.7: Cumulative star formation histories of the Cen A satellites (within 600 kpc) as a function of look back time colored by their luminosity in the DES g-band. The star formation histories are divided into four panels $-8 < M_V \leq -4$, $-10 < M_V \leq -8$, $-14 < M_V \leq -10$, and $-18 < M_V \leq -14$. Each line is colored by the galaxy's absolute V band magnitude at $z = 0$ (faintest in blue and brightest in yellow). The majority of the faintest dwarfs quench very early on. Most luminous galaxies are quenched later (6 Gyrs ago or later). Note that the galaxies on the upper left panel have not been observed yet. However, we predict their SFHs given observations, will reach those magnitudes in the era of Roman.

very broad red giant branch stars, and dense asymptotic giant branch zone. This dwarf has a higher SFR compared to KK196 with $0.07 \pm 0.04\,\mathrm{M}_\odot\,yr^{-1}$, and has formed $50\%^{+15\%}_{-15\%}$

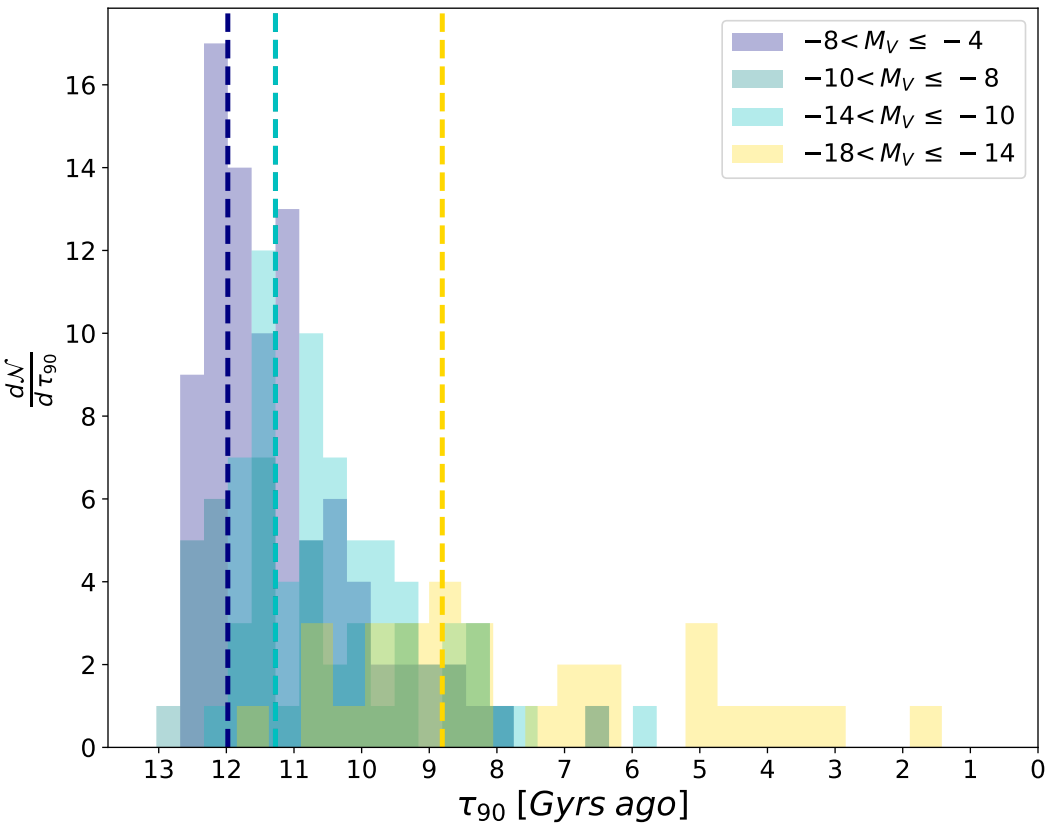

Figure 6.8: The distributions of τ_{90} (time taken for a particular galaxy to reach 90% of its stellar mass at $z = 0$) for the panels shown in Figure6.7. The faintest satellites quenched 12 Gyrs ago, while satellites between $-14 \leq M_V \leq -8$ quenched after 11.2 Gyrs ago. The most luminous galaxies quench much later ~ 8.8 Gyrs ago.

of stars 5 Gyrs ago. While its star formation activity has been enhanced between 3-5 Gyrs ago, Crnojević et al. (2012) also states that Cen A has lowered its star formation rate in the last 1 Gyr.

In Figure 6.7, we show the modeled cumulative star formation histories of the Cen A satellites as a function of look back time colored by their absolute V band magnitude at $z = 0$ for our N-body model. As expected, our Cen A modeled SFHs are similar to that of

the Milky Way satellites in Chapter 5 given our assumptions of astrophysical prescriptions and parameters. In the upper left panel, we show dwarfs with $-8 < M_V \leq -4$. These are the faintest galaxies. Most ultra faint dwarfs quench after $8 - 12$ Gyrs ago as expected since the faintest observed Milky Way satellites are the fossils of the first galaxies (Bovill and Ricotti 2011, Brown et al. 2012a). Upper right panel shows the satellites in the range $-10 < M_V \leq -8$. Majority of these satellites reached 90% of their present stellar mass 12 Gyrs ago. Most dwarfs in the upper right ($-10 < M_V \leq -8$) and lower left panel ($-14 < M_V \leq -10$) reached 90% of their present day stellar mass ~ 11.2 Gyrs ago. Known SFHs from observations of Cen A dwarfs discussed earlier would fall in the lower left panel of Figure 6.7. Most of the brightest galaxies in the lower right panel ($-18 < M_V \leq -14$) acquired 90% of their stellar mass 8.8 Gyrs ago.

6.4 Discussion & Summary

We model these dwarf galaxies using Galacticus. We have explored properties such as the cumulative luminosity function, luminosity-metallicity, and half-light radii from observations of the Cen A system. We also predict their velocity dispersions, star formation histories, etc. We summarize the results of this chapter as follows,

- The same astrophysical prescriptions and parameters allows Galacticus to reproduce the Milky Way dwarfs for the global properties of the Cen A satellites. However, in the inner 200 kpc of the galaxy the picture is more complex. While being cognizant of the lack of observations in the Cen A system, we conclude that overall properties and trends of the Cen A satellite population are similar to the

dwarf galaxies around the Milky Way.

- Our N-body models within 600 kpc and EPS 10^{13} $M_{\odot}$ of Cen A reproduce luminosity functions that follow the overall shape of observations. However, we do observe a slight variation in the luminosity functions between the N-body and EPS merger trees.

- Cen A satellites follow a similar metal enrichment and stellar feedback to the Milky Way satellites. That is we obtain similar luminosity-metallicity relations for both the Milky Way and Cen A as expected. This could mean metallicity might not depend on environment.

- Assuming similar star formation physics of the Milky Way satellites for Cen A, SFHs, and quenching times of the Cen A satellites also follow similar trend to the Milky Way satellites.

In this chapter we have shown that the same astrophysical prescriptions and parameters that reproduced the properties of the Milky Way satellites, can reproduce the overall shape of the luminosity function of Cen A dwarfs. We will discuss the inner dwarfs of Cen A and their implications for environmental quenching in the next chapter.

Chapter 7

The Curious Case of Centaurus A

In this chapter, we further explore the curious case of the dwarf galaxies within 200 kpc of Cen A. Weerasooriya et al. (b.) will draw from this work.

As seen in Chapter 6, comparisons between theoretical models and Cen A observations reproduce the correct number of dwarfs and the shape of the luminosity function within 600 kpc. However, simulations cannot reproduce the steep Cen A luminosity function within 200 kpc (see Chapter 6). In this region, our modeled luminosity function over-predicts the number of brighter ($M_V < -13\,mag$) satellites. While there aren't many studies on the effects of the host environment on Cen A dwarfs, Crnojević et al. (2012) finds dwarfs have lower SFR in the denser inner region of Cen A. Crnojević et al. (2012) concludes that the environment does play a role in star formation in dwarfs. They find the dwarf irregulars closest to Cen A have lower SFR within the last 1 Gyr. They also find that the fraction of gas mass to stellar mass and gas mass to average SFR is much lower in these dwarfs.

We use the merger trees from the N-body simulation of Cen A described in Chapter 2. The positional information from N-body merger trees allows us to study the dwarf galaxies closest to the host (within 150 kpc and < 600 kpc). In this chapter, we explore what combination of the astrophysical prescriptions and parameters can reproduce this steepening effect in the luminosity function within 150 kpc. In order to inspect this feature in detail, we look at how the luminosity function depends on distance from Cen A in more detail.

First, we plot luminosity functions within distances from $150-500$ kpc (Figure 7.1) for our modeled dwarfs and known observed dwarfs of Cen A. Distance explored are within 500 kpc, 400 kpc, 300 kpc, 250 kpc, 200 kpc, 150 kpc in shades of purple (shade lightens as the distance decreases) for observations and N-body models in shades of green (the smallest distance is in olive and largest distance in light green). Normalization of the density of galaxies observed per absolute V band magnitude decrease as the distance explored decreases for both models (green) and observations (purple). This is expected because when the area explored decreases, the number of luminous satellites decreases for all distances. While the number of faintest dwarfs within 500 kpc for our model is greater than 100, the observed number density of dwarfs is ~ 100. This is likely due to incompleteness in observations. All distances above 250 kpc produce luminosity functions that follow the correct shape of the observed luminosity function.

We find the observed luminosity function abruptly steepens 200 kpc $\sim< d \sim<$ 250 kpc while no corresponding trend is seen in the modeled luminosity function. However, for

dwarfs within 150 kpc, the observed number of dwarfs agrees with the models in the faint end. The former is not expected because galaxies this massive typically have brighter galaxies unless there exist some quenching effects at play within this region of Cen A. We note that our results are consistent with Müller et al. (2019). But their models are still within 90% of the observations, and so agree with observations.

In order to investigate the lack of luminous satellites within 200 kpc of Cen A, we test a variety of potential feedback mechanisms, however, it is likely that the lack of brighter dwarfs is caused by a quenching effect. In this work, we determine if it may have been caused by reionization redshift, reionization velocity, or tidal stripping effects.

7.1 Effect of Reionization Redshift

We start by determining the effect on the dwarf population if the Cen A reionized at a different redshift than the Milky Way. Cen A is 10 times more massive than the Milky Way and thus originated from larger overdensities than the Milky Way. Larger overdensities evolve more rapidly, and thus reionize earlier. Therefore, Cen A likely reionized earlier than the Milky Way.

Our fiducial model assumes the reionization of the Milky Way to be $z_{\rm reion} = 9$ (Gnedin 2000, Bullock et al. 2000, Alvarez et al. 2009, Busha et al. 2010, Iliev et al. 2011, Spitler et al. 2012, Ocvirk et al. 2013, Li et al. 2014, Aubert et al. 2018). The goal is to test whether Cen A might have reionized sometime earlier than $z = 9$, since it is more massive than the Milky Way and the reionization process could have occurred anywhere between

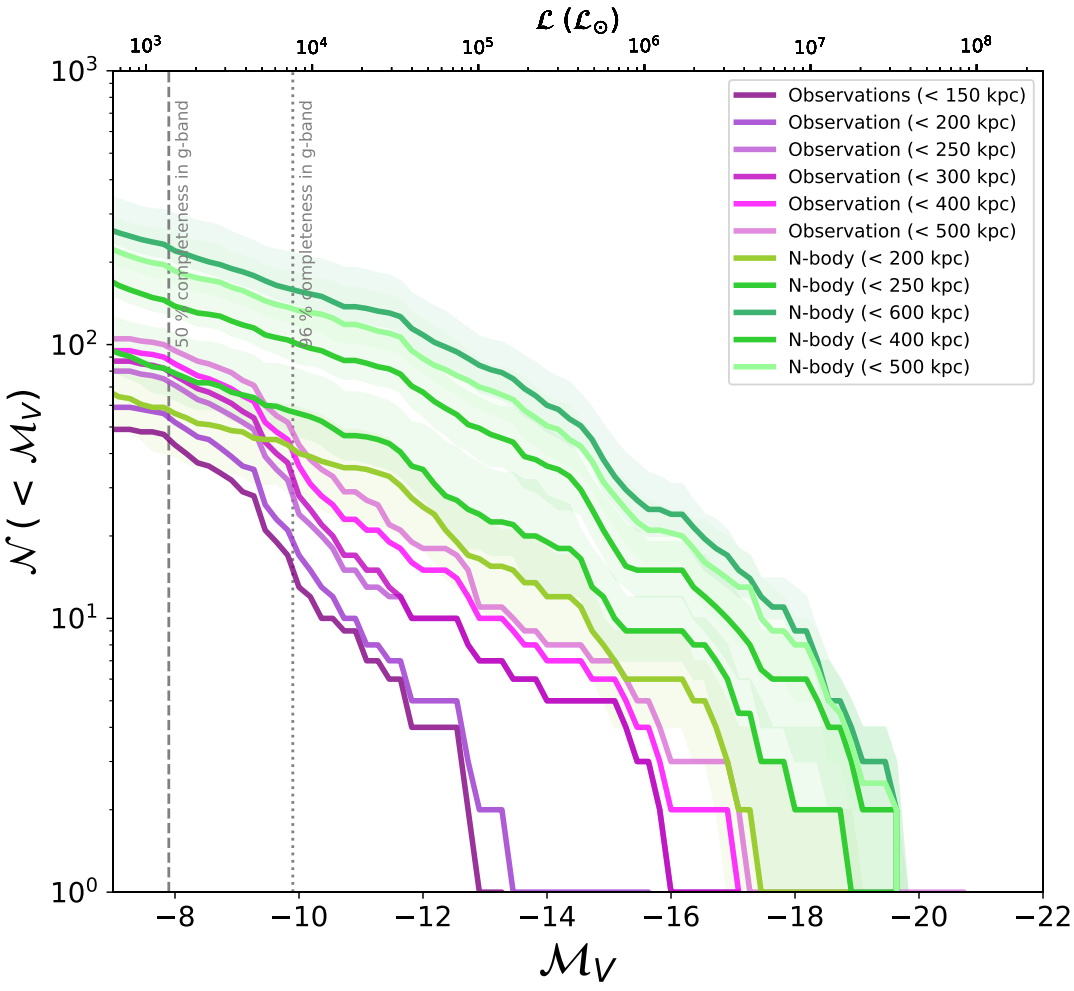

Figure 7.1: Luminosity functions for observed and modeled Cen A satellites. Each curve shown in shades of purple (observations) and green (models) correspond to cumulative luminosity function within 150, 200, 250, 300, 400, and 500 kpc. 50% and 96% completeness limits within 150 kpc of Cen A in g-band based on results of Leahy et al. ((private communication)) is shown in dashed grey lines. This peculiar feature starts to emerge for luminosity functions within 200 kpc.

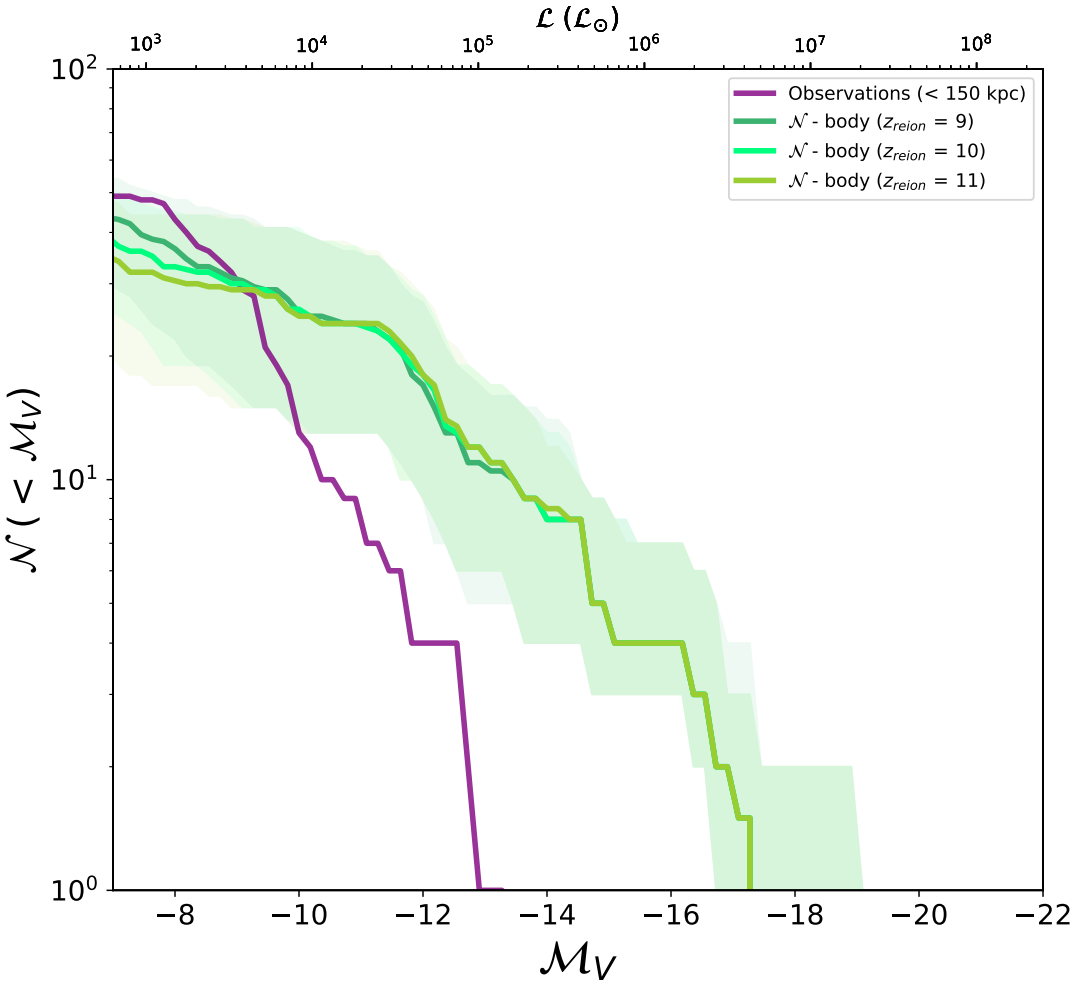

Figure 7.2: Luminosity functions for the Cen A satellites within 150 kpc. Purple plot shows the observations within 150 kpc and $M_V \leq -7$ in the y-z plane are shown in green. Models for different reionization redshifts are shown in shades of green. Reionization redshift suppress star formation in the faintest dwarfs. But we see minimal effect on the luminous dwarfs.

the redshifts of 6 and 14 (Fan et al. 2006, Furlanetto et al. 2006, Morales and Wyithe 2010). In Figure 7.2, we show the luminosity functions for our galaxy models within 150 kpc for different reionization redshifts $z = 9, 10, 11$. We do not test $z > 11$ because we underpredict the fainter dwarfs with $z = 11$ compared to observations. As expected, the fainter end of the luminosity function flattens as the redshift of reionization increases.

This makes sense, given that reionization occurs earlier in those models, mass accretion into those halos is suppressed longer. However, changing the reionization redshift cannot replicate the steeper effect seen in the observed luminosity function. Reionization redshift affects only the fainter end of the luminosity function, decreasing the fainter dwarfs as the reionization redshift increases. Thus, there is no change to the luminosity function in the inner region we are interested in. Therefore, inner dwarfs within 150 kpc of Cen A cannot be explained by an earlier reionization redshift.

7.2 Tidal Effects

Another parameter that could decrease the luminosity of dwarf satellites and eject stars from their halos is tidal stripping due to tidal forces of the host halo. Thus, is a viable way that could have caused higher mass halos to lose their stars. Because Cen A is more massive than the Milky Way, its tidal stripping might be more powerful than in the LG. Therefore, we investigate the effects of both tidal stripping of stars and gas in the ISM and the tidal destruction of halos. These two methods helps us explore whether tidal stripping of baryons or tidal destruction of dark matter halos due to strong tidal fields are responsible for lack of brighter satellites.

7.2.0.1 Effect of Tidal Stripping Efficiency of The ISM

We start by implementing tidal stripping efficiency of the ISM. This method assumes that any dark matter stripping has been handled by the N-body simulation. Details on the implementation of tidal stripping algorithm can be found in 3.2.2 and Equation 3.12.

In Figure 7.3, we explore the luminosity function of Cen A satellites within 150 kpc for various tidal stripping efficiencies. Note, although we use the same tidal stripping efficiencies explored in 3.2.2, the strength of the tidal force is higher in Cen A since the tidal field depends on M_{host}.

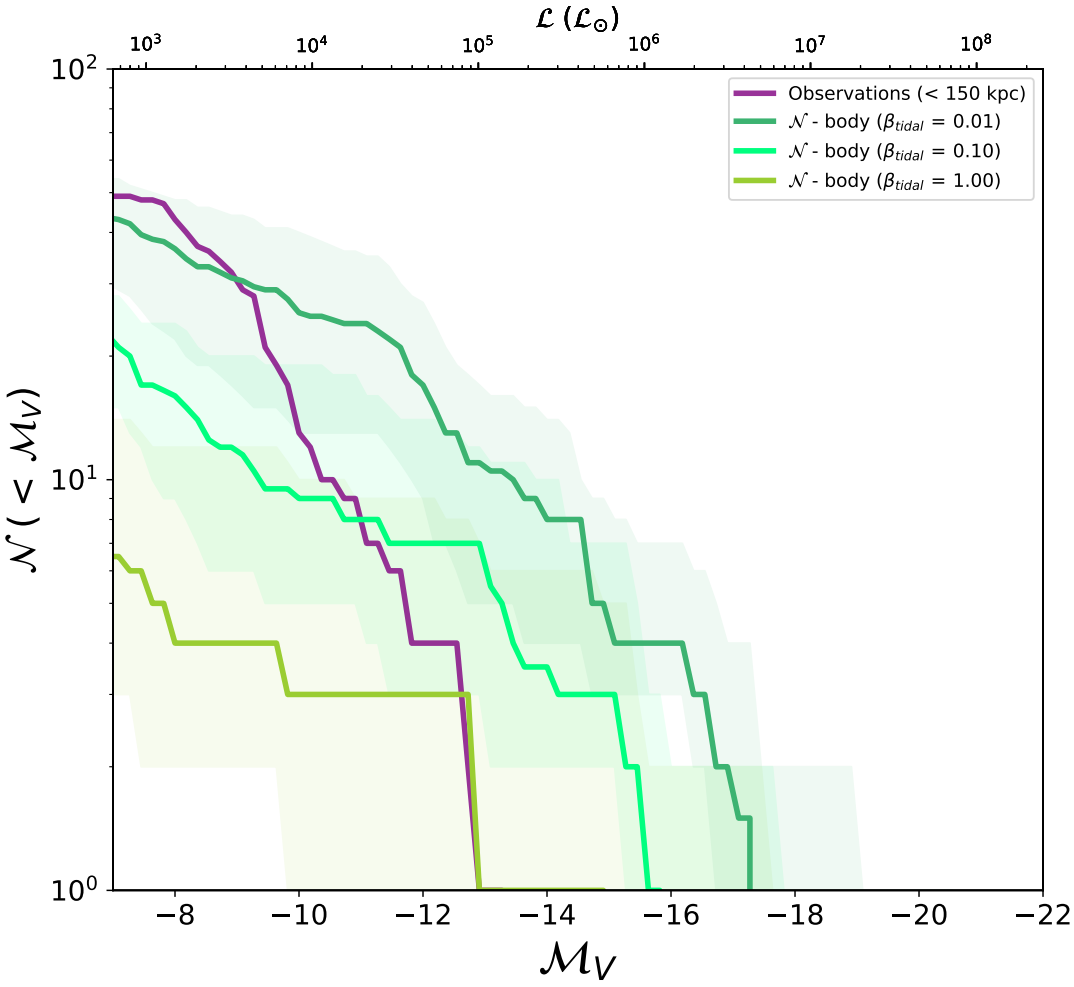

Figure 7.3: This figure shows the luminosity functions for the Cen A satellites within 150 kpc. Models for different ISM tidal stripping efficiencies are shown in shades of green and observations of Cen A dwarfs are shown in purple. Tidal stripping suppress star formation in all dwarfs not just in more luminous dwarfs.

As expected, the number of dwarfs at all luminosities decreases with an increasing

tidal stripping efficiency of the ISM. The effect is similar to what we saw for the Milky Way satellites in 3.2. Therefore, the tidal stripping efficiency only changes the normalization of the luminosity function and not the slope. This agrees with the results of Müller et al. (2019) since they do not find any evidence for tidal stripping in their sample either. Their sample has 15 dwarf galaxies within $-12 \leq M_V \leq -8$. Therefore, we can rule out tidal stripping as a possible culprit of the steepening effect of the luminosity function within 150 kpc.

7.3 Effect of Tidal Destruction of Halos

While tidal stripping efficiency for ISM does not quench the more luminous dwarfs, the tidal stripping method implemented previously is simpler and applied only to ISM. Because it assumes that tidal stripping of dark matter has already been dealt with in the N-body simulation and only implements stripping a fraction of ISM gas and stars. Would our results change if we implemented an additional model for tidal destruction of dark matter halos? We test this tidal destruction model on our modeled Cen A dwarf galaxies, as we expect it to be stronger for satellites closer to the center of Cen A. This method uses a detailed model of sub-halo orbits/tidal evolution using Li et al. (2020) model of orbital parameter distribution. Li et al. (2020) describes the orbital parameter distribution of infalling subhalos through cosmic time. This allows us to track the orbits of subhalos in the simulation and determine when it approaches $r \leq f_{rvir}\, r_{vir}$. According to Li et al. (2020), the orbit of the satellite halo is set by two parameters for a spherical potential of halo, infall velocity, v and angle between position vector and velocity θ.

Thus, radial and tangential velocity is described by $v_r = v\cos\theta$ and $v_t = v\sin\theta$. The probability of normalized velocity $u = v/V_h$ of the infalling subhalos follows a lognormal distribution,

$$p(u)du = \frac{1}{\sqrt{2\pi}\sigma_1}\exp\left[-\frac{ln^2(u/\mu_1)}{2{\sigma_1}^2}\right]\frac{du}{u}, \tag{7.1}$$

where the virial velocity of the halo $V_h = \sqrt{GM_h/R_h}$ satisfies $\int_0^\infty P(u)du = 1$ for any positive μ_1 and σ_1.

The probability distribution of the infall angle $\cos^2(\theta) = {v_r}^2/v^2$ follows an exponential distribution given by

$$p(\cos^2\theta|u,\nu,\xi)d\cos^2\theta = \frac{\eta}{e^\eta - 1}\exp(\eta\cos^2\theta)d\cos^2\theta, \tag{7.2}$$

where ν is the peak height of the host, ξ is the sub-to-host mass ratio, and η is given by

$$\eta = a_0\exp\left[-\frac{ln^2(u/\mu_1)}{2{\sigma_1}^2}\right] + A(u+1) + B, \tag{7.3}$$

with $A = a_1\nu + a_2\xi^c + a_3\nu\xi_c$ and $B = b_1 + b_2\xi^c$. Note that the above distribution satisfies $\int_0^1 p(\cos^2\theta)d\cos^2\theta = 1$ for any η.

The effect of tidal destruction is implemented such that if a subhalo reaches a certain percentage (f_{virial}) of virial radius of their host halo, it will be destroyed. We implement three virial fraction values, 1%, 10%, and 33%. Figure 7.4 shows the effect of tidal destruction on the luminosity function within the inner region ($< 150\,\mathrm{kpc}$). As the percentage of virial fraction increases, the median number density of fainter dwarfs

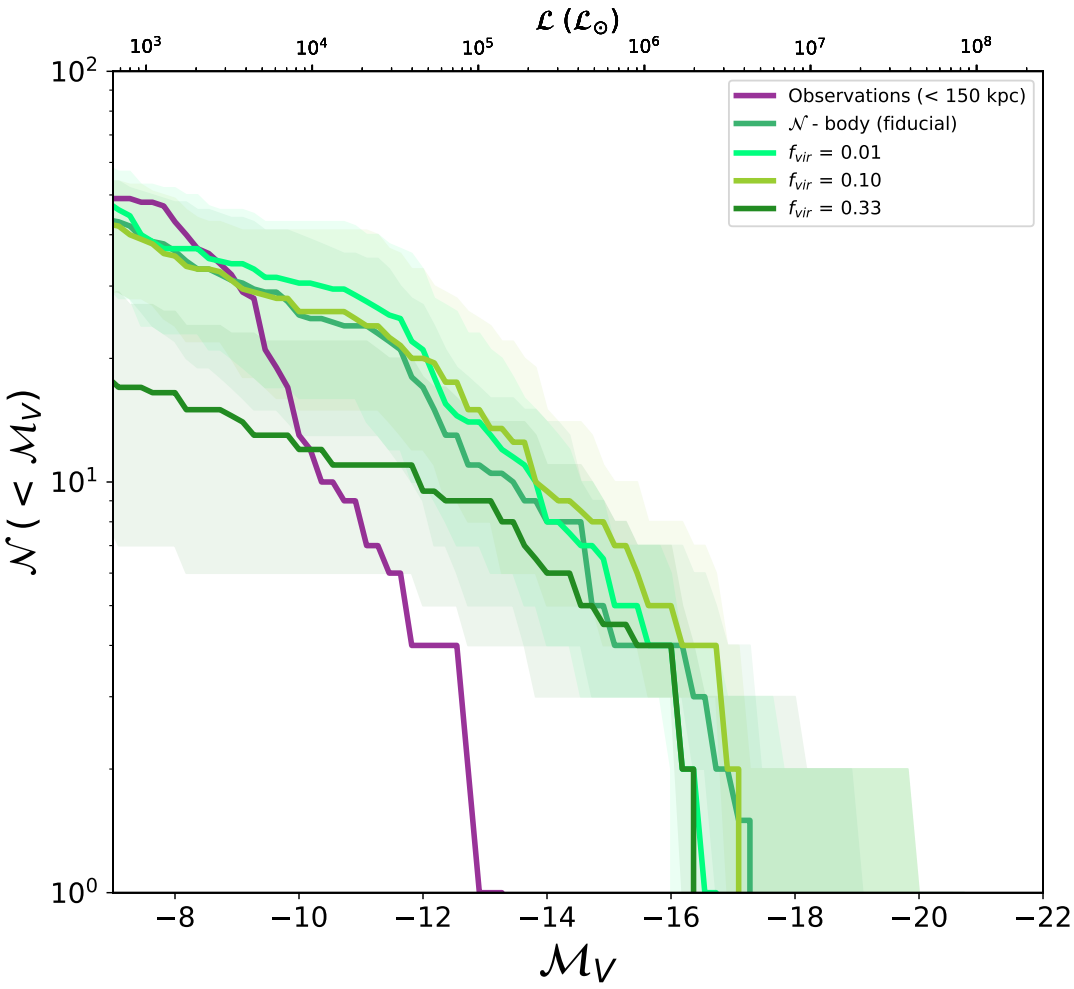

Figure 7.4: This figure shows the luminosity function for Cen A satellites within 150 kpc. Observations in purple, and models with different virial fractions (f_{virial}) in shades of green. Virial fraction radius determines the fraction of the virial radius of Cen A where subhalos will be destroyed due to tidal destruction.

decreases. Note that the envelope corresponding to margins between maximum and minimum number densities at each magnitude also increases. While the drop in number density of satellites for increasing the virial fraction from $1\% - 10\%$ does not make a difference, we do see a significant drop when the virial fraction of subhalos is increased to 33%.

We observe the most flattening effect for $f_{vir} = 33\%$ for satellites fainter than $M_V \sim -13\,mag$. While some luminous dwarfs are affected, such impact is insignificant. But is possible that our models underestimate tidal effects or underestimate the amount of merging in the inner region. It destroys most fainter subhalos flattening the luminosity function within 150 kpc rather than steepening it. Tidal destruction of subhalos flattens the luminosity function but does not produce a steepening effect. Therefore, we cannot attribute tidal destruction of Cen A satellites to the lack of luminous satellites within inner Cen A at this time.

7.4 Effect of Filtering Velocity

Next, we investigate if filtering velocity can change the slope of the luminosity function within 150 kpc. Reheating of the IGM during reionization suppresses the accretion of gas into low mass halos below the filtering mass (Ricotti and Gnedin 2005). We do not use mass because it is redshift dependent, whereas circular velocity is not. Filtering velocity (v_{filter}) corresponds to this filtering mass and the IGM temperature. Thus gas accretion in fossil galaxies or galaxies with circular velocities $< 20 - 30\,km\,s^{-1}$ (Bovill and Ricotti 2011) are suppressed by reionization.

Therefore, we check if the luminosity function changes with changes to IGM temperature from filtering velocity. We show models for three different v_{filter} (40, 60, 80 km/s). While 40 km/s is astrophysically reasonable value latter 60 km/s and 80 km/s are not physical ($> 20,000\,K$). In an IGM that reionizes at $z = 9$, virial temperature would reach a temperature of $\sim 46,000\,K$ for $v_{filter} = 80\,km\,s^{-1}$. But this value is not physical since the temperature of the IGM at reionization is $\sim 2 \times 10^4\,K$. Thus only halos with $\sim 5 \times 10^8\,\mathrm{M}_\odot$ could accrete gas from the IGM, artificially suppressing accretion onto halos. Although these values are not physical, they could still hint at a higher temperature for IGM. As a result, we test these values as well.

In Figure 7.5, we show how the luminosity function changes within 150 kpc for 40, 60, and 80 $km\,s^{-1}$. We show that as the filtering velocity increases, the slope of the luminosity function steepens. In fact, both the normalization and slope of the luminosity function for $v_{filter} = 80\,km\,s^{-1}$ match that observed for Cen A satellites with $d < 200$ kpc. Thus, a filtering velocity of $80\,km\,s^{-1}$ with a z_{reion} of 9 successfully suppresses star formation in brighter dwarfs.

To quantify the comparison between models and observations, we compare the luminosity functions within 150 kpc using a 2-sample K-S test to determine if they come from the same distribution. Since the null hypothesis is that the two samples come from the same distribution, we find the following p values; 0.009 for $v_{filter} = 40\ km\,s^{-1}$, 0.02 for $v_{filter} = 60\ km\,s^{-1}$, and 0.57 for $v_{filter} = 80\ km\,s^{-1}$. Since p-value of $v_{filter} = 80\ km\,s^{-1}$ is greater than 0.05, we cannot reject the null hypothesis, and that model might come from the same distribution as the observations. While the temperature of $\sim 46,000\,K$

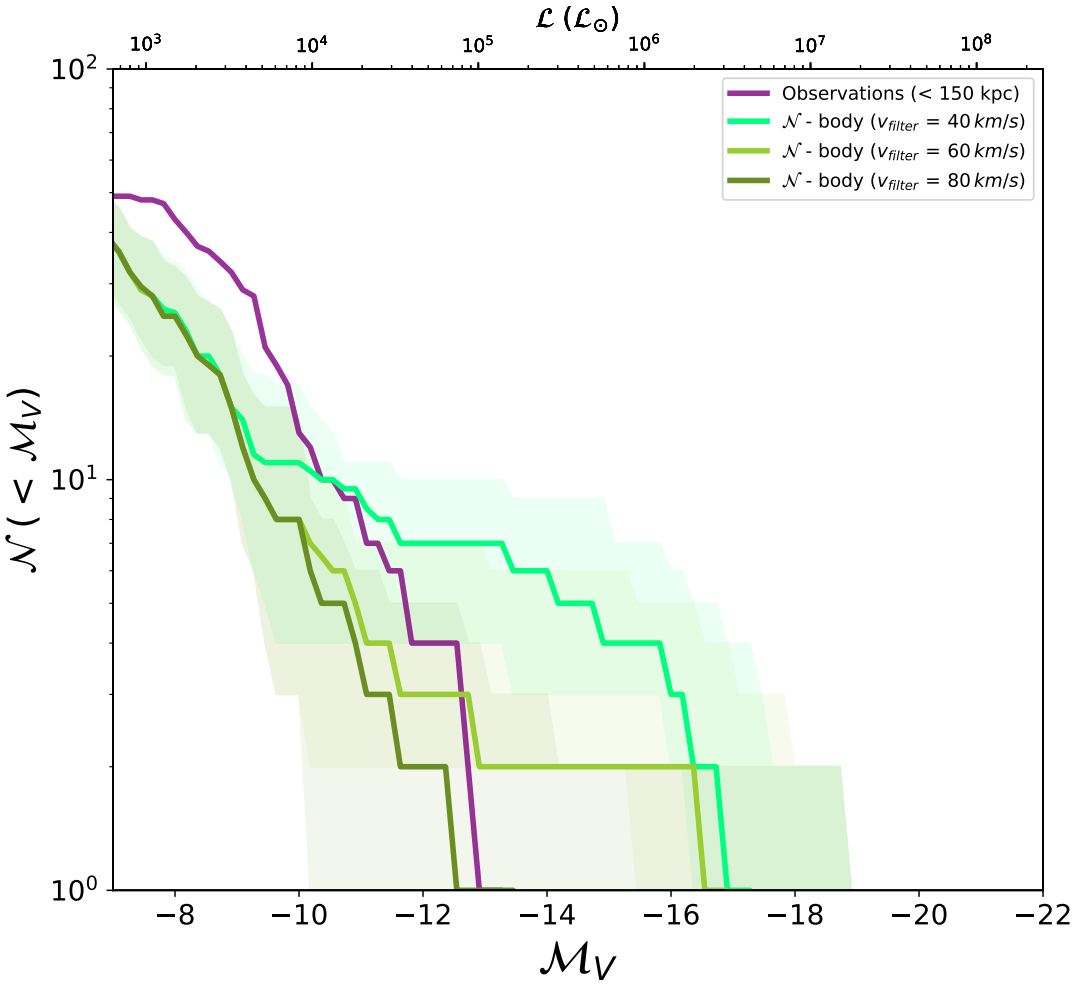

Figure 7.5: Luminosity functions for the Cen A satellites within 150 kpc for models with different filtering velocities. Purple plot shows the observations within 150 kpc and $M_V \leq -4$ in the y-z plane are shown in green. Models corresponding to different reionization suppression velocities are shown in shades of green (40,60, 80 $km\,s^{-1}$).

for $v_{filter} = 80\,km\,s^{-1}$ is not physical at $z_{reion} = 9$, it would be physical in Warm Hot Intergalactic Medium (WHIM) or if there is some source such as AGN ionizing the IGM of galaxies in the inner halo.

In summary, we find that the lack of luminous satellites within 200 kpc of the Cen A halo is not caused by change in reionization redshift, filtering velocity, tidal stripping

efficiency, and tidal destruction of subhalos. However, heating of the IGM by an AGN could be possible.

7.5 Star Formation Histories

Now that we know there exists some quenching at play in the inner region of Cen A, let us explore the SFHs of its satellites. Few observed SFHs available from Crnojević et al. (2012) show that dwarf galaxies close to the Cen A and in a denser environment have a lower fraction of star formation compared to isolated dwarfs. In addition, they also find the ratio of neutral gas mass to baryonic mass and neutral gas mass to average SFR is significantly lower for dwarfs close to the host galaxy. Therefore, the observed SFHs further confirm presence of quenching in the inner region of Cen A.

7.5.1 τ_{90} vs. τ_{50}

In Figure 7.6 we have shown $\tau_{90}\, vs.\, \tau_{50}$ for Cen A satellites within 600 kpc. Each point is colored by the absolute V band magnitude and sized by half-light radii. τ_{90} increase with increasing τ_{50} as expected. Notice that some satellites that quench 50% of mass 11 Gyrs ago quench much later if they decline SFR slowly. There are two star formation quenching events shown by dashed dot and dashed curves, which correspond to star formation rates that decline in orders of 4 and 7 Gyrs respectively. In addition, some of the τ_{50} values predicted by our models agree with the observed values of KK196 and ESO269-58 (Crnojević et al. 2012).

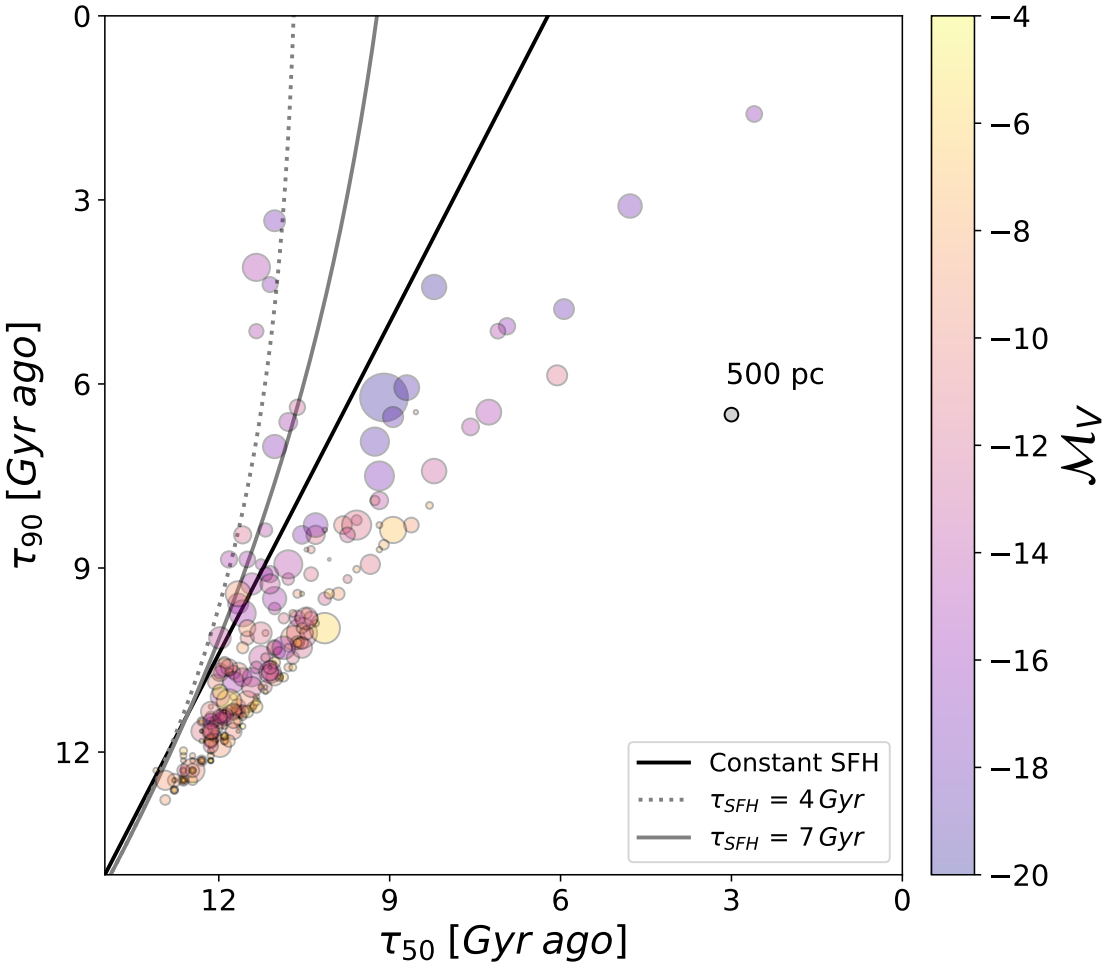

Figure 7.6: τ_{90} vs. τ_{50} for Cen A satellites within 600 kpc. Each point shows the time taken to gain 90% stellar mass at $z = 0$ vs. time taken to gain 50% of the stellar mass at $z = 0$ for a satellite galaxy, sized by their half light radii and colored by absolute magnitude ($g_{\rm DES}$). The curves show galaxies undergoing exponentially declining SFRs.

7.6 Discussion

As discussed in previous sections, the reason for this dearth of luminous satellites within 200 kpc of the Cen A halo is a mystery. We can observe this same feature of the luminosity function in Figure 11 of Müller et al. (2019). Their models from Illustris-TNG simulations for different host halo masses reveal that the host halo mass might not be a

culprit of this issue. While we test several quenching mechanisms including reionization redshift, filtering velocity, tidal stripping, and tidal destruction in our models, none of these parameters seem to have caused quenching of these luminous dwarfs within 150 kpc. Our models get closest to the observed luminosity function within 150 kpc of Cen A when a filtering velocity of $80\,km\,s^{-1}$ is implemented with $z_{reion} = 9$. While higher IGM temperatures are not physical at reionization, this implies that some phenomena might be raising the IGM temperature at a later time.

Our clue to solve the mystery is the high IGM temperature. So, what is capable of heating gas to $v_{filter} = 80\,km\,s^{-1}$? One culprit could be AGN. This is not surprising given there is evidence of AGN activity in Cen A (Sun et al. 2016). The second clue is Cen A's major merger: We know Cen A has experienced at least one major merger. According to Wang et al. (2020), Cen A had a major merger 2 Gyrs ago. Given that major mergers can activate Super Massive Black Holes (SMBHs), could Cen A's AGN have been activated after a major merger? This question remains unanswered as the merger or AGN's effect on its satellite population has not been quantified yet. Unraveling if or how either could have affected the Cen A satellites requires further careful study. If AGN or a major merger quench star formation, what other signatures would this leave? The quenching lines that we see in SFHs of our Cen A analog could be a smoking gun of these quenching events. However, further analysis of SFHs and signatures of quenching is a subject of future work.

7.7 Conclusions

We model the dwarf satellites of Cen A with Galacticus SAM (Benson 2012). We have explored luminosity function of Cen A satellites around the inner halo. The summary of our results is as follows,

- Exploration of the luminosity function within 150 kpc of the host reveals a lack of luminous satellites that is not reflected in the models. Note that we can assume 100% completeness for these brighter dwarfs. While it is unusual to observe fewer brighter dwarfs, our comparisons agree with results of Müller et al. (2019). Although our models can predict the correct number of dwarfs within 150 kpc of Cen A $M_V \leq -6\,mag$, they overproduce the number of luminous dwarfs $M_V \leq -13$.

- Although we do not reproduce the correct slope of the luminosity function within 150 kpc, we do reproduce the correct number of luminous dwarfs within 150 kpc (see left panel of Figure 6.3). Note that observations are 96% complete down to 18 mag in the g band. Analysis of observed luminosity functions show that steeper slope of the luminosity function begins to appear between $\sim 200 - 250$ kpc.

- In order to find the cause of missing luminous satellites, we vary parameters that could suppress or eject stars/gas in these satellite galaxies.

- We find reionization redshift has no effect on the luminous satellites within the inner region of Cen A.

- Implementation of different tidal stripping efficiencies for loss of ISM mass affects all dwarf galaxies within 150 kpc and does not produce the expected observed steeper

luminosity function.

- Destruction of dark matter halos via tidal forces flattens the luminosity function within 150 kpc of Cen A models and does not have a steepening effect for more luminous dwarfs.

- Higher filtering velocities suppress accretion of gas from IGM into halos. We find these velocities to be not physical at $z_{reion} \sim 9$. However, this could have implications for IGM temperatures caused by other phenomena at a later time.

- While we do not know the exact phenomena causing this, it might be due to Cen A's major merger, or the activity in Cen A's AGN due to this major merger.

- Determining whether these have affected Cen A dwarf satellites at all will require detailed and careful study.

- Further analysis of SFHs of Cen A shows that despite not being able to reproduce the correct slope of the luminosity function, we are still able to produce reasonable SFHs within available observations of Crnojević et al. (2012).

In this chapter, we investigated the unknown phenomena that are responsible for the dearth of luminous satellites $< 200\,\mathrm{kpc}$. While this work does not find the mechanism responsible for this feature, it eliminates reionization redshift, reionization velocity, and tidal stripping as prospects. However, a detailed investigation of other phenomena will be a subject of a future study.

Chapter 8

Conclusions & Future Directions

In this chapter, we summarize the results and conclusions of this dissertation and present a brief overview of our future plans below. Components of this chapter is drawn from Weerasooriya et al. (2023). Weerasooriya et al. (in prep. a) and Weerasooriya et al. (b.) will draw from large components of this chapter.

In previous chapters, we presented models of dwarf galaxies around Cen A analogs using Galacticus. First we constrained the astrophysical prescriptions and parameters for the Milky Way satellite galaxies in Chapter 3. We modeled the Milky Way satellites using the semi-analytic model Galacticus (Benson 2012) run on merger trees from a high resolution N-body simulation of a Milky Way analog. Using available astrophysical priors, we tuned the gas cooling in halos, star formation and feedback recipes to reproduce the observed luminosity function and the luminosity-metallicity relation of the Milky Way satellites (McConnachie 2012, Drlica-Wagner et al. 2020), the simulated luminosity functions from the Mint Justice League (Applebaum et al. 2021), and mock observations of FIRE-II (Shipp et al. 2022).

In Chapter 6, we modeled the satellite dwarf galaxies of Cen A using the astrophysical prescriptions and parameters for the Milky Way. Our models are able to reproduce the overall properties of the dwarf population fairly well. Here we applied the best parameter space that reproduced the dwarfs of the Milky Way (Weerasooriya et al. 2023) to several Cen A analogs of both N-body and EPS models with its satellite galaxies. In Chapter 7 we explored the luminosity function within the inner region of Cen A in detail and star formation physics that might be responsible for quenching of brighter dwarfs.

Our conclusions are as follows.

- Our models reproduce the luminosities and metallicities of the Milky Way satellites down to $M_{\rm V} \sim -6$ without implementation of H_2 cooling in our current model. We reproduce several other $z = 0$ properties of the Milky Way dwarfs, including half-light radii, velocity dispersion and mass-to-light ratios without any additional tuning of the physics.

- Without further tuning, our model reproduces star formation histories that are consistent with observations (Weisz et al. 2014; 2019).

- We reproduce the global properties of Cen A satellites at $z = 0$ with the same astrophysical prescriptions and parameters that reproduce the Milky Way satellites. This suggests that SF physics governing feedback physics is independent of the external environment. Note that we do not produce all properties due to lack of observations for comparison.

- However, our models cannot reproduce steeper luminosity function for inner 200 kpc.

We investigate possible quenching mechanisms in Cen A's inner region by varying astrophysical prescriptions and parameters pertaining to tidal stripping, tidal destruction, reionization redshift, reionization velocity, etc.

- While tidal effects and reionization redshift seem to affect fainter dwarfs, they do not change the brighter end of the luminosity function. Filtering velocity of $80\,km\,s^{-1}$ at $z_{reion} = 9$ produces the correct shape of the slope with effects to brighter dwarfs. While the IGM temperature corresponding to $v_{filter} = 80\,km\,s^{-1}$ is unphysical at reionization, a higher IGM temperature at a later time is still a possibility.

- This might be caused by Cen A's major merger, or the activation of Cen A's AGN due to this major merger.

This work shows the ability of Galacticus to reproduce the $z = 0$ properties and star formation histories of dwarf galaxies down to the luminous ultra-faints, providing a new tool for investigating the astrophysics of star formation and feedback in the lowest mass systems in the Milky Way and Cen A. We conclude that while overall population of dwarfs in Cen A is similar to that of the Milky Way, the inner region may be affected by environmental effects. While our models cannot reproduce this effect, we hypothesis it may be caused by quenching of brighter dwarfs in the inner halo ($< 200\,kpc$) due to high IGM temperature.

8.1 Future Directions

8.1.1 Implementation of H_2 Cooling for The Milky Way Satellites

In Chapters 3,4, and 5 we showed the properties and SFHs of the Milky Way dwarfs. While we are able to reproduce the ultra-faints these results are obtained without implementation of molecular hydrogen cooling which is essential to the cooling of ultra faint dwarf galaxies. Therefore, we intend to implement molecular hydrogen cooling method that is already available in GALACTICUS to reproduce SFHs of the Milky Way satellites. In addition, we also hope to apply the same parameter space to several other high resolution simulations that will be available to us through Dr. Robyn Sanderson.

8.1.2 SFHs of Cen A Analogs

We are currently exploring a statistical sample of SFHs of Cen A EPS merger trees with different host masses, and several merger trees of the same mass. We use the same EPS merger trees described in Chapter 2. The goal of this investigation is to determine if there is are visible patterns in quenching of dwarfs throughout their history. This would allow an statistical exploration of SFHs of Cen A satellites with minimal computational cost.

Appendix A

Observations of Centaurus A

The table below shows a compilation of observational data for Centaurus A dwarf satellites from various sources. In Table A.1, we present a compilation of observations from a variety of sources used in this study along with their references.

Table A.1: **References:** (1) Lauberts and Valentijn (1989), (2) de Vaucouleurs et al. (1991),(3) Karachentsev et al. (2003),(4) James et al. (2004), (5) Doyle et al. (2005), (6) Sharina et al. (2008), (7) Karachentsev et al. (2013), (8) Müller et al. (2015), (9) Müller et al. (2017), (10) Crnojević et al. (2014), Crnojevic et al. (2016), Crnojević et al. (2019), (11) (Taylor et al. 2018).

Name	**RA**	**Dec**	M_B	M_V	**D**	**References**
	(hh:mm:ss)	(dd:mm:ss)	(mag)	(mag)	(Mpc)	
NGC4945	13:05:26.1	-49:28:16.0	-20.34	-20.6	3.47	1,7
NGC5102	13:21:57.8	-36:37:47.0	-18.24	-20.37	3.66	1,7
E274-01	15:14:13.5	-46:48:45.0	-17.35	-19.2	2.79	2,7
NGC5253	13:37:5.0	-31:23:30.0	-17.33	-17.7	3.9	1,7

Continued on next page

Table A.1 – *Continued from previous page*

Name	**RA**	**Dec**	M_B	M_V	**D**	**References**
E383-087	13:49:17.5	-36:03:48.4	-16.83	-17.17	3.19	1,7
NGC5206	13:30:41.0	-47:53:42.0	-16.43	-16.97	3.6	1,7
NGC5408	14:00:18.0	-41:08:11.0	-15.91	-17.3	4.81	2,7
E324-24	13:27:37.4	-41:28:50.0	-15.49	-15.6	3.78	2,7
E26958	13:07:38.0	-46:43:30.0	-14.99	-16.8	4.78	6,7
NGC5237	13:37:38.9	-42:50:51.0	-14.82	-15.08	3.33	3,5,7
E272-25	14:43:25.5	-44:42:19.0	-14.52	-16.4	5.8	3,6,7
NGC5011C	13:13:11.9	-43:15:56.0	-14.15	-15.8	3.73	2,3,7
E325-11	13:45:0.8	-41:51:32.0	-14.02	-14.5	3.4	3,6,7
KK190	13:13:9.2	-44:53:24.0	-13.68	-15.2	3.75	6,7
KKS54	11:37:53.4	-39:13:14.0	-13.66	-14.3	3.75	6,7
E384-016	13:57:1.6	-35:20:2.0	-13.47	-14.8	4.49	6,7
KK197	13:22:1.8	-42:32:8.0	-13.19	-12.6	3.84	7,11
PGC51659	14:28:3.7	-46:18:6.0	-13.15	999.0	3.61	7
E21910	12:56:9.6	-50:08:38.0	-12.94	999.0	4.7	7
E321-014	12:13:49.6	-38:13:53.0	-12.8	-13.43	3.33	1,7
KK196	13:21:47.1	-45:03:48.0	-12.73	-12.5	3.96	7
E269-037	13:03:33.58	-46:35:5.9	-12.67	-12.61	3.15	1,7
KKs55	13:22:12.4	-42:43:51.0	-12.14	-12.4	3.85	3,7

Continued on next page

Table A.1 – *Continued from previous page*

Name	**RA**	**Dec**	M_B	M_V	**D**	**References**
KK179	13:00:41.0	-46:19:0.0	-12.13	-12.61	3.48	1,7
CenA-MM-Dw1	13:30:14.3	-41:53:36.0	-12.1	-13.8	3.91	9
KK211	13:42:5.6	-45:12:18.0	-11.99	-13.32	3.68	6,7
CenA-MM-Dw3	13:30:21.5	-42:11:33.0	-11.94	-13.1	3.87	9
HIPASSa	13:34:29.7	-39:36:59.0	-11.64	999.0	3.85	3
KKs51	12:44:21.5	-42:56:23.0	-11.46	-16.0	3.8	7,9
KK213	13:43:35.8	-43:46:9.0	-11.41	-10.0	3.77	7,9
KK189	13:12:45.0	-41:49:55.0	-11.33	-11.2	4.23	9
KKs53	13:11:14.2	-38:54:22.0	-11.26	999.0	3.8	7
HIPASSc	13:45:49.8	-37:43:34.0	-11.25	999.0	3.6	3
KK221	13:48:46.4	-46:59:49.0	-11.21	999.0	3.82	7
HIPASSb	13:48:5.4	-46:43:23.0	-10.94	999.0	3.6	7
CenN	13:48:9.2	-47:33:54.0	-10.93	-12.7	3.66	6
KKs57	13:41:38.1	-42:34:55.0	-10.81	-11.36	3.83	7
KK217	13:46:17.2	-45:41:5.0	-10.67	-12.3	3.5	6
KK203	13:27:28.1	-45:21:9.0	-10.62	-10.5	3.77	11
dw1341-43	13:41:37.0	-43:51:17.0	-10.54	-10.1	3.53	9
KKS58	13:46:0.8	-36:19:44.0	-10.49	-11.9	3.8	7,10
CenA-MM-Dw8	13:33:34.1	-41:36:28.0	-10.19	-9.7	3.47	10

Continued on next page

Table A.1 – *Continued from previous page*

Name	**RA**	**Dec**	M_B	M_V	**D**	**References**
dw1323-40	13:24:53.0	-40:45:41.0	-10.14	-10.4	3.73	9
CenA-MM-Dw4	13:23:2.6	-41:47:10.0	-10.0	-9.9	4.09	10
CenA-MM-Dw9	13:33:1.5	-42:31:48.0	-9.91	-9.1	3.8	10
dw1323-40b	13:23:55.0	-40:50:9.0	-9.88	-9.9	3.91	9
dw1322-39	13:22:32.0	-39:54:20.0	-9.67	-10.0	2.95	9
dw1342-43	13:42:44.0	-43:15:19.0	-9.14	-9.8	2.9	9
dw1336-44	13:36:44.0	-44:26:50.0	-9.0	-8.6	3.5	9
dw1329-45	13:29:10.0	-45:10:31.0	-8.92	-8.4	2.9	9
CenA-MM-Dw11	13:17:49.2	-42:55:37.0	-8.73	-9.4	3.52	10
CenA-MM-Dw6	13:25:57.6	-41:05:39.0	-8.51	-9.1	4.04	10
CenA-MM-Dw7	13:26:28.7	-43:33:24.0	-8.35	-7.8	4.11	10
CenA-MM-Dw2	13:29:57.3	-41:52:23.0	-8.05	-9.7	4.15	10
CenA-MM-Dw10	13:24:32.9	-44:44:7.0	-7.15	-7.8	3.27	10
CenA-MM-Dw5	13:19:52.4	-41:59:37.0	-6.6	-8.2	3.61	10
dw1325-33	13:25:41.0	-33:00:25.0	-9.57	999.0	4.9	8
dw1326-29	13:26:4.0	-29:24:16.0	-9.82	999.0	4.9	8
dw1326-35	13:26:44.0	-35:05:0.0	-9.72	999.0	4.9	8
dw1328-29	13:28:12.0	-29:28:45.0	-9.49	999.0	4.9	8
dw1329-32	13:29:58.0	-32:29:46.0	-11.19	999.0	4.9	8

Continued on next page

Table A.1 – *Continued from previous page*

Name	**RA**	**Dec**	M_B	M_V	**D**	**References**
dw1330-32	13:30:54.0	-32:18:21.0	-9.47	999.0	4.9	8
dw1330-33	13:30:4.0	-33:50:6.0	-8.12	999.0	4.9	8
dw1330-34	13:30:2.0	-34:00:14.0	-9.6	999.0	4.9	8
dw1334-32	13:34:5.0	-32:06:28.0	999.0	999.0	4.9	8
dw1335-29	13:35:46.0	-29:42:24.0	-9.6	999.0	4.9	8
dw1335-33	13:35:25.0	-33:18:0.0	-11.33	999.0	4.9	8
dw1336-32	13:36:33.0	-32:18:5.0	-10.59	999.0	4.9	8
dw1337-26	13:37:13.0	-26:48:10.0	-10.31	999.0	4.9	8
dw1337-33	13:37:2.0	-33:31:25.0	-10.66	999.0	4.9	8
dw1340-30	13:40:19.0	-30:21:35.0	-9.09	999.0	5.06	8
dw1341-33	13:41:13.0	-33:49:30.0	-10.26	999.0	4.9	8
KK195	13:21:8.2	-31:31:47.0	-11.76	999.0	5.22	7
KK200	13:24:36.0	-30:58:20.0	-12.89	999.0	4.76	7
IC4247	13:26:44.4	-30:21:45.0	-14.43	-14.9	5.18	2,7
E444-78	13:36:31.11	-29:14:5.6	-14.7	-14.7	5.42	6,7
E444-84	13:37:20.2	-28:02:46.0	-13.56	-14.0	4.61	5,7
IC4316	13:40:18.1	-28:53:40.0	-14.39	-13.6	4.35	2,3
NGC5264	13:41:37.0	-29:54:50.0	-16.02	999.0	4.79	1,7
CenA-dE4	13:46:39.5	-29:58:45.0	-10.4	999.0	4.94	1,7

Continued on next page

Table A.1 – *Continued from previous page*

Name	**RA**	**Dec**	M_B	M_V	**D**	**References**
dw1240-42	12:40:2.0	-42:24:44.0	-9.77	999.0	3.6	9
dw1241-32	12:41:27.0	-42:53:45.0	-8.64	999.0	3.6	9
dw1243-42	12:43:13.0	-42:27:48.0	-9.32	999.0	3.6	9
dw1243-42b	12:43:11.0	-42:26:37.0	-10.03	999.0	3.6	9
dw1251-40	12:51:56.0	-40:19:53.0	-8.28	999.0	3.6	9
dw1252-40	12:52:1.0	-40:21:55.0	-11.05	999.0	3.6	9
dw1252-43	12:52:25.0	-43:05:58.0	-8.36	999.0	3.6	9
dw1257-41	12:57:45.0	-41:22:52.0	-10.44	999.0	3.6	9
dw1258-37	12:58:29.0	-37:07:21.0	-8.93	999.0	3.6	9
dw1301-30	13:01:28.0	-20:06:43.0	-9.42	999.0	4.9	9
dw1302-40	13:02:49.0	-40:08:35.0	-9.1	999.0	3.6	9
dw1306-29	13:06:48.0	-29:53:30.0	-9.79	999.0	4.9	9
dw1314-28	13:14:2.0	-28:12:12.0	-10.74	999.0	4.9	9
dw1318-21	13:18:4.0	-21:53:6.0	-10.27	999.0	4.9	9
dw1321-27	13:21:8.0	-27:44:66.0	-9.6	999.0	4.9	9
dw1322-27	13:22:6.0	-27:34:45.0	-10.54	999.0	4.9	9
dw1326-37	13:26:22.0	-37:23:8.0	-8.76	999.0	3.6	9
dw1330-38	13:30:41.0	-31:10:3.0	-8.02	999.0	3.6	9
dw1331-40	13:31:26.0	-40:15:47.0	-7.1	999.0	3.6	9

Continued on next page

Table A.1 – *Continued from previous page*

Name	**RA**	**Dec**	M_B	M_V	**D**	**References**
dw1337-41	13:37:55.0	-41:54:11.0	-8.85	999.0	3.6	9
dw1343-34	13:43:49.0	-34:56:7.0	-8.4	999.0	4.9	9
dw1357-28	13:57:0.0	-28:55:15.0	-8.87	999.0	4.9	9
dw1401-32	14:01:25.0	-32:37:46.0	-9.81	999.0	4.9	9
dw1403-33	14:03:18.0	-33:24:14.0	-9.5	999.0	4.9	9
dw1406-29	14:06:41.0	-29:08:10.0	-9.79	999.0	4.9	9
dw1409-33	14:09:3.0	-33:49:40.0	-9.81	999.0	4.9	9
dw1410-34	14:10:47.0	-34:52:7.0	-10.71	999.0	4.9	9
dw1413-34	14:13:8.0	-34:23:33.0	-8.28	999.0	4.9	9
dw1415-32	14:15:41.0	-32:34:21.0	-9.58	999.0	4.9	9
dw1318-44	13:18:58.0	-44:53:41.0	-7.88	999.0	4.9	9
dw1323-40c	13:23:47.0	-40:43:17.0	-10.2	999.0	4.9	9
dw1331-37	13:31:32.0	-37:03:29.0	-9.38	999.0	4.9	9
dw1337-44	13:37:34.0	-44:13:7.0	-9.65	999.0	4.9	9
dw1315-45	13:15:56.0	-45:45:2.0	-10.44	999.0	4.9	8
dw1335-33	13:35:25.0	-33:18:0.0	-11.33	999.0	4.9	8
dw1334-32	13:34:5.0	-32:06:28.0	-10.47	999.0	4.9	8
dw1312-4246	13:12:10.18	-42:46:48.53	999.0	-9.37	999.0	11
dw1312-4244	13:12:10.93	-42:44:43.66	999.0	-8.12	999.0	11

Continued on next page

Table A.1 – *Continued from previous page*

Name	**RA**	**Dec**	M_B	M_V	**D**	**References**
dw1313-4218	13:12:22.48	-42:46:41.58	999.0	-7.54	999.0	11
dw1313-4246	13:12:42.87	-42:46:50.57	999.0	-7.95	999.0	11
dw1313-4211	13:13:34.28	-42:11:8.38	999.0	-9.79	999.0	11
dw1313-4214	13:13:34.4	-42:14:8.11	999.0	-9.58	999.0	11
dw1314-4204	13:14:8.17	-42:04:8.51	999.0	-9.11	999.0	11
dw1314-4230	13:14:21.93	-42:30:41.87	999.0	-8.96	999.0	11
dw1314-4142	13:14:44.82	-41:42:28.27	999.0	-7.74	999.0	11
dw1315-4232	13:15:2.98	-42:32:17.78	999.0	-8.91	999.0	11
dw1315-4309	13:15:33.97	-43:09:27.18	999.0	-7.42	999.0	11
dw1316-4224	13:16:42.27	-42:24:5.32	999.0	-10.32	999.0	11
dw1317-4255	13:17:48.49	-42:55:40.45	999.0	-8.46	999.0	11
dw1318-4233	13:18:5.59	-42:33:37.1	999.0	-9.14	999.0	11
dw1319-4203	13:19:21.26	-42:03:38.74	999.0	-9.15	999.0	11

Bibliography

T. M. C. Abbott, F. B. Abdalla, A. Alarcon, J. Aleksić, S. Allam, S. Allen, A. Amara, J. Annis, J. Asorey, S. Avila, D. Bacon, E. Balbinot, M. Banerji, N. Banik, W. Barkhouse, M. Baumer, E. Baxter, K. Bechtol, M. R. Becker, A. Benoit-Lévy, B. A. Benson, G. M. Bernstein, E. Bertin, J. Blazek, S. L. Bridle, D. Brooks, D. Brout, E. Buckley-Geer, D. L. Burke, M. T. Busha, A. Campos, D. Capozzi, A. Carnero Rosell, M. Carrasco Kind, J. Carretero, F. J. Castander, R. Cawthon, C. Chang, N. Chen, M. Childress, A. Choi, C. Conselice, R. Crittenden, M. Crocce, C. E. Cunha, C. B. D'Andrea, L. N. da Costa, R. Das, T. M. Davis, C. Davis, J. De Vicente, D. L. DePoy, J. DeRose, S. Desai, H. T. Diehl, J. P. Dietrich, S. Dodelson, P. Doel, A. Drlica-Wagner, T. F. Eifler, A. E. Elliott, F. Elsner, J. Elvin-Poole, J. Estrada, A. E. Evrard, Y. Fang, E. Fernandez, A. Ferté, D. A. Finley, B. Flaugher, P. Fosalba, O. Friedrich, J. Frieman, J. García-Bellido, M. Garcia-Fernandez, M. Gatti, E. Gaztanaga, D. W. Gerdes, T. Giannantonio, M. S. S. Gill, K. Glazebrook, D. A. Goldstein, D. Gruen, R. A. Gruendl, J. Gschwend, G. Gutierrez, S. Hamilton, W. G. Hartley, S. R. Hinton, K. Honscheid, B. Hoyle, D. Huterer, B. Jain, D. J. James, M. Jarvis, T. Jeltema, M. D. Johnson, M. W. G. Johnson, T. Kacprzak, S. Kent, A. G. Kim, A. King, D. Kirk, N. Kokron, A. Kovacs, E. Krause, C. Krawiec, A. Kremin, K. Kuehn, S. Kuhlmann, N. Kuropatkin, F. Lacasa, O. Lahav, T. S. Li, A. R. Liddle, C. Lidman, M. Lima, H. Lin, N. MacCrann, M. A. G. Maia, M. Makler, M. Manera, M. March, J. L. Marshall, P. Martini, R. G. McMahon, P. Melchior, F. Menanteau, R. Miquel, V. Miranda, D. Mudd, J. Muir, A. Möller, E. Neilsen, R. C. Nichol, B. Nord, P. Nugent, R. L. C. Ogando, A. Palmese, J. Peacock, H. V. Peiris, J. Peoples, W. J. Percival, D. Petravick, A. A. Plazas, A. Porredon, J. Prat, A. Pujol, M. M. Rau, A. Refregier, P. M. Ricker, N. Roe, R. P. Rollins, A. K. Romer, A. Roodman, R. Rosenfeld, A. J. Ross, E. Rozo, E. S. Rykoff, M. Sako, A. I. Salvador, S. Samuroff, C. Sánchez, E. Sanchez, B. Santiago, V. Scarpine, R. Schindler, D. Scolnic, L. F. Secco, S. Serrano, I. Sevilla-Noarbe, E. Sheldon, R. C. Smith, M. Smith, J. Smith, M. Soares-Santos, F. Sobreira, E. Suchyta, G. Tarle, D. Thomas, M. A. Troxel, D. L. Tucker, B. E. Tucker, S. A. Uddin, T. N. Varga, P. Vielzeuf, V. Vikram, A. K. Vivas, A. R. Walker, M. Wang, R. H. Wechsler, J. Weller, W. Wester, R. C. Wolf, B. Yanny, F. Yuan, A. Zenteno, B. Zhang, Y. Zhang, J. Zuntz, and Dark Energy Survey Collaboration. Dark Energy Survey year 1 results: Cosmological constraints from galaxy clustering and weak lensing. , 98(4): 043526, Aug. 2018. doi: 10.1103/PhysRevD.98.043526.

D. S. Aguado, R. Ahumada, A. Almeida, S. F. Anderson, B. H. Andrews, B. Anguiano, E. Aquino Ortíz, A. Aragón-Salamanca, M. Argudo-Fernández, M. Aubert, V. Avila-

Reese, C. Badenes, S. r. Barboza Rembold, K. Barger, J. Barrera-Ballesteros, D. Bates, J. Bautista, R. L. Beaton, T. C. Beers, F. Belfiore, M. Bernardi, M. Bershady, F. Beutler, J. Bird, D. Bizyaev, G. A. Blanc, M. R. Blanton, M. Blomqvist, A. S. Bolton, M. Boquien, J. Borissova, J. Bovy, W. N. Brand t, J. Brinkmann, J. R. Brownstein, K. Bundy, A. Burgasser, N. Byler, M. Cano Diaz, M. Cappellari, R. Carrera, B. Cervantes Sodi, Y. Chen, B. Cherinka, P. D. Choi, H. Chung, D. Coffey, J. M. Comerford, J. Comparat, K. Covey, G. da Silva Ilha, L. da Costa, Y. S. Dai, G. Damke, J. Darling, R. Davies, K. Dawson, V. de Sainte Agathe, A. Deconto Machado, A. Del Moro, N. De Lee, A. M. Diamond-Stanic, H. Domínguez Sánchez, J. Donor, N. Drory, H. du Mas des Bourboux, C. Duckworth, T. Dwelly, G. Ebelke, E. Emsellem, S. Escoffier, J. G. Fernández-Trincado, D. Feuillet, J.-L. Fischer, S. W. Fleming, A. Fraser-McKelvie, G. Freischlad, P. M. Frinchaboy, H. Fu, L. Galbany, R. Garcia-Dias, D. A. García-Hernández, L. A. Garma Oehmichen, M. A. Geimba Maia, H. Gil-Marín, K. Grabowski, M. Gu, H. Guo, J. Ha, E. Harrington, S. Hasselquist, C. R. Hayes, F. Hearty, H. Hernandez Toledo, H. Hicks, D. W. Hogg, K. Holley-Bockelmann, J. A. Holtzman, B.-C. Hsieh, J. A. S. Hunt, H. S. Hwang, H. J. Ibarra-Medel, C. E. Jimenez Angel, J. Johnson, A. Jones, H. Jönsson, K. Kinemuchi, J. Kollmeier, C. Krawczyk, K. Kreckel, S. Kruk, I. Lacerna, T.-W. Lan, R. R. Lane, D. R. Law, Y.-B. Lee, C. Li, J. Lian, L. Lin, Y.-T. Lin, C. Lintott, D. Long, P. Longa-Peña, J. T. Mackereth, A. de la Macorra, S. R. Majewski, O. Malanushenko, A. Manchado, C. Maraston, V. Mariappan, M. Marinelli, R. Marques-Chaves, T. Masseron, K. L. Masters, R. M. McDermid, N. Medina Peña, S. Meneses-Goytia, A. Merloni, M. Merrifield, S. Meszaros, D. Minniti, R. Minsley, D. Muna, A. D. Myers, P. Nair, J. Correa do Nascimento, J. A. Newman, C. Nitschelm, M. D. Olmstead, A. Oravetz, D. Oravetz, R. A. Ortega Minakata, Z. Pace, N. Padilla, P. A. Palicio, K. Pan, H.-A. Pan, T. Parikh, I. Parker, James, S. Peirani, S. Penny, W. J. Percival, I. Perez-Fournon, T. Peterken, M. H. Pinsonneault, A. Prakash, M. J. Raddick, A. Raichoor, R. A. Riffel, R. Riffel, H.-W. Rix, A. C. Robin, A. Roman-Lopes, B. Rose, A. J. Ross, G. Rossi, K. Rowlands, K. H. R. Rubin, S. F. Sánchez, J. R. Sánchez-Gallego, C. Sayres, A. Schaefer, R. P. Schiavon, J. S. Schimoia, E. Schlafly, D. Schlegel, D. P. Schneider, M. Schultheis, H.-J. Seo, S. J. Shamsi, Z. Shao, S. Shen, S. Shetty, G. Simonian, R. J. Smethurst, J. Sobeck, B. J. Souter, A. Spindler, D. V. Stark, K. G. Stassun, M. Steinmetz, T. Storchi-Bergmann, G. S. Stringfellow, G. Suárez, J. Sun, M. Taghizadeh-Popp, M. S. Talbot, J. Tayar, A. R. Thakar, D. Thomas, P. Tissera, R. Tojeiro, N. W. Troup, E. Unda-Sanzana, O. Valenzuela, M. Vargas-Magaña, J. A. Vázquez-Mata, D. Wake, B. A. Weaver, A.-M. Weijmans, K. B. Westfall, V. Wild, J. Wilson, E. Woods, R. Yan, M. Yang, O. Zamora, G. Zasowski, K. Zhang, Z. Zheng, Z. Zheng, G. Zhu, J. C. Zinn, and H. Zou. The Fifteenth Data Release of the Sloan Digital Sky Surveys: First Release of MaNGA-derived Quantities, Data Visualization Tools, and Stellar Library. , 240(2): 23, Feb. 2019. doi: 10.3847/1538-4365/aaf651.

H. B. Akins, C. R. Christensen, A. M. Brooks, F. Munshi, E. Applebaum, A. Engelhardt, and L. Chamberland. Quenching Timescales of Dwarf Satellites around Milky Way-mass Hosts. *The Astrophysical Journal*, 909(2):139, Mar. 2021. doi: 10.3847/1538-4357/abe2ab.

F. D. Albareti, C. Allende Prieto, A. Almeida, F. Anders, S. Anderson, B. H. Andrews, A. Aragón-Salamanca, M. Argudo-Fernández, E. Armengaud, E. Aubourg, V. Avila-Reese, C. Badenes, S. Bailey, B. Barbuy, K. Barger, J. Barrera-Ballesteros, C. Bartosz, S. Basu, D. Bates, G. Battaglia, F. Baumgarten, J. Baur, J. Bautista, T. C. Beers, F. Belfiore, M. Bershady, S. Bertran de Lis, J. C. Bird, D. Bizyaev, G. A. Blanc, M. Blanton, M. Blomqvist, A. S. Bolton, J. Borissova, J. Bovy, W. N. Brand t, J. Brinkmann, J. R. Brownstein, K. Bundy, E. Burtin, N. G. Busca, H. Orlando Camacho Chavez, M. Cano Díaz, M. Cappellari, R. Carrera, Y. Chen, B. Cherinka, E. Cheung, C. Chiappini, D. Chojnowski, C.-H. Chuang, H. Chung, R. F. Cirolini, N. Clerc, R. E. Cohen, J. M. Comerford, J. Comparat, J. Correa do Nascimento, M.-C. Cousinou, K. Covey, J. D. Crane, R. Croft, K. Cunha, J. Darling, J. Davidson, James W., K. Dawson, L. Da Costa, G. Da Silva Ilha, A. Deconto Machado, T. Delubac, N. De Lee, A. De la Macorra, S. De la Torre, A. M. Diamond-Stanic, J. Donor, J. J. Downes, N. Drory, C. Du, H. Du Mas des Bourboux, T. Dwelly, G. Ebelke, A. Eigenbrot, D. J. Eisenstein, Y. P. Elsworth, E. Emsellem, M. Eracleous, S. Escoffier, M. L. Evans, J. Falcón-Barroso, X. Fan, G. Favole, E. Fernandez-Alvar, J. G. Fernand ez-Trincado, D. Feuillet, S. W. Fleming, A. Font-Ribera, G. Freischlad, P. Frinchaboy, H. Fu, Y. Gao, R. A. Garcia, R. Garcia-Dias, D. A. Garcia-Hernández, A. E. Garcia Pérez, P. Gaulme, J. Ge, D. Geisler, B. Gillespie, H. Gil Marin, L. Girardi, D. Goddard, Y. Gomez Maqueo Chew, V. Gonzalez-Perez, K. Grabowski, P. Green, C. J. Grier, T. Grier, H. Guo, J. Guy, A. Hagen, M. Hall, P. Harding, R. E. Harley, S. Hasselquist, S. Hawley, C. R. Hayes, F. Hearty, S. Hekker, H. Hernandez Toledo, S. Ho, D. W. Hogg, K. Holley-Bockelmann, J. A. Holtzman, P. H. Holzer, J. Hu, D. Huber, T. A. Hutchinson, H. S. Hwang, H. J. Ibarra-Medel, I. I. Ivans, K. Ivory, K. Jaehnig, T. W. Jensen, J. A. Johnson, A. Jones, E. Jullo, T. Kallinger, K. Kinemuchi, D. Kirkby, M. Klaene, J.-P. Kneib, J. A. Kollmeier, I. Lacerna, R. R. Lane, D. Lang, P. Laurent, D. R. Law, A. Leauthaud, J.-M. Le Goff, C. Li, C. Li, N. Li, R. Li, F.-H. Liang, Y. Liang, M. Lima, L. Lin, L. Lin, Y.-T. Lin, C. Liu, D. Long, S. Lucatello, N. MacDonald, C. L. MacLeod, J. T. Mackereth, S. Mahadevan, M. A. G. Maia, R. Maiolino, S. R. Majewski, O. Malanushenko, V. Malanushenko, N. D. Mallmann, A. Manchado, C. Maraston, R. Marques-Chaves, I. Martinez Valpuesta, K. L. Masters, S. Mathur, I. D. McGreer, A. Merloni, M. R. Merrifield, S. Mészáros, A. Meza, A. Miglio, I. Minchev, K. Molaverdikhani, A. D. Montero-Dorta, B. Mosser, D. Muna, A. Myers, P. Nair, K. Nandra, M. Ness, J. A. Newman, R. C. Nichol, D. L. Nidever, C. Nitschelm, J. O'Connell, A. Oravetz, D. J. Oravetz, Z. Pace, N. Padilla, N. Palanque-Delabrouille, K. Pan, J. Parejko, I. Paris, C. Park, J. A. Peacock, S. Peirani, M. Pellejero-Ibanez, S. Penny, W. J. Percival, J. W. Percival, I. Perez-Fournon, P. Petitjean, M. Pieri, M. H. Pinsonneault, A. Pisani, F. Prada, A. Prakash, N. Price-Jones, M. J. Raddick, M. Rahman, A. Raichoor, S. Barboza Rembold, A. M. Reyna, J. Rich, H. Richstein, J. Ridl, R. A. Riffel, R. Riffel, H.-W. Rix, A. C. Robin, C. M. Rockosi, S. Rodríguez-Torres, T. S. Rodrigues, N. Roe, A. Roman Lopes, C. Román-Zúñiga, A. J. Ross, G. Rossi, J. Ruan, R. Ruggeri, J. C. Runnoe, S. Salazar-Albornoz, M. Salvato, S. F. Sanchez, A. G. Sanchez, J. R. Sanchez-Gallego, B. X. Santiago, R. Schiavon, J. S. Schimoia, E. Schlafly, D. J. Schlegel, D. P. Schneider, R. Schönrich, M. Schultheis, A. Schwope, H.-J. Seo, A. Serenelli, B. Sesar, Z. Shao, M. Shetrone, M. Shull, V. Silva Aguirre, M. F.

Skrutskie, A. Slosar, M. Smith, V. V. Smith, J. Sobeck, G. Somers, D. Souto, D. V. Stark, K. G. Stassun, M. Steinmetz, D. Stello, T. Storchi Bergmann, M. A. Strauss, A. Streblyanska, G. S. Stringfellow, G. Suarez, J. Sun, M. Taghizadeh-Popp, B. Tang, C. Tao, J. Tayar, M. Tembe, D. Thomas, J. Tinker, R. Tojeiro, C. Tremonti, N. Troup, J. R. Trump, E. Unda-Sanzana, O. Valenzuela, R. Van den Bosch, M. Vargas-Magaña, J. A. Vazquez, S. Villanova, M. Vivek, N. Vogt, D. Wake, R. Walterbos, Y. Wang, E. Wang, B. A. Weaver, A.-M. Weijmans, D. H. Weinberg, K. B. Westfall, D. G. Whelan, E. Wilcots, V. Wild, R. A. Williams, J. Wilson, W. M. Wood-Vasey, D. Wylezalek, T. Xiao, R. Yan, M. Yang, J. E. Ybarra, C. Yeche, F.-T. Yuan, N. Zakamska, O. Zamora, G. Zasowski, K. Zhang, C. Zhao, G.-B. Zhao, Z. Zheng, Z. Zheng, Z.-M. Zhou, G. Zhu, J. C. Zinn, and H. Zou. The 13th Data Release of the Sloan Digital Sky Survey: First Spectroscopic Data from the SDSS-IV Survey Mapping Nearby Galaxies at Apache Point Observatory. , 233(2):25, Dec. 2017. doi: 10.3847/1538-4365/aa8992.

L. G. Althaus, E. García-Berro, I. Renedo, J. Isern, A. H. Córsico, and R. D. Rohrmann. EVOLUTION OF WHITE DWARF STARS WITH HIGH-METALLICITY PROGENITORS: THE ROLE OF22ne DIFFUSION. *The Astrophysical Journal*, 719(1):612–621, jul 2010. doi: 10.1088/0004-637x/719/1/612. URL `https://doi.org/10.1088%2F0004-637x%2F719%2F1%2F612`.

M. A. Alvarez, M. Busha, T. Abel, and R. H. Wechsler. Connecting Reionization to the Local Universe. , 703(2):L167–L171, Oct. 2009. doi: 10.1088/0004-637X/703/2/L167.

E. Applebaum, A. M. Brooks, C. R. Christensen, F. Munshi, T. R. Quinn, S. Shen, and M. Tremmel. Ultrafaint Dwarfs in a Milky Way Context: Introducing the Mint Condition DC Justice League Simulations. *The Astrophysical Journal*, 906(2):96, Jan. 2021. doi: 10.3847/1538-4357/abcafa.

D. Aubert, N. Deparis, P. Ocvirk, P. R. Shapiro, I. T. Iliev, G. Yepes, S. Gottlöber, Y. Hoffman, and R. Teyssier. The Inhomogeneous Reionization Times of Present-day Galaxies. , 856(2):L22, Apr. 2018. doi: 10.3847/2041-8213/aab14d.

I. K. Baldry, S. P. Driver, J. Loveday, E. N. Taylor, L. S. Kelvin, J. Liske, P. Norberg, A. S. G. Robotham, S. Brough, A. M. Hopkins, S. P. Bamford, J. A. Peacock, J. Bland-Hawthorn, C. J. Conselice, S. M. Croom, D. H. Jones, H. R. Parkinson, C. C. Popescu, M. Prescott, R. G. Sharp, and R. J. Tuffs. Galaxy And Mass Assembly (GAMA): the galaxy stellar mass function at z ¡ 0.06. , 421(1):621–634, Mar. 2012. doi: 10.1111/j.1365-2966.2012.20340.x.

P. Behroozi, R. H. Wechsler, A. P. Hearin, and C. Conroy. UNIVERSEMACHINE: The correlation between galaxy growth and dark matter halo assembly from z = 0-10. , 488(3):3143–3194, Sept. 2019. doi: 10.1093/mnras/stz1182.

P. S. Behroozi, R. H. Wechsler, and H.-Y. Wu. The ROCKSTAR Phase-space Temporal Halo Finder and the Velocity Offsets of Cluster Cores. *The Astrophysical Journal*, 762 (2):109, Jan. 2013a. doi: 10.1088/0004-637X/762/2/109.

P. S. Behroozi, R. H. Wechsler, H.-Y. Wu, M. T. Busha, A. A. Klypin, and J. R. Primack. Gravitationally Consistent Halo Catalogs and Merger Trees for Precision Cosmology. *The Astrophysical Journal*, 763(1):18, Jan. 2013b. doi: 10.1088/0004-637X/763/1/18.

V. Belokurov, D. B. Zucker, N. W. Evans, M. I. Wilkinson, M. J. Irwin, S. Hodgkin, D. M. Bramich, J. M. Irwin, G. Gilmore, B. Willman, S. Vidrih, H. J. Newberg, R. F. G. Wyse, M. Fellhauer, P. C. Hewett, N. Cole, E. F. Bell, T. C. Beers, C. M. Rockosi, B. Yanny, E. K. Grebel, D. P. Schneider, R. Lupton, J. C. Barentine, H. Brewington, J. Brinkmann, M. Harvanek, S. J. Kleinman, J. Krzesinski, D. Long, A. Nitta, J. A. Smith, and S. A. Snedden. A Faint New Milky Way Satellite in Bootes. , 647(2): L111–L114, Aug. 2006. doi: 10.1086/507324.

V. Belokurov, D. B. Zucker, N. W. Evans, J. T. Kleyna, S. Koposov, S. T. Hodgkin, M. J. Irwin, G. Gilmore, M. I. Wilkinson, M. Fellhauer, D. M. Bramich, P. C. Hewett, S. Vidrih, J. T. A. De Jong, J. A. Smith, H. W. Rix, E. F. Bell, R. F. G. Wyse, H. J. Newberg, P. A. Mayeur, B. Yanny, C. M. Rockosi, O. Y. Gnedin, D. P. Schneider, T. C. Beers, J. C. Barentine, H. Brewington, J. Brinkmann, M. Harvanek, S. J. Kleinman, J. Krzesinski, D. Long, A. Nitta, and S. A. Snedden. Cats and Dogs, Hair and a Hero: A Quintet of New Milky Way Companions. *The Astrophysical Journal*, 654(2): 897–906, Jan. 2007a. doi: 10.1086/509718.

V. Belokurov, D. B. Zucker, N. W. Evans, J. T. Kleyna, S. Koposov, S. T. Hodgkin, M. J. Irwin, G. Gilmore, M. I. Wilkinson, M. Fellhauer, D. M. Bramich, P. C. Hewett, S. Vidrih, J. T. A. De Jong, J. A. Smith, H. W. Rix, E. F. Bell, R. F. G. Wyse, H. J. Newberg, P. A. Mayeur, B. Yanny, C. M. Rockosi, O. Y. Gnedin, D. P. Schneider, T. C. Beers, J. C. Barentine, H. Brewington, J. Brinkmann, M. Harvanek, S. J. Kleinman, J. Krzesinski, D. Long, A. Nitta, and S. A. Snedden. Cats and Dogs, Hair and a Hero: A Quintet of New Milky Way Companions. *The Astrophysical Journal*, 654(2): 897–906, Jan. 2007b. doi: 10.1086/509718.

A. Benítez-Llambay, J. F. Navarro, C. S. Frenk, T. Sawala, K. Oman, A. Fattahi, M. Schaller, J. Schaye, R. A. Crain, and T. Theuns. The properties of 'dark' ΛCDM haloes in the Local Group. , 465(4):3913–3926, Mar. 2017. doi: 10.1093/mnras/stw2982.

C. L. Bennett, D. Larson, J. L. Weiland, N. Jarosik, G. Hinshaw, N. Odegard, K. M. Smith, R. S. Hill, B. Gold, M. Halpern, E. Komatsu, M. R. Nolta, L. Page, D. N. Spergel, E. Wollack, J. Dunkley, A. Kogut, M. Limon, S. S. Meyer, G. S. Tucker, and E. L. Wright. Nine-year Wilkinson Microwave Anisotropy Probe (WMAP) Observations: Final Maps and Results. , 208(2):20, Oct. 2013. doi: 10.1088/0067-0049/208/2/20.

A. J. Benson. GALACTICUS: A semi-analytic model of galaxy formation. , 17(2): 175–197, Feb. 2012. doi: 10.1016/j.newast.2011.07.004.

A. J. Benson. The mass function of unprocessed dark matter haloes and merger tree branching rates. , 467(3):3454–3466, May 2017a. doi: 10.1093/mnras/stx343.

A. J. Benson. Constraining the noise-free distribution of halo spin parameters. , 471(3): 2871–2881, Nov. 2017b. doi: 10.1093/mnras/stx1804.

A. J. Benson. The mass function of unprocessed dark matter haloes and merger tree branching rates. , 467(3):3454–3466, May 2017c. doi: 10.1093/mnras/stx343.

A. J. Benson and R. Bower. Galaxy formation spanning cosmic history. , 405(3):1573–1623, July 2010. doi: 10.1111/j.1365-2966.2010.16592.x.

A. J. Benson, C. G. Lacey, C. M. Baugh, S. Cole, and C. S. Frenk. The effects of photoionization on galaxy formation - I. Model and results at z=0. , 333(1):156–176, June 2002. doi: 10.1046/j.1365-8711.2002.05387.x.

G. Bertone, D. Hooper, and J. Silk. Particle dark matter: evidence, candidates and constraints. , 405(5-6):279–390, Jan. 2005. doi: 10.1016/j.physrep.2004.08.031.

Y. Birnboim and A. Dekel. Virial shocks in galactic haloes? , 345(1):349–364, Oct. 2003. doi: 10.1046/j.1365-8711.2003.06955.x.

G. A. Blanc, Y. Lu, A. Benson, A. Katsianis, and M. Barraza. A Characteristic Mass Scale in the Mass-Metallicity Relation of Galaxies. *The Astrophysical Journal*, 877(1): 6, May 2019. doi: 10.3847/1538-4357/ab16ec.

L. Blitz and E. Rosolowsky. The Role of Pressure in GMC Formation II: The H_2-Pressure Relation. *The Astrophysical Journal*, 650(2):933–944, Oct. 2006. doi: 10.1086/505417.

Á. Bogdán and A. D. Goulding. Connecting Dark Matter Halos with the Galaxy Center and the Supermassive Black Hole. *The Astrophysical Journal*, 800(2):124, Feb. 2015. doi: 10.1088/0004-637X/800/2/124.

S. Bose, A. J. Deason, V. Belokurov, and C. S. Frenk. The little things matter: relating the abundance of ultrafaint satellites to the hosts' assembly history. , 495(1):743–757, June 2020. doi: 10.1093/mnras/staa1199.

M. S. Bovill and M. Ricotti. Pre-reionization fossils, ultra-faint dwarfs, and the missing galactic satellite problem. *The Astrophysical Journal*, 693(2):1859, 2009.

M. S. Bovill and M. Ricotti. Pre-Reionization Fossils, Ultra-Faint Dwarfs, and the Missing Galactic Satellite Problem. *The Astrophysical Journal*, 693(2):1859–1870, Mar. 2009. doi: 10.1088/0004-637X/693/2/1859.

M. S. Bovill and M. Ricotti. Where are the Fossils of the First Galaxies? I. Local Volume Maps and Properties of the Undetected Dwarfs. *The Astrophysical Journal*, 741(1):17, Nov. 2011. doi: 10.1088/0004-637X/741/1/17.

M. S. Bovill, T. H. Puzia, M. Ricotti, and M. A. Taylor. The Lost Dwarfs of Centaurus A and the Formation of its Dark Globular Clusters. *The Astrophysical Journal*, 832 (1):88, Nov. 2016. doi: 10.3847/0004-637X/832/1/88.

R. G. Bower, I. Vernon, M. Goldstein, A. J. Benson, C. G. Lacey, C. M. Baugh, S. Cole, and C. S. Frenk. The parameter space of galaxy formation. , 407(4):2017–2045, Oct. 2010. doi: 10.1111/j.1365-2966.2010.16991.x.

M. Boylan-Kolchin, V. Springel, S. D. M. White, A. Jenkins, and G. Lemson. Resolving cosmic structure formation with the Millennium-II Simulation. , 398(3):1150–1164, Sept. 2009. doi: 10.1111/j.1365-2966.2009.15191.x.

V. Bromm, N. Yoshida, L. Hernquist, and C. F. McKee. The formation of the first stars and galaxies. , 459(7243):49–54, May 2009. doi: 10.1038/nature07990.

T. M. Brown, J. Tumlinson, M. Geha, E. N. Kirby, D. A. VandenBerg, R. R. Muñoz, J. S. Kalirai, J. D. Simon, R. J. Avila, P. Guhathakurta, A. Renzini, and H. C. Ferguson. The Primeval Populations of the Ultra-faint Dwarf Galaxies. , 753(1):L21, July 2012a. doi: 10.1088/2041-8205/753/1/L21.

T. M. Brown, J. Tumlinson, M. Geha, E. N. Kirby, D. A. VandenBerg, R. R. Muñoz, J. S. Kalirai, J. D. Simon, R. J. Avila, P. Guhathakurta, A. Renzini, and H. C. Ferguson. The Primeval Populations of the Ultra-faint Dwarf Galaxies. , 753(1):L21, July 2012b. doi: 10.1088/2041-8205/753/1/L21.

T. M. Brown, J. Tumlinson, M. Geha, J. D. Simon, L. C. Vargas, D. A. VandenBerg, E. N. Kirby, J. S. Kalirai, R. J. Avila, M. Gennaro, H. C. Ferguson, R. R. Muñoz, P. Guhathakurta, and A. Renzini. The Quenching of the Ultra-faint Dwarf Galaxies in the Reionization Era. *The Astrophysical Journal*, 796(2):91, Dec. 2014. doi: 10.1088/0004-637X/796/2/91.

G. L. Bryan and M. L. Norman. Statistical Properties of X-Ray Clusters: Analytic and Numerical Comparisons. *The Astrophysical Journal*, 495(1):80–99, Mar. 1998. doi: 10.1086/305262.

J. S. Bullock and K. V. Johnston. Tracing Galaxy Formation with Stellar Halos. I. Methods. *The Astrophysical Journal*, 635(2):931–949, Dec. 2005. doi: 10.1086/497422.

J. S. Bullock, A. V. Kravtsov, and D. H. Weinberg. Reionization and the Abundance of Galactic Satellites. *The Astrophysical Journal*, 539(2):517–521, Aug. 2000. doi: 10.1086/309279.

M. T. Busha, M. A. Alvarez, R. H. Wechsler, T. Abel, and L. E. Strigari. The Impact of Inhomogeneous Reionization on the Satellite Galaxy Population of the Milky Way. *The Astrophysical Journal*, 710(1):408–420, Feb. 2010. doi: 10.1088/0004-637X/710/1/408.

W. Cerny, C. E. Martínez-Vázquez, A. Drlica-Wagner, A. B. Pace, B. Mutlu-Pakdil, T. S. Li, A. H. Riley, D. Crnojević, C. R. Bom, J. A. Carballo-Bello, J. L. Carlin, A. Chiti, Y. Choi, M. L. M. Collins, E. Darragh-Ford, P. S. Ferguson, M. Geha, D. Martínez-Delgado, P. Massana, S. Mau, G. E. Medina, R. R. Muñoz, E. O. Nadler, K. A. G. Olsen, A. Pieres, J. D. Sakowska, J. D. Simon, G. S. Stringfellow, A. K. Vivas, A. R. Walker, and R. H. Wechsler. Six More Ultra-Faint Milky Way Companions

Discovered in the DECam Local Volume Exploration Survey. *arXiv e-prints*, art. arXiv:2209.12422, Sept. 2022. doi: 10.48550/arXiv.2209.12422.

K. Chamberlain, A. M. Price-Whelan, G. Besla, E. C. Cunningham, N. Garavito-Camargo, J. Peñarrubia, and M. S. Petersen. Implications of the Milky Way Travel Velocity for Dynamical Mass Estimates of the Local Group. *The Astrophysical Journal*, 942(1):18, Jan. 2023. doi: 10.3847/1538-4357/aca01f.

L.-H. Chen, M. Magg, T. Hartwig, S. C. O. Glover, A. P. Ji, and R. S. Klessen. Tracing stars in Milky Way satellites with A-SLOTH. , 513(1):934–950, June 2022. doi: 10.1093/mnras/stac933.

S. Cole, C. G. Lacey, C. M. Baugh, and C. S. Frenk. Hierarchical galaxy formation. , 319(1):168–204, Nov. 2000a. doi: 10.1046/j.1365-8711.2000.03879.x.

S. Cole, C. G. Lacey, C. M. Baugh, and C. S. Frenk. Hierarchical galaxy formation. , 319(1):168–204, Nov. 2000b. doi: 10.1046/j.1365-8711.2000.03879.x.

S. Cole, J. Helly, C. S. Frenk, and H. Parkinson. The statistical properties of Λ cold dark matter halo formation. , 383(2):546–556, Jan. 2008. doi: 10.1111/j.1365-2966.2007.12516.x.

M. Colless. *The 2dF Galaxy Redshift Survey*, page E5485. 2002. doi: 10.1888/0333750888/5485.

Colvin,A.Z. Local volume, 2020. URL `https://commons.wikimedia.org/w/index.php?curid=71065242`.

B. Côté, C. L. Fryer, K. Belczynski, O. Korobkin, M. Chruślińska, N. Vassh, M. R. Mumpower, J. Lippuner, T. M. Sprouse, R. Surman, and R. Wollaeger. The Origin of r-process Elements in the Milky Way. *The Astrophysical Journal*, 855(2):99, Mar. 2018. doi: 10.3847/1538-4357/aaad67.

S. Côté, A. Draginda, E. D. Skillman, and B. W. Miller. Star Formation in Dwarf Galaxies of the Nearby Centaurus a Group. , 138(4):1037–1061, Oct. 2009. doi: 10.1088/0004-6256/138/4/1037.

D. Crnojevic. The PISCeS survey: the extended stellar halos of nearby galaxies. In *American Astronomical Society Meeting Abstracts*, American Astronomical Society Meeting Abstracts, page 207.13, Jan. 2020.

D. Crnojević and B. Mutlu-Pakdil. Dwarf galaxies yesterday, now and tomorrow. *Nature Astronomy*, 5:1191–1194, Dec. 2021. doi: 10.1038/s41550-021-01563-1.

D. Crnojević, E. K. Grebel, and A. Koch. A close look at the Centaurus A group of galaxies. I. Metallicity distribution functions and population gradients in early-type dwarfs. , 516:A85, June 2010. doi: 10.1051/0004-6361/200913429.

D. Crnojević, E. K. Grebel, and A. A. Cole. A close look at the Centaurus A group of galaxies. III. Recent star formation histories of late-type dwarfs around M 83. , 530: A59, June 2011. doi: 10.1051/0004-6361/201015474.

D. Crnojević, E. K. Grebel, and A. A. Cole. A close look at the Centaurus A group of galaxies. IV. Recent star formation histories of late-type dwarfs around CenA. , 541: A131, May 2012. doi: 10.1051/0004-6361/201218898.

D. Crnojević, D. J. Sand, N. Caldwell, P. Guhathakurta, B. McLeod, A. Seth, J. D. Simon, J. Strader, and E. Toloba. Discovery of a Close Pair of Faint Dwarf Galaxies in the Halo of Centaurus A. , 795(2):L35, Nov. 2014. doi: 10.1088/2041-8205/795/2/L35.

D. Crnojevic, N. Caldwell, P. Guhathakurta, B. Mcleod, D. J. Sand, A. C. Seth, J. D. Simon, J. Strader, and E. Toloba. Resolving the faint end of the satellite luminosity function for the nearest elliptical Centaurus A. HST Proposal. Cycle 22, ID. #13856, Jan. 2016.

D. Crnojević, D. J. Sand, P. Bennet, S. Pasetto, K. Spekkens, N. Caldwell, P. Guhathakurta, B. McLeod, A. Seth, J. D. Simon, J. Strader, and E. Toloba. The Faint End of the Centaurus A Satellite Luminosity Function. , 872(1):80, Feb. 2019. doi: 10.3847/1538-4357/aafbe7.

N. Dalal, Y. Lithwick, and M. Kuhlen. The Origin of Dark Matter Halo Profiles. *arXiv e-prints*, art. arXiv:1010.2539, Oct. 2010.

G. de Vaucouleurs, A. de Vaucouleurs, J. Corwin, Herold G., R. J. Buta, G. Paturel, and P. Fouque. *Third Reference Catalogue of Bright Galaxies*. 1991.

A. Dekel and J. Silk. The Origin of Dwarf Galaxies, Cold Dark Matter, and Biased Galaxy Formation. *The Astrophysical Journal*, 303:39, Apr. 1986. doi: 10.1086/164050.

B. Diemer and A. V. Kravtsov. Dependence of the Outer Density Profiles of Halos on Their Mass Accretion Rate. *The Astrophysical Journal*, 789(1):1, July 2014. doi: 10.1088/0004-637X/789/1/1.

M. T. Doyle, M. J. Drinkwater, D. J. Rohde, K. A. Pimbblet, M. Read, M. J. Meyer, M. A. Zwaan, E. Ryan-Weber, J. Stevens, B. S. Koribalski, R. L. Webster, L. Staveley-Smith, D. G. Barnes, M. Howlett, V. A. Kilborn, M. Waugh, M. J. Pierce, R. Bhathal, W. J. G. de Blok, M. J. Disney, R. D. Ekers, K. C. Freeman, D. A. Garcia, B. K. Gibson, J. Harnett, P. A. Henning, H. Jerjen, M. J. Kesteven, P. M. Knezek, S. Mader, M. Marquarding, R. F. Minchin, J. O'Brien, T. Oosterloo, R. M. Price, M. E. Putman, S. D. Ryder, E. M. Sadler, I. M. Stewart, F. Stootman, and A. E. Wright. The HIPASS catalogue - III. Optical counterparts and isolated dark galaxies. , 361(1):34–44, July 2005. doi: 10.1111/j.1365-2966.2005.09159.x.

A. Drlica-Wagner, K. Bechtol, E. S. Rykoff, E. Luque, A. Queiroz, Y. Y. Mao, R. H. Wechsler, J. D. Simon, B. Santiago, B. Yanny, E. Balbinot, S. Dodelson, A. Fausti Neto, D. J. James, T. S. Li, M. A. G. Maia, J. L. Marshall, A. Pieres, K. Stringer, A. R.

Walker, T. M. C. Abbott, F. B. Abdalla, S. Allam, A. Benoit-Lévy, G. M. Bernstein, E. Bertin, D. Brooks, E. Buckley-Geer, D. L. Burke, A. Carnero Rosell, M. Carrasco Kind, J. Carretero, M. Crocce, L. N. da Costa, S. Desai, H. T. Diehl, J. P. Dietrich, P. Doel, T. F. Eifler, A. E. Evrard, D. A. Finley, B. Flaugher, P. Fosalba, J. Frieman, E. Gaztanaga, D. W. Gerdes, D. Gruen, R. A. Gruendl, G. Gutierrez, K. Honscheid, K. Kuehn, N. Kuropatkin, O. Lahav, P. Martini, R. Miquel, B. Nord, R. Ogando, A. A. Plazas, K. Reil, A. Roodman, M. Sako, E. Sanchez, V. Scarpine, M. Schubnell, I. Sevilla-Noarbe, R. C. Smith, M. Soares-Santos, F. Sobreira, E. Suchyta, M. E. C. Swanson, G. Tarle, D. Tucker, V. Vikram, W. Wester, Y. Zhang, J. Zuntz, and DES Collaboration. Eight Ultra-faint Galaxy Candidates Discovered in Year Two of the Dark Energy Survey. *The Astrophysical Journal*, 813(2):109, Nov. 2015. doi: 10.1088/0004-637X/813/2/109.

A. Drlica-Wagner, K. Bechtol, S. Allam, D. L. Tucker, R. A. Gruendl, M. D. Johnson, A. R. Walker, D. J. James, D. L. Nidever, K. A. G. Olsen, R. H. Wechsler, M. R. L. Cioni, B. C. Conn, K. Kuehn, T. S. Li, Y. Y. Mao, N. F. Martin, E. Neilsen, N. E. D. Noel, A. Pieres, J. D. Simon, G. S. Stringfellow, R. P. van der Marel, and B. Yanny. An Ultra-faint Galaxy Candidate Discovered in Early Data from the Magellanic Satellites Survey. , 833(1):L5, Dec. 2016. doi: 10.3847/2041-8205/833/1/L5.

A. Drlica-Wagner, K. Bechtol, S. Mau, M. McNanna, E. O. Nadler, A. B. Pace, T. S. Li, A. Pieres, E. Rozo, J. D. Simon, A. R. Walker, R. H. Wechsler, T. M. C. Abbott, S. Allam, J. Annis, E. Bertin, D. Brooks, D. L. Burke, A. C. Rosell, M. Carrasco Kind, J. Carretero, M. Costanzi, L. N. da Costa, J. De Vicente, S. Desai, H. T. Diehl, P. Doel, T. F. Eifler, S. Everett, B. Flaugher, J. Frieman, J. García-Bellido, E. Gaztanaga, D. Gruen, R. A. Gruendl, J. Gschwend, G. Gutierrez, K. Honscheid, D. J. James, E. Krause, K. Kuehn, N. Kuropatkin, O. Lahav, M. A. G. Maia, J. L. Marshall, P. Melchior, F. Menanteau, R. Miquel, A. Palmese, A. A. Plazas, E. Sanchez, V. Scarpine, M. Schubnell, S. Serrano, I. Sevilla-Noarbe, M. Smith, E. Suchyta, G. Tarle, and DES Collaboration. Milky Way Satellite Census. I. The Observational Selection Function for Milky Way Satellites in DES Y3 and Pan-STARRS DR1. *The Astrophysical Journal*, 893(1):47, Apr. 2020. doi: 10.3847/1538-4357/ab7eb9.

G. Efstathiou and M. J. Rees. High-redshift quasars in the Cold Dark Matter cosmogony. , 230:5p–11p, Feb. 1988. doi: 10.1093/mnras/230.1.5P.

G. Efstathiou, C. S. Frenk, S. D. M. White, and M. Davis. Gravitational clustering from scale-free initial conditions. , 235:715–748, Dec. 1988. doi: 10.1093/mnras/235.3.715.

P. Eigenthaler, T. H. Puzia, M. A. Taylor, Y. Ordenes-Briceño, R. P. Muñoz, K. X. Ribbeck, K. A. Alamo-Martínez, H. Zhang, S. Ángel, M. Capaccioli, P. Côté, L. Ferrarese, G. Galaz, E. K. Grebel, M. Hempel, M. Hilker, A. Lançon, S. Mieske, B. Miller, M. Paolillo, M. Powalka, T. Richtler, J. Roediger, Y. Rong, R. Sánchez-Janssen, and C. Spengler. The Next Generation Fornax Survey (NGFS). II. The Central Dwarf Galaxy Population. *The Astrophysical Journal*, 855(2):142, Mar. 2018. doi: 10.3847/1538-4357/aaab60.

X. Fan, C. L. Carilli, and B. Keating. Observational Constraints on Cosmic Reionization. , 44(1):415–462, Sept. 2006. doi: 10.1146/annurev.astro.44.051905.092514.

M. A. Fardal, N. Katz, J. P. Gardner, L. Hernquist, D. H. Weinberg, and R. Davé. Cooling Radiation and the Lyα Luminosity of Forming Galaxies. *The Astrophysical Journal*, 562(2):605–617, Dec. 2001. doi: 10.1086/323519.

L. Ferrarese, P. Côté, J.-C. Cuillandre, S. D. J. Gwyn, E. W. Peng, L. A. MacArthur, P.-A. Duc, A. Boselli, S. Mei, T. Erben, A. W. McConnachie, P. R. Durrell, J. C. Mihos, A. Jordán, A. Lançon, T. H. Puzia, E. Emsellem, M. L. Balogh, J. P. Blakeslee, L. van Waerbeke, R. Gavazzi, B. Vollmer, J. J. Kavelaars, D. Woods, N. M. Ball, S. Boissier, S. Courteau, E. Ferriere, G. Gavazzi, H. Hildebrandt, P. Hudelot, M. Huertas-Company, C. Liu, D. McLaughlin, Y. Mellier, M. Milkeraitis, D. Schade, C. Balkowski, F. Bournaud, R. G. Carlberg, S. C. Chapman, H. Hoekstra, C. Peng, M. Sawicki, L. Simard, J. E. Taylor, R. B. Tully, W. van Driel, C. D. Wilson, T. Burdullis, B. Mahoney, and N. Manset. The Next Generation Virgo Cluster Survey (NGVS). I. Introduction to the Survey. , 200(1):4, May 2012. doi: 10.1088/0067-0049/200/1/4.

A. Fitts, M. Boylan-Kolchin, O. D. Elbert, J. S. Bullock, P. F. Hopkins, J. Oñorbe, A. Wetzel, C. Wheeler, C.-A. Faucher-Giguère, D. Kereš, E. D. Skillman, and D. R. Weisz. fire in the field: simulating the threshold of galaxy formation. , 471(3):3547–3562, Nov. 2017. doi: 10.1093/mnras/stx1757.

A. S. Font, R. G. Bower, I. G. McCarthy, A. J. Benson, C. S. Frenk, J. C. Helly, C. G. Lacey, C. M. Baugh, and S. Cole. The colours of satellite galaxies in groups and clusters. , 389(4):1619–1629, Oct. 2008. doi: 10.1111/j.1365-2966.2008.13698.x.

A. S. Font, A. J. Benson, R. G. Bower, C. S. Frenk, A. Cooper, G. De Lucia, J. C. Helly, A. Helmi, Y. S. Li, I. G. McCarthy, J. F. Navarro, V. Springel, E. Starkenburg, J. Wang, and S. D. M. White. The population of Milky Way satellites in the Λ cold dark matter cosmology. , 417(2):1260–1279, Oct. 2011. doi: 10.1111/j.1365-2966.2011.19339.x.

A. Frebel, J. D. Simon, E. Kirby, M. Geha, and B. Willman. Extremely metal-poor stars in dwarf galaxies. In K. Cunha, M. Spite, and B. Barbuy, editors, *Chemical Abundances in the Universe: Connecting First Stars to Planets*, volume 265, pages 237–240, Mar. 2010. doi: 10.1017/S1743921310000633.

S. R. Furlanetto, S. P. Oh, and F. H. Briggs. Cosmology at low frequencies: The 21 cm transition and the high-redshift Universe. , 433(4-6):181–301, Oct. 2006. doi: 10.1016/j.physrep.2006.08.002.

L. Gao, J. F. Navarro, S. Cole, C. S. Frenk, S. D. M. White, V. Springel, A. Jenkins, and A. F. Neto. The redshift dependence of the structure of massive Λ cold dark matter haloes. , 387(2):536–544, June 2008. doi: 10.1111/j.1365-2966.2008.13277.x.

M. Geha, R. H. Wechsler, Y.-Y. Mao, E. J. Tollerud, B. Weiner, R. Bernstein, B. Hoyle, S. Marchi, P. J. Marshall, R. Muñoz, and Y. Lu. The SAGA Survey. I. Satellite Galaxy

Populations around Eight Milky Way Analogs. *The Astrophysical Journal*, 847(1):4, Sept. 2017. doi: 10.3847/1538-4357/aa8626.

Gerard Lemson & the Virgo Consortium. Halo and galaxy formation histories from the millennium simulation, 2020. URL `https://wwwmpa.mpa-garching.mpg.de/millennium/#PUBLICATIONS`.

N. Y. Gnedin. Effect of Reionization on Structure Formation in the Universe. *The Astrophysical Journal*, 542(2):535–541, Oct. 2000. doi: 10.1086/317042.

N. Y. Gnedin and A. V. Kravtsov. Fossils of Reionization in the Local Group. *The Astrophysical Journal*, 645(2):1054–1061, July 2006. doi: 10.1086/504404.

S. Gottloeber, Y. Hoffman, and G. Yepes. Constrained Local UniversE Simulations (CLUES). *arXiv e-prints*, art. arXiv:1005.2687, May 2010.

A. S. Graus, J. S. Bullock, T. Kelley, M. Boylan-Kolchin, S. Garrison-Kimmel, and Y. Qi. How low does it go? Too few Galactic satellites with standard reionization quenching. , 488(4):4585–4595, Oct. 2019. doi: 10.1093/mnras/stz1992.

M. L. P. Gunawardhana, A. M. Hopkins, J. Bland-Hawthorn, S. Brough, R. Sharp, J. Loveday, E. Taylor, D. H. Jones, M. A. Lara-López, A. E. Bauer, M. Colless, M. Owers, I. K. Baldry, A. R. López-Sánchez, C. Foster, S. Bamford, M. J. I. Brown, S. P. Driver, M. J. Drinkwater, J. Liske, M. Meyer, P. Norberg, A. S. G. Robotham, J. H. Y. Ching, M. E. Cluver, S. Croom, L. Kelvin, M. Prescott, O. Steele, D. Thomas, and L. Wang. Galaxy And Mass Assembly: evolution of the Hα luminosity function and star formation rate density up to z ¡ 0.35. , 433(4):2764–2789, Aug. 2013. doi: 10.1093/mnras/stt890.

Y. Guo, M. Rafelski, S. M. Faber, D. C. Koo, M. R. Krumholz, J. R. Trump, S. P. Willner, R. Amorín, G. Barro, E. F. Bell, J. P. Gardner, E. Gawiser, N. P. Hathi, A. M. Koekemoer, C. Pacifici, P. G. Pérez-González, S. Ravindranath, N. Reddy, H. I. Teplitz, and H. Yesuf. The Bursty Star Formation Histories of Low-mass Galaxies at 0.4 ¡ z ¡ 1 Revealed by Star Formation Rates Measured From Hβ and FUV. *The Astrophysical Journal*, 833(1):37, Dec. 2016. doi: 10.3847/1538-4357/833/1/37.

O. Hahn and T. Abel. Multi-scale initial conditions for cosmological simulations. , 415 (3):2101–2121, Aug. 2011. doi: 10.1111/j.1365-2966.2011.18820.x.

G. L. H. Harris, M. Rejkuba, and W. E. Harris. The Distance to NGC 5128 (Centaurus A). , 27(4):457–462, Oct. 2010. doi: 10.1071/AS09061.

W. E. Harris, G. L. Harris, and M. J. Hudson. Dark Matter Halos in Galaxies and Globular Cluster Populations. II. Metallicity and Morphology. *The Astrophysical Journal*, 806(1):36, June 2015a. doi: 10.1088/0004-637X/806/1/36.

W. E. Harris, G. L. Harris, and M. J. Hudson. Dark Matter Halos in Galaxies and Globular Cluster Populations. II. Metallicity and Morphology. *The Astrophysical Journal*, 806(1):36, June 2015b. doi: 10.1088/0004-637X/806/1/36.

S. Hatton, J. E. G. Devriendt, S. Ninin, F. R. Bouchet, B. Guiderdoni, and D. Vibert. GALICS- I. A hybrid N-body/semi-analytic model of hierarchical galaxy formation. , 343(1):75–106, July 2003. doi: 10.1046/j.1365-8711.2003.05589.x.

J. C. Helly, S. Cole, C. S. Frenk, C. M. Baugh, A. Benson, and C. Lacey. Galaxy formation using halo merger histories taken from N-body simulations. , 338(4):903–912, Feb. 2003. doi: 10.1046/j.1365-8711.2003.06151.x.

B. M. B. Henriques, P. A. Thomas, S. Oliver, and I. Roseboom. Monte Carlo Markov Chain parameter estimation in semi-analytic models of galaxy formation. , 396(1): 535–547, June 2009. doi: 10.1111/j.1365-2966.2009.14730.x.

C. Hernández-Aguayo, V. Springel, R. Pakmor, M. Barrera, F. Ferlito, S. D. M. White, L. Hernquist, B. Hadzhiyska, A. M. Delgado, R. Kannan, S. Bose, and C. Frenk. The MillenniumTNG Project: High-precision predictions for matter clustering and halo statistics. *arXiv e-prints*, art. arXiv:2210.10059, Oct. 2022. doi: 10.48550/arXiv.2210.10059.

C. R. Higgs and A. W. McConnachie. Solo dwarfs IV: comparing and contrasting satellite and isolated dwarf galaxies in the Local Group. , 506(2):2766–2779, Sept. 2021. doi: 10.1093/mnras/stab1754.

G. Hinshaw, D. Larson, E. Komatsu, D. N. Spergel, C. L. Bennett, J. Dunkley, M. R. Nolta, M. Halpern, R. S. Hill, N. Odegard, L. Page, K. M. Smith, J. L. Weiland, B. Gold, N. Jarosik, A. Kogut, M. Limon, S. S. Meyer, G. S. Tucker, E. Wollack, and E. L. Wright. Nine-year Wilkinson Microwave Anisotropy Probe (WMAP) Observations: Cosmological Parameter Results. , 208(2):19, Oct. 2013. doi: 10.1088/0067-0049/208/2/19.

H. Hoekstra, M. Bartelmann, H. Dahle, H. Israel, M. Limousin, and M. Meneghetti. Masses of Galaxy Clusters from Gravitational Lensing. , 177(1-4):75–118, Aug. 2013. doi: 10.1007/s11214-013-9978-5.

P. F. Hopkins, D. Kereš, J. Oñorbe, C.-A. Faucher-Giguère, E. Quataert, N. Murray, and J. S. Bullock. Galaxies on FIRE (Feedback In Realistic Environments): stellar feedback explains cosmologically inefficient star formation. , 445(1):581–603, Nov. 2014a. doi: 10.1093/mnras/stu1738.

P. F. Hopkins, D. Kereš, J. Oñorbe, C.-A. Faucher-Giguère, E. Quataert, N. Murray, and J. S. Bullock. Galaxies on FIRE (Feedback In Realistic Environments): stellar feedback explains cosmologically inefficient star formation. , 445(1):581–603, Nov. 2014b. doi: 10.1093/mnras/stu1738.

P. F. Hopkins, A. Wetzel, D. Kereš, C.-A. Faucher-Giguère, E. Quataert, M. Boylan-Kolchin, N. Murray, C. C. Hayward, S. Garrison-Kimmel, C. Hummels, R. Feldmann, P. Torrey, X. Ma, D. Anglés-Alcázar, K.-Y. Su, M. Orr, D. Schmitz, I. Escala, R. Sanderson, M. Y. Grudić, Z. Hafen, J.-H. Kim, A. Fitts, J. S. Bullock, C. Wheeler,

T. K. Chan, O. D. Elbert, and D. Narayanan. FIRE-2 simulations: physics versus numerics in galaxy formation. , 480(1):800–863, Oct. 2018a. doi: 10.1093/mnras/sty1690.

P. F. Hopkins, A. Wetzel, D. Kereš, C.-A. Faucher-Giguère, E. Quataert, M. Boylan-Kolchin, N. Murray, C. C. Hayward, S. Garrison-Kimmel, C. Hummels, R. Feldmann, P. Torrey, X. Ma, D. Anglés-Alcázar, K.-Y. Su, M. Orr, D. Schmitz, I. Escala, R. Sanderson, M. Y. Grudić, Z. Hafen, J.-H. Kim, A. Fitts, J. S. Bullock, C. Wheeler, T. K. Chan, O. D. Elbert, and D. Narayanan. FIRE-2 simulations: physics versus numerics in galaxy formation. , 480(1):800–863, Oct. 2018b. doi: 10.1093/mnras/sty1690.

I. T. Iliev, B. Moore, S. Gottlöber, G. Yepes, Y. Hoffman, and G. Mellema. Reionization of the Local Group of galaxies. , 413(3):2093–2102, May 2011. doi: 10.1111/j.1365-2966.2011.18292.x.

M. J. Irwin, V. Belokurov, N. W. Evans, E. V. Ryan-Weber, J. T. A. de Jong, S. Koposov, D. B. Zucker, S. T. Hodgkin, G. Gilmore, P. Prema, L. Hebb, A. Begum, M. Fellhauer, P. C. Hewett, J. Kennicutt, R. C., M. I. Wilkinson, D. M. Bramich, S. Vidrih, H. W. Rix, T. C. Beers, J. C. Barentine, H. Brewington, M. Harvanek, J. Krzesinski, D. Long, A. Nitta, and S. A. Snedden. Discovery of an Unusual Dwarf Galaxy in the Outskirts of the Milky Way. , 656(1):L13–L16, Feb. 2007. doi: 10.1086/512183.

R. A. Jackson, S. Kaviraj, G. Martin, J. E. G. Devriendt, A. Slyz, J. Silk, Y. Dubois, S. K. Yi, C. Pichon, M. Volonteri, H. Choi, T. Kimm, K. Kraljic, and S. Peirani. Dark matter-deficient dwarf galaxies form via tidal stripping of dark matter in interactions with massive companions. , 502(2):1785–1796, Apr. 2021. doi: 10.1093/mnras/stab093.

P. A. James, N. S. Shane, J. E. Beckman, A. Cardwell, C. A. Collins, J. Etherton, R. S. de Jong, K. Fathi, J. H. Knapen, R. F. Peletier, S. M. Percival, D. L. Pollacco, M. S. Seigar, S. Stedman, and I. A. Steele. The Hα galaxy survey. I. The galaxy sample, Hα narrow-band observations and star formation parameters for 334 galaxies. , 414:23–43, Jan. 2004. doi: 10.1051/0004-6361:20031568.

F. Jiang, A. Dekel, J. Freundlich, F. C. van den Bosch, S. B. Green, P. F. Hopkins, A. Benson, and X. Du. SatGen: a semi-analytical satellite galaxy generator - I. The model and its application to Local-Group satellite statistics. , 502(1):621–641, Mar. 2021. doi: 10.1093/mnras/staa4034.

H. D. Kang and M. Ricotti. Ghostly haloes in dwarf galaxies: constraints on the star formation efficiency before reionization. *Monthly Notices of the Royal Astronomical Society*, 488(2):2673–2688, 2019.

I. D. Karachentsev, M. E. Sharina, D. I. Makarov, A. E. Dolphin, E. K. Grebel, D. Geisler, P. Guhathakurta, P. W. Hodge, V. E. Karachentseva, A. Sarajedini, and P. Seitzer. The very local Hubble flow. , 389:812–824, July 2002. doi: 10.1051/0004-6361:20020649.

I. D. Karachentsev, D. I. Makarov, M. E. Sharina, A. E. Dolphin, E. K. Grebel, D. Geisler, P. Guhathakurta, P. W. Hodge, V. E. Karachentseva, A. Sarajedini, and P. Seitzer.

Local galaxy flows within 5 Mpc. , 398:479–491, Feb. 2003. doi: 10.1051/0004-6361:20021566.

I. D. Karachentsev, D. I. Makarov, and E. I. Kaisina. Updated Nearby Galaxy Catalog. , 145(4):101, Apr. 2013. doi: 10.1088/0004-6256/145/4/101.

V. E. Karachentseva and I. D. Karachentsev. A list of new nearby dwarf galaxy candidates. , 127:409–419, Feb. 1998. doi: 10.1051/aas:1998109.

V. E. Karachentseva, I. D. Karachentsev, and G. M. Richter. A list of nearby dwarf galaxies towards the Local Void in Hercules-Aquila. , 135:221–226, Mar. 1999. doi: 10.1051/aas:1999173.

G. Kauffmann, S. D. M. White, and B. Guiderdoni. The formation and evolution of galaxies within merging dark matter haloes. , 264:201–218, Sept. 1993. doi: 10.1093/mnras/264.1.201.

G. Kauffmann, J. M. Colberg, A. Diaferio, and S. D. M. White. Clustering of galaxies in a hierarchical universe - I. Methods and results at z=0. , 303(1):188–206, Feb. 1999. doi: 10.1046/j.1365-8711.1999.02202.x.

J. D. P. Kenney, M. Geha, P. Jáchym, H. H. Crowl, W. Dague, A. Chung, J. van Gorkom, and B. Vollmer. Transformation of a Virgo Cluster Dwarf Irregular Galaxy by Ram Pressure Stripping: IC3418 and Its Fireballs. *The Astrophysical Journal*, 780(2):119, Jan. 2014. doi: 10.1088/0004-637X/780/2/119.

J. Kennicutt, Robert C. The Global Schmidt Law in Star-forming Galaxies. *The Astrophysical Journal*, 498(2):541–552, May 1998. doi: 10.1086/305588.

D. Kereš, N. Katz, D. H. Weinberg, and R. Davé. How do galaxies get their gas? , 363 (1):2–28, Oct. 2005. doi: 10.1111/j.1365-2966.2005.09451.x.

D. Kereš, N. Katz, R. Davé, M. Fardal, and D. H. Weinberg. Galaxies in a simulated ΛCDM universe - II. Observable properties and constraints on feedback. , 396(4): 2332–2344, July 2009. doi: 10.1111/j.1365-2966.2009.14924.x.

J. T. Kleyna, M. I. Wilkinson, N. W. Evans, and G. Gilmore. First Clear Signature of an Extended Dark Matter Halo in the Draco Dwarf Spheroidal. , 563(2):L115–L118, Dec. 2001. doi: 10.1086/338603.

A. Klypin, A. V. Kravtsov, O. Valenzuela, and F. Prada. Where Are the Missing Galactic Satellites? *The Astrophysical Journal*, 522(1):82–92, Sept. 1999. doi: 10.1086/307643.

S. R. Knollmann and A. Knebe. AHF: Amiga's Halo Finder. , 182(2):608–624, June 2009. doi: 10.1088/0067-0049/182/2/608.

J. Kormendy and L. C. Ho. Coevolution (Or Not) of Supermassive Black Holes and Host Galaxies. , 51(1):511–653, Aug. 2013. doi: 10.1146/annurev-astro-082708-101811.

A. Lauberts and E. A. Valentijn. *The surface photometry catalogue of the ESO-Uppsala galaxies*. 1989.

A. Leauthaud, J. Tinker, K. Bundy, P. S. Behroozi, R. Massey, J. Rhodes, M. R. George, J.-P. Kneib, A. Benson, R. H. Wechsler, M. T. Busha, P. Capak, M. Cortês, O. Ilbert, A. M. Koekemoer, O. Le Fèvre, S. Lilly, H. J. McCracken, M. Salvato, T. Schrabback, N. Scoville, T. Smith, and J. E. Taylor. New Constraints on the Evolution of the Stellar-to-dark Matter Connection: A Combined Analysis of Galaxy-Galaxy Lensing, Clustering, and Stellar Mass Functions from z = 0.2 to z =1. *The Astrophysical Journal*, 744(2):159, Jan. 2012. doi: 10.1088/0004-637X/744/2/159.

T. Y. Li, M. A. Alvarez, R. H. Wechsler, and T. Abel. Reionization Histories of Milky Way Mass Halos. *The Astrophysical Journal*, 785(2):134, Apr. 2014. doi: 10.1088/0004-637X/785/2/134.

Y.-S. Li, G. De Lucia, and A. Helmi. On the nature of the Milky Way satellites. , 401 (3):2036–2052, Jan. 2010. doi: 10.1111/j.1365-2966.2009.15803.x.

Z.-Z. Li, D.-H. Zhao, Y. P. Jing, J. Han, and F.-Y. Dong. Orbital Distribution of Infalling Satellite Halos across Cosmic Time. *The Astrophysical Journal*, 905(2):177, Dec. 2020. doi: 10.3847/1538-4357/abc481.

E. L. Łokas. NGC 5128 as an Isotropic Rotator. , 680(2):L101, June 2008. doi: 10.1086/589943.

Y. Lu, G. A. Blanc, and A. Benson. An Analytical Model for Galaxy Metallicity: What do Metallicity Relations Tell Us about Star Formation and Outflow? *The Astrophysical Journal*, 808(2):129, Aug. 2015. doi: 10.1088/0004-637X/808/2/129.

Y. Lu, A. Benson, A. Wetzel, Y.-Y. Mao, S. Tonnesen, A. H. G. Peter, M. Boylan-Kolchin, and R. H. Wechsler. The Importance of Preventive Feedback: Inference from Observations of the Stellar Masses and Metallicities of Milky Way Dwarf Galaxies. *The Astrophysical Journal*, 846(1):66, Sept. 2017. doi: 10.3847/1538-4357/aa845e.

A. V. Macciò, X. Kang, F. Fontanot, R. S. Somerville, S. Koposov, and P. Monaco. Luminosity function and radial distribution of Milky Way satellites in a ΛCDM Universe. , 402(3):1995–2008, Mar. 2010. doi: 10.1111/j.1365-2966.2009.16031.x.

A. V. Macciò, J. Frings, T. Buck, C. Penzo, A. A. Dutton, M. Blank, and A. Obreja. The edge of galaxy formation - I. Formation and evolution of MW-satellite analogues before accretion. , 472(2):2356–2366, Dec. 2017. doi: 10.1093/mnras/stx2048.

L. Makarova, D. Makarov, A. Dolphin, I. Karachentsev, B. Tully, S. Sakai, E. Shaya, L. Rizzi, M. Sharina, and V. Karachentseva. Star Formation History of the Dwarf Galaxies in the Centaurus A Group. In F. Combes and J. Palouš, editors, *Galaxy Evolution across the Hubble Time*, volume 235, pages 320–320, May 2007. doi: 10.1017/S1743921306006855.

P. Mansfield and C. Avestruz. How biased are halo properties in cosmological simulations? , 500(3):3309–3328, Jan. 2021. doi: 10.1093/mnras/staa3388.

Y.-Y. Mao, M. Geha, R. H. Wechsler, B. Weiner, E. J. Tollerud, E. O. Nadler, and N. Kallivayalil. The SAGA Survey. II. Building a Statistical Sample of Satellite Systems around Milky Way-like Galaxies. *The Astrophysical Journal*, 907(2):85, Feb. 2021. doi: 10.3847/1538-4357/abce58.

F. Marinacci, M. Vogelsberger, R. Pakmor, P. Torrey, V. Springel, L. Hernquist, D. Nelson, R. Weinberger, A. Pillepich, J. Naiman, and S. Genel. First results from the IllustrisTNG simulations: radio haloes and magnetic fields. , 480(4):5113–5139, Nov. 2018. doi: 10.1093/mnras/sty2206.

A. M. Martin, E. Papastergis, R. Giovanelli, M. P. Haynes, C. M. Springob, and S. Stierwalt. The Arecibo Legacy Fast ALFA Survey. X. The H I Mass Function and Ω_H I from the 40% ALFALFA Survey. *The Astrophysical Journal*, 723(2):1359–1374, Nov. 2010. doi: 10.1088/0004-637X/723/2/1359.

N. F. Martin, R. A. Ibata, G. F. Lewis, A. McConnachie, A. Babul, N. F. Bate, E. Bernard, S. C. Chapman, M. M. L. Collins, A. R. Conn, D. Crnojević, M. A. Fardal, A. M. N. Ferguson, M. Irwin, A. D. Mackey, B. McMonigal, J. F. Navarro, and R. M. Rich. The PAndAS View of the Andromeda Satellite System. II. Detailed Properties of 23 M31 Dwarf Spheroidal Galaxies. *The Astrophysical Journal*, 833(2): 167, Dec. 2016. doi: 10.3847/1538-4357/833/2/167.

P. Massey, K. A. G. Olsen, P. W. Hodge, G. H. Jacoby, R. T. McNeill, R. C. Smith, and S. B. Strong. A Survey of Local Group Galaxies Currently Forming Stars. II. UBVRI Photometry of Stars in Seven Dwarfs and a Comparison of the Entire Sample. *The Astronomical Journal*, 133(5):2393–2417, May 2007. doi: 10.1086/513319.

M. Mateo, E. W. Olszewski, S. S. Vogt, and M. J. Keane. The Internal Kinematics of the Leo I Dwarf Spheroidal Galaxy: Dark Matter at the Fringe of the Milky Way. *The Astronomical Journal*, 116(5):2315–2327, Nov. 1998. doi: 10.1086/300618.

M. L. Mateo. Dwarf Galaxies of the Local Group. , 36:435–506, Jan. 1998. doi: 10.1146/annurev.astro.36.1.435.

A. W. McConnachie. The Observed Properties of Dwarf Galaxies in and around the Local Group. , 144(1):4, July 2012. doi: 10.1088/0004-6256/144/1/4.

A. J. Moffett, R. Lange, S. P. Driver, A. S. G. Robotham, L. S. Kelvin, M. Alpaslan, S. K. Andrews, J. Bland-Hawthorn, S. Brough, M. E. Cluver, M. Colless, L. J. M. Davies, B. W. Holwerda, A. M. Hopkins, P. R. Kafle, J. Liske, and M. Meyer. Galaxy and Mass Assembly (GAMA): the stellar mass budget of galaxy spheroids and discs. , 462(4):4336–4348, Nov. 2016. doi: 10.1093/mnras/stw1861.

P. Monaco, F. Fontanot, and G. Taffoni. The MORGANA model for the rise of galaxies and active nuclei. , 375(4):1189–1219, Mar. 2007. doi: 10.1111/j.1365-2966.2006.11253.x.

A. D. Montero-Dorta and F. Prada. The SDSS DR6 luminosity functions of galaxies. , 399(3):1106–1118, Nov. 2009. doi: 10.1111/j.1365-2966.2009.15197.x.

B. Moore, S. Ghigna, F. Governato, G. Lake, T. Quinn, J. Stadel, and P. Tozzi. Dark Matter Substructure within Galactic Halos. , 524(1):L19–L22, Oct. 1999. doi: 10.1086/312287.

M. F. Morales and J. S. B. Wyithe. Reionization and Cosmology with 21-cm Fluctuations. , 48:127–171, Sept. 2010. doi: 10.1146/annurev-astro-081309-130936.

S. More, F. C. van den Bosch, M. Cacciato, H. J. Mo, X. Yang, and R. Li. Satellite kinematics - II. The halo mass-luminosity relation of central galaxies in SDSS. , 392 (2):801–816, Jan. 2009. doi: 10.1111/j.1365-2966.2008.14095.x.

O. Müller, H. Jerjen, and B. Binggeli. New dwarf galaxy candidates in the Centaurus group. , 583:A79, Nov. 2015. doi: 10.1051/0004-6361/201526748.

O. Müller, H. Jerjen, and B. Binggeli. New low surface brightness dwarf galaxies in the Centaurus group. , 597:A7, Jan. 2017. doi: 10.1051/0004-6361/201628921.

O. Müller, M. Rejkuba, M. S. Pawlowski, R. Ibata, F. Lelli, M. Hilker, and H. Jerjen. The dwarf galaxy satellite system of Centaurus A. , 629:A18, Sept. 2019. doi: 10.1051/0004-6361/201935807.

O. Müller, K. Fahrion, M. Rejkuba, M. Hilker, F. Lelli, K. Lutz, M. S. Pawlowski, L. Coccato, G. S. Anand, and H. Jerjen. The properties of dwarf spheroidal galaxies in the Cen A group. Stellar populations, internal dynamics, and a heart-shaped Hα ring. , 645:A92, Jan. 2021. doi: 10.1051/0004-6361/202039359.

O. Müller, F. Lelli, B. Famaey, M. S. Pawlowski, K. Fahrion, M. Rejkuba, M. Hilker, and H. Jerjen. The Cen A galaxy group: Dynamical mass and missing baryons. , 662: A57, June 2022. doi: 10.1051/0004-6361/202142351.

F. Munshi, A. M. Brooks, E. Applebaum, D. R. Weisz, F. Governato, and T. R. Quinn. Going, going, gone dark: Quantifying the scatter in the faintest dwarf galaxies. *arXiv e-prints*, art. arXiv:1705.06286, May 2017.

A. Muzzin, D. Marchesini, M. Stefanon, M. Franx, H. J. McCracken, B. Milvang-Jensen, J. S. Dunlop, J. P. U. Fynbo, G. Brammer, I. Labbé, and P. G. van Dokkum. The Evolution of the Stellar Mass Functions of Star-forming and Quiescent Galaxies to z = 4 from the COSMOS/UltraVISTA Survey. *The Astrophysical Journal*, 777(1):18, Nov. 2013. doi: 10.1088/0004-637X/777/1/18.

E. O. Nadler, R. H. Wechsler, K. Bechtol, Y. Y. Mao, G. Green, A. Drlica-Wagner, M. McNanna, S. Mau, A. B. Pace, J. D. Simon, A. Kravtsov, S. Dodelson, T. S. Li, A. H. Riley, M. Y. Wang, T. M. C. Abbott, M. Aguena, S. Allam, J. Annis, S. Avila, G. M. Bernstein, E. Bertin, D. Brooks, D. L. Burke, A. C. Rosell, M. C. Kind, J. Carretero, M. Costanzi, L. N. da Costa, J. De Vicente, S. Desai, A. E.

Evrard, B. Flaugher, P. Fosalba, J. Frieman, J. García-Bellido, E. Gaztanaga, D. W. Gerdes, D. Gruen, J. Gschwend, G. Gutierrez, W. G. Hartley, S. R. Hinton, K. Honscheid, E. Krause, K. Kuehn, N. Kuropatkin, O. Lahav, M. A. G. Maia, J. L. Marshall, F. Menanteau, R. Miquel, A. Palmese, F. Paz-Chinchón, A. A. Plazas, A. K. Romer, E. Sanchez, B. Santiago, V. Scarpine, S. Serrano, M. Smith, M. Soares-Santos, E. Suchyta, G. Tarle, D. Thomas, T. N. Varga, A. R. Walker, and DES Collaboration. Milky Way Satellite Census. II. Galaxy-Halo Connection Constraints Including the Impact of the Large Magellanic Cloud. *The Astrophysical Journal*, 893(1):48, Apr. 2020. doi: 10.3847/1538-4357/ab846a.

J. P. Naiman, A. Pillepich, V. Springel, E. Ramirez-Ruiz, P. Torrey, M. Vogelsberger, R. Pakmor, D. Nelson, F. Marinacci, L. Hernquist, R. Weinberger, and S. Genel. First results from the IllustrisTNG simulations: a tale of two elements - chemical evolution of magnesium and europium. , 477(1):1206–1224, June 2018. doi: 10.1093/mnras/sty618.

J. F. Navarro, C. S. Frenk, and S. D. M. White. A Universal Density Profile from Hierarchical Clustering. *The Astrophysical Journal*, 490(2):493–508, Dec. 1997. doi: 10.1086/304888.

D. Nelson, A. Pillepich, V. Springel, R. Weinberger, L. Hernquist, R. Pakmor, S. Genel, P. Torrey, M. Vogelsberger, G. Kauffmann, F. Marinacci, and J. Naiman. First results from the IllustrisTNG simulations: the galaxy colour bimodality. , 475(1):624–647, Mar. 2018. doi: 10.1093/mnras/stx3040.

D. Nelson, A. Pillepich, V. Springel, R. Pakmor, R. Weinberger, S. Genel, P. Torrey, M. Vogelsberger, F. Marinacci, and L. Hernquist. First results from the TNG50 simulation: galactic outflows driven by supernovae and black hole feedback. , 490(3): 3234–3261, Dec. 2019. doi: 10.1093/mnras/stz2306.

P. Ocvirk, D. Aubert, J. Chardin, A. Knebe, N. Libeskind, S. Gottlöber, G. Yepes, and Y. Hoffman. High-resolution Simulations of the Reionization of an Isolated Milky Way-M31 Galaxy Pair. *The Astrophysical Journal*, 777(1):51, Nov. 2013. doi: 10.1088/0004-637X/777/1/51.

T. Okamoto, C. S. Frenk, A. Jenkins, and T. Theuns. The properties of satellite galaxies in simulations of galaxy formation. , 406(1):208–222, July 2010. doi: 10.1111/j.1365-2966.2010.16690.x.

Y. Ordenes-Briceño, P. Eigenthaler, M. A. Taylor, T. H. Puzia, K. Alamo-Martínez, K. X. Ribbeck, R. P. Muñoz, H. Zhang, E. K. Grebel, S. Ángel, P. Côté, L. Ferrarese, M. Hilker, A. Lançon, S. Mieske, B. W. Miller, Y. Rong, and R. Sánchez-Janssen. The Next Generation Fornax Survey (NGFS). III. Revealing the Spatial Substructure of the Dwarf Galaxy Population Inside Half of Fornax's Virial Radius. *The Astrophysical Journal*, 859(1):52, May 2018. doi: 10.3847/1538-4357/aaba70.

V. Pandya, R. S. Somerville, D. Anglés-Alcázar, C. C. Hayward, G. L. Bryan, D. B. Fielding, J. C. Forbes, B. Burkhart, S. Genel, L. Hernquist, C.-G. Kim, S. Tonnesen,

and T. Starkenburg. First Results from SMAUG: The Need for Preventative Stellar Feedback and Improved Baryon Cycling in Semianalytic Models of Galaxy Formation. *The Astrophysical Journal*, 905(1):4, Dec. 2020. doi: 10.3847/1538-4357/abc3c1.

H. Parkinson, S. Cole, and J. Helly. Generating dark matter halo merger trees. , 383(2): 557–564, Jan. 2008. doi: 10.1111/j.1365-2966.2007.12517.x.

S. Paudel, R. Smith, P.-A. Duc, P. Côté, J.-C. Cuillandre, L. Ferrarese, J. P. Blakeslee, A. Boselli, M. Cantiello, S. D. J. Gwyn, P. Guhathakurta, S. Mei, J. C. Mihos, E. W. Peng, M. Powalka, R. Sánchez-Janssen, E. Toloba, and H. Zhang. The Next Generation Virgo Cluster Survey. XXII. Shell Feature Early-type Dwarf Galaxies in the Virgo Cluster. *The Astrophysical Journal*, 834(1):66, Jan. 2017. doi: 10.3847/1538-4357/834/1/66.

M. S. Pawlowski, B. Famaey, H. Jerjen, D. Merritt, P. Kroupa, J. Dabringhausen, F. Lüghausen, D. A. Forbes, G. Hensler, F. Hammer, M. Puech, S. Fouquet, H. Flores, and Y. Yang. Co-orbiting satellite galaxy structures are still in conflict with the distribution of primordial dwarf galaxies. , 442(3):2362–2380, Aug. 2014. doi: 10.1093/mnras/stu1005.

J. Peñarrubia, J. F. Navarro, and A. W. McConnachie. The Tidal Evolution of Local Group Dwarf Spheroidals. *The Astrophysical Journal*, 673(1):226–240, Jan. 2008. doi: 10.1086/523686.

S. Pearson, A. M. Price-Whelan, D. W. Hogg, A. C. Seth, D. J. Sand, J. A. S. Hunt, and D. Crnojevic. Mapping Dark Matter with Extragalactic Stellar Streams: the Case of Centaurus A. *arXiv e-prints*, art. arXiv:2205.12277, May 2022.

E. W. Peng, H. C. Ford, and K. C. Freeman. The Globular Cluster System of NGC 5128. II. Ages, Metallicities, Kinematics, and Formation. *The Astrophysical Journal*, 602(2): 705–722, Feb. 2004a. doi: 10.1086/381236.

E. W. Peng, H. C. Ford, and K. C. Freeman. The Globular Cluster System of NGC 5128. II. Ages, Metallicities, Kinematics, and Formation. *The Astrophysical Journal*, 602(2): 705–722, Feb. 2004b. doi: 10.1086/381236.

S. Perlmutter, G. Aldering, G. Goldhaber, R. A. Knop, P. Nugent, P. G. Castro, S. Deustua, S. Fabbro, A. Goobar, D. E. Groom, I. M. Hook, A. G. Kim, M. Y. Kim, J. C. Lee, N. J. Nunes, R. Pain, C. R. Pennypacker, R. Quimby, C. Lidman, R. S. Ellis, M. Irwin, R. G. McMahon, P. Ruiz-Lapuente, N. Walton, B. Schaefer, B. J. Boyle, A. V. Filippenko, T. Matheson, A. S. Fruchter, N. Panagia, H. J. M. Newberg, W. J. Couch, and T. S. C. Project. Measurements of Ω and Λ from 42 High-Redshift Supernovae. *The Astrophysical Journal*, 517(2):565–586, June 1999. doi: 10.1086/307221.

A. Pillepich, D. Nelson, L. Hernquist, V. Springel, R. Pakmor, P. Torrey, R. Weinberger, S. Genel, J. P. Naiman, F. Marinacci, and M. Vogelsberger. First results from the

IllustrisTNG simulations: the stellar mass content of groups and clusters of galaxies. , 475(1):648–675, Mar. 2018a. doi: 10.1093/mnras/stx3112.

A. Pillepich, V. Springel, D. Nelson, S. Genel, J. Naiman, R. Pakmor, L. Hernquist, P. Torrey, M. Vogelsberger, R. Weinberger, and F. Marinacci. Simulating galaxy formation with the IllustrisTNG model. , 473(3):4077–4106, Jan. 2018b. doi: 10.1093/mnras/stx2656.

A. Pillepich, D. Nelson, V. Springel, R. Pakmor, P. Torrey, R. Weinberger, M. Vogelsberger, F. Marinacci, S. Genel, A. van der Wel, and L. Hernquist. First results from the TNG50 simulation: the evolution of stellar and gaseous discs across cosmic time. , 490(3):3196–3233, Dec. 2019. doi: 10.1093/mnras/stz2338.

Planck Collaboration, N. Aghanim, Y. Akrami, M. Ashdown, J. Aumont, C. Baccigalupi, M. Ballardini, A. J. Banday, R. B. Barreiro, N. Bartolo, S. Basak, R. Battye, K. Benabed, J. P. Bernard, M. Bersanelli, P. Bielewicz, J. J. Bock, J. R. Bond, J. Borrill, F. R. Bouchet, F. Boulanger, M. Bucher, C. Burigana, R. C. Butler, E. Calabrese, J. F. Cardoso, J. Carron, A. Challinor, H. C. Chiang, J. Chluba, L. P. L. Colombo, C. Combet, D. Contreras, B. P. Crill, F. Cuttaia, P. de Bernardis, G. de Zotti, J. Delabrouille, J. M. Delouis, E. Di Valentino, J. M. Diego, O. Doré, M. Douspis, A. Ducout, X. Dupac, S. Dusini, G. Efstathiou, F. Elsner, T. A. Enßlin, H. K. Eriksen, Y. Fantaye, M. Farhang, J. Fergusson, R. Fernandez-Cobos, F. Finelli, F. Forastieri, M. Frailis, A. A. Fraisse, E. Franceschi, A. Frolov, S. Galeotta, S. Galli, K. Ganga, R. T. Génova-Santos, M. Gerbino, T. Ghosh, J. González-Nuevo, K. M. Górski, S. Gratton, A. Gruppuso, J. E. Gudmundsson, J. Hamann, W. Handley, F. K. Hansen, D. Herranz, S. R. Hildebrandt, E. Hivon, Z. Huang, A. H. Jaffe, W. C. Jones, A. Karakci, E. Keihänen, R. Keskitalo, K. Kiiveri, J. Kim, T. S. Kisner, L. Knox, N. Krachmalnicoff, M. Kunz, H. Kurki-Suonio, G. Lagache, J. M. Lamarre, A. Lasenby, M. Lattanzi, C. R. Lawrence, M. Le Jeune, P. Lemos, J. Lesgourgues, F. Levrier, A. Lewis, M. Liguori, P. B. Lilje, M. Lilley, V. Lindholm, M. López-Caniego, P. M. Lubin, Y. Z. Ma, J. F. Macías-Pérez, G. Maggio, D. Maino, N. Mandolesi, A. Mangilli, A. Marcos-Caballero, M. Maris, P. G. Martin, M. Martinelli, E. Martínez-González, S. Matarrese, N. Mauri, J. D. McEwen, P. R. Meinhold, A. Melchiorri, A. Mennella, M. Migliaccio, M. Millea, S. Mitra, M. A. Miville-Deschênes, D. Molinari, L. Montier, G. Morgante, A. Moss, P. Natoli, H. U. Nørgaard-Nielsen, L. Pagano, D. Paoletti, B. Partridge, G. Patanchon, H. V. Peiris, F. Perrotta, V. Pettorino, F. Piacentini, L. Polastri, G. Polenta, J. L. Puget, J. P. Rachen, M. Reinecke, M. Remazeilles, A. Renzi, G. Rocha, C. Rosset, G. Roudier, J. A. Rubiño-Martín, B. Ruiz-Granados, L. Salvati, M. Sandri, M. Savelainen, D. Scott, E. P. S. Shellard, C. Sirignano, G. Sirri, L. D. Spencer, R. Sunyaev, A. S. Suur-Uski, J. A. Tauber, D. Tavagnacco, M. Tenti, L. Toffolatti, M. Tomasi, T. Trombetti, L. Valenziano, J. Valiviita, B. Van Tent, L. Vibert, P. Vielva, F. Villa, N. Vittorio, B. D. Wandelt, I. K. Wehus, M. White, S. D. M. White, A. Zacchei, and A. Zonca. Planck 2018 results. VI. Cosmological parameters. , 641:A6, Sept. 2020. doi: 10.1051/0004-6361/201833910.

W. H. Press and P. Schechter. Formation of Galaxies and Clusters of Galaxies by Self-

Similar Gravitational Condensation. *The Astrophysical Journal*, 187:425–438, Feb. 1974. doi: 10.1086/152650.

Y. Qin, A. R. Duffy, S. J. Mutch, G. B. Poole, A. Mesinger, and J. S. B. Wyithe. Dark-ages Reionization and Galaxy Formation Simulation â€“ XV. Stellar evolution and feedback in dwarf galaxies at high redshift. *Monthly Notices of the Royal Astronomical Society*, 487(2):1946–1963, 05 2019. ISSN 0035-8711. doi: 10.1093/mnras/stz1380. URL `https://doi.org/10.1093/mnras/stz1380`.

J. C. Richardson, M. J. Irwin, A. W. McConnachie, N. F. Martin, A. L. Dotter, A. M. N. Ferguson, R. A. Ibata, S. C. Chapman, G. F. Lewis, N. R. Tanvir, and R. M. Rich. PAndAS' Progeny: Extending the M31 Dwarf Galaxy Cabal. *The Astrophysical Journal*, 732(2):76, May 2011. doi: 10.1088/0004-637X/732/2/76.

M. Ricotti and N. Y. Gnedin. Formation Histories of Dwarf Galaxies in the Local Group. *The Astrophysical Journal*, 629(1):259–267, Aug. 2005. doi: 10.1086/431415.

M. Ricotti, O. H. Parry, and N. Y. Gnedin. A common origin for globular clusters and ultra-faint dwarfs in simulations of the first galaxies. *The Astrophysical Journal*, 831 (2):204, 2016.

M. Ricotti, E. Polisensky, and E. Cleland. Ghostly stellar haloes and their relationship to ultra-faint dwarfs. *Monthly Notices of the Royal Astronomical Society*, 2022.

A. G. Riess, A. V. Filippenko, P. Challis, A. Clocchiatti, A. Diercks, P. M. Garnavich, R. L. Gilliland, C. J. Hogan, S. Jha, R. P. Kirshner, B. Leibundgut, M. M. Phillips, D. Reiss, B. P. Schmidt, R. A. Schommer, R. C. Smith, J. Spyromilio, C. Stubbs, N. B. Suntzeff, and J. Tonry. Observational Evidence from Supernovae for an Accelerating Universe and a Cosmological Constant. *The Astronomical Journal*, 116(3):1009–1038, Sept. 1998. doi: 10.1086/300499.

M. Rocha, A. H. G. Peter, and J. Bullock. Infall times for Milky Way satellites from their present-day kinematics. , 425(1):231–244, Sept. 2012. doi: 10.1111/j.1365-2966.2012.21432.x.

Y. Rong, T. H. Puzia, P. Eigenthaler, Y. Ordenes-Briceño, M. A. Taylor, R. P. Muñoz, H. Zhang, G. Galaz, K. Alamo-Martínez, K. X. Ribbeck, E. K. Grebel, S. Ángel, P. Côté, L. Ferrarese, M. Hilker, S. Mieske, B. W. Miller, R. Sánchez-Janssen, and E. J. Johnston. The Next Generation Fornax Survey (NGFS). VI. The Alignment of Dwarf Galaxies in the Fornax Cluster. *The Astrophysical Journal*, 883(1):56, Sept. 2019. doi: 10.3847/1538-4357/ab3725.

V. C. Rubin and J. Ford, W. Kent. Rotation of the Andromeda Nebula from a Spectroscopic Survey of Emission Regions. *The Astrophysical Journal*, 159:379, Feb. 1970. doi: 10.1086/150317.

V. C. Rubin, J. Burley, A. Kiasatpoor, B. Klock, G. Pease, E. Rutscheidt, and C. Smith. Kinematic studies of early-type stars. I. Photometric survey, space motions, and comparison with radio observations. *The Astronomical Journal*, 67:491–531, Oct. 1962. doi: 10.1086/108758.

E. Sacchi, H. Richstein, N. Kallivayalil, R. van der Marel, M. Libralato, P. Zivick, G. Besla, T. M. Brown, Y. Choi, A. Deason, T. Fritz, M. Geha, P. Guhathakurta, M. Jeon, E. Kirby, S. R. Majewski, E. Patel, J. D. Simon, S. Tony Sohn, E. Tollerud, and A. Wetzel. Star Formation Histories of Ultra-faint Dwarf Galaxies: Environmental Differences between Magellanic and Non-Magellanic Satellites? , 920(1):L19, Oct. 2021. doi: 10.3847/2041-8213/ac2aa3.

D. J. Sand, D. Crnojević, J. Strader, E. Toloba, J. D. Simon, N. Caldwell, P. Guhathakurta, B. McLeod, and A. C. Seth. Discovery of a New Faint Dwarf Galaxy Associated with NGC 253. , 793(1):L7, Sept. 2014. doi: 10.1088/2041-8205/793/1/L7.

I. M. E. Santos-Santos, L. V. Sales, A. Fattahi, and J. F. Navarro. Satellite mass functions and the faint end of the galaxy mass-halo mass relation in LCDM. , July 2022. doi: 10.1093/mnras/stac2057.

T. Sawala, C. Scannapieco, and S. White. Local Group dwarf galaxies: nature and nurture. , 420(2):1714–1730, Feb. 2012. doi: 10.1111/j.1365-2966.2011.20181.x.

T. Sawala, C. S. Frenk, A. Fattahi, J. F. Navarro, T. Theuns, R. G. Bower, R. A. Crain, M. Furlong, A. Jenkins, M. Schaller, and J. Schaye. The chosen few: the low-mass haloes that host faint galaxies. , 456(1):85–97, Feb. 2016. doi: 10.1093/mnras/stv2597.

P. L. Schechter. New axes for the fundamental plane. *arXiv e-prints*, art. arXiv:1508.02358, Aug. 2015.

A. Schneider and R. Teyssier. A new method to quantify the effects of baryons on the matter power spectrum. , 2015(12):049–049, Dec. 2015. doi: 10.1088/1475-7516/2015/12/049.

M. E. Sharina, I. D. Karachentsev, A. E. Dolphin, V. E. Karachentseva, R. B. Tully, G. M. Karataeva, D. I. Makarov, L. N. Makarova, S. Sakai, E. J. Shaya, E. Y. Nikolaev, and A. N. Kuznetsov. Photometric properties of the Local Volume dwarf galaxies. , 384 (4):1544–1562, Mar. 2008. doi: 10.1111/j.1365-2966.2007.12814.x.

S. Shen, H. J. Mo, S. D. M. White, M. R. Blanton, G. Kauffmann, W. Voges, J. Brinkmann, and I. Csabai. The size distribution of galaxies in the Sloan Digital Sky Survey. , 343(3):978–994, Aug. 2003. doi: 10.1046/j.1365-8711.2003.06740.x.

Y. Shi, G. Helou, L. Yan, L. Armus, Y. Wu, C. Papovich, and S. Stierwalt. Extended Schmidt Law: Role of Existing Stars in Current Star Formation. *The Astrophysical Journal*, 733(2):87, June 2011. doi: 10.1088/0004-637X/733/2/87.

N. Shipp, N. Panithanpaisal, L. Necib, R. Sanderson, D. Erkal, T. S. Li, I. B. Santistevan, A. Wetzel, L. R. Cullinane, A. P. Ji, S. E. Koposov, K. Kuehn, G. F. Lewis, A. B. Pace, D. B. Zucker, J. Bland-Hawthorn, E. C. Cunningham, S. Y. Kim, S. Lilleengen, J. Moreno, and S. Sharma. Streams on FIRE: Populations of Detectable Stellar Streams in the Milky Way and FIRE. *arXiv e-prints*, art. arXiv:2208.02255, Aug. 2022.

J. D. Simon. The Faintest Dwarf Galaxies. , 57:375–415, Aug. 2019. doi: 10.1146/annurev-astro-091918-104453.

S. J. Smartt. Progenitors of Core-Collapse Supernovae. , 47:63–106, Sept. 2009. doi: 10.1146/annurev-astro-082708-101737.

R. Smith, R. Sánchez-Janssen, M. Fellhauer, T. H. Puzia, J. A. L. Aguerri, and J. P. Farias. The impact of galaxy harassment on the globular cluster systems of early-type cluster dwarf galaxies. , 429(2):1066–1079, Feb. 2013. doi: 10.1093/mnras/sts395.

R. Smith, H. Choi, J. Lee, J. Rhee, R. Sanchez-Janssen, and S. K. Yi. The Preferential Tidal Stripping of Dark Matter versus Stars in Galaxies. *The Astrophysical Journal*, 833(1):109, Dec. 2016. doi: 10.3847/1538-4357/833/1/109.

D. Sobral, I. Smail, P. N. Best, J. E. Geach, Y. Matsuda, J. P. Stott, M. Cirasuolo, and J. Kurk. A large Hα survey at z = 2.23, 1.47, 0.84 and 0.40: the 11 Gyr evolution of star-forming galaxies from HiZELS. , 428(2):1128–1146, Jan. 2013. doi: 10.1093/mnras/sts096.

R. S. Somerville and R. Davé. Physical Models of Galaxy Formation in a Cosmological Framework. , 53:51–113, Aug. 2015. doi: 10.1146/annurev-astro-082812-140951.

R. S. Somerville and T. S. Kolatt. How to plant a merger tree. , 305(1):1–14, May 1999. doi: 10.1046/j.1365-8711.1999.02154.x.

R. S. Somerville and J. R. Primack. Semi-analytic modelling of galaxy formation: the local Universe. , 310(4):1087–1110, Dec. 1999. doi: 10.1046/j.1365-8711.1999.03032.x.

A. Sorgho, T. Foster, C. Carignan, and L. Chemin. A 5^{deg} x 5^{deg} deep H I survey of the M81 group. , 486(1):504–522, June 2019. doi: 10.1093/mnras/stz696.

G. Soucail, B. Fort, Y. Mellier, and J. P. Picat. A blue ring-like structure in the center of the A 370 cluster of galaxies. , 172:L14–L16, Jan. 1987.

L. R. Spitler, A. J. Romanowsky, J. Diemand, J. Strader, D. A. Forbes, B. Moore, and J. P. Brodie. Evidence for inhomogeneous reionization in the local Universe from metal-poor globular cluster systems. , 423(3):2177–2189, July 2012. doi: 10.1111/j.1365-2966.2012.21029.x.

V. Springel. The cosmological simulation code GADGET-2. , 364(4):1105–1134, Dec. 2005. doi: 10.1111/j.1365-2966.2005.09655.x.

V. Springel, S. D. M. White, A. Jenkins, C. S. Frenk, N. Yoshida, L. Gao, J. Navarro, R. Thacker, D. Croton, J. Helly, J. A. Peacock, S. Cole, P. Thomas, H. Couchman, A. Evrard, J. Colberg, and F. Pearce. Simulations of the formation, evolution and clustering of galaxies and quasars. , 435(7042):629–636, June 2005. doi: 10.1038/nature03597.

V. Springel, J. Wang, M. Vogelsberger, A. Ludlow, A. Jenkins, A. Helmi, J. F. Navarro, C. S. Frenk, and S. D. M. White. The Aquarius Project: the subhaloes of galactic haloes. , 391(4):1685–1711, Dec. 2008. doi: 10.1111/j.1365-2966.2008.14066.x.

V. Springel, R. Pakmor, A. Pillepich, R. Weinberger, D. Nelson, L. Hernquist, M. Vogelsberger, S. Genel, P. Torrey, F. Marinacci, and J. Naiman. First results from the IllustrisTNG simulations: matter and galaxy clustering. , 475(1):676–698, Mar. 2018. doi: 10.1093/mnras/stx3304.

E. Starkenburg, A. Helmi, G. De Lucia, Y.-S. Li, J. F. Navarro, A. S. Font, C. S. Frenk, V. Springel, C. A. Vera-Ciro, and S. D. M. White. The satellites of the Milky Way - insights from semi-analytic modelling in a ΛCDM cosmology. , 429(1):725–743, Feb. 2013. doi: 10.1093/mnras/sts367.

X.-n. Sun, R.-z. Yang, B. Mckinley, and F. Aharonian. Giant lobes of Centaurus A as seen in radio and γ-ray images obtained with the Fermi-LAT and Planck satellites. , 595:A29, Oct. 2016. doi: 10.1051/0004-6361/201629069.

G. A. Tammann. Dwarf Galaxies in the Past. In *European Southern Observatory Conference and Workshop Proceedings*, volume 49 of *European Southern Observatory Conference and Workshop Proceedings*, page 3, Jan. 1994.

M. A. . Taylor, , , , and j. . i. k. . . y. . . m. . v. . . n. . . p. . . d. . . a. . . e. . . p. . . a. . . a. . . , title = "".

M. A. Taylor, R. P. Muñoz, T. H. Puzia, S. Mieske, P. Eigenthaler, and M. S. Bovill. The Survey of Centaurus A's Baryonic Structures (SCABS). I. Survey Description and Initial Source Catalogues. *arXiv e-prints*, art. arXiv:1608.07285, Aug. 2016.

M. A. Taylor, T. H. Puzia, R. P. Muñoz, S. Mieske, A. Lançon, H. Zhang, P. Eigenthaler, and M. S. Bovill. The Survey of Centaurus A's Baryonic Structures (SCABS) - II. The extended globular cluster system of NGC 5128 and its nearby environment. , 469(3):3444–3467, Aug. 2017. doi: 10.1093/mnras/stx1021.

M. A. Taylor, P. Eigenthaler, T. H. Puzia, R. P. Muñoz, K. X. Ribbeck, H.-X. Zhang, Y. Ordenes-Briceño, and M. S. Bovill. A Collection of New Dwarf Galaxies in NGC 5128's Western Halo. , 867(1):L15, Nov. 2018. doi: 10.3847/2041-8213/aae88d.

A. A. Thoul and D. H. Weinberg. Hydrodynamic Simulations of Galaxy Formation. II. Photoionization and the Formation of Low-Mass Galaxies. *The Astrophysical Journal*, 465:608, July 1996. doi: 10.1086/177446.

J. Tinker, A. V. Kravtsov, A. Klypin, K. Abazajian, M. Warren, G. Yepes, S. Gottlöber, and D. E. Holz. Toward a Halo Mass Function for Precision Cosmology: The Limits of Universality. *The Astrophysical Journal*, 688(2):709–728, Dec. 2008. doi: 10.1086/591439.

G. Torrealba, V. Belokurov, S. E. Koposov, K. Bechtol, A. Drlica-Wagner, K. A. G. Olsen, A. K. Vivas, B. Yanny, P. Jethwa, A. R. Walker, T. S. Li, S. Allam, B. C. Conn, C. Gallart, R. A. Gruendl, D. J. James, M. D. Johnson, K. Kuehn, N. Kuropatkin, N. F. Martin, D. Martinez-Delgado, D. L. Nidever, N. E. D. Noël, J. D. Simon, G. S. Stringfellow, and D. L. Tucker. Discovery of two neighbouring satellites in the Carina constellation with MagLiteS. , 475(4):5085–5097, Apr. 2018. doi: 10.1093/mnras/sty170.

G. Torrealba, V. Belokurov, S. E. Koposov, T. S. Li, M. G. Walker, J. L. Sanders, A. Geringer-Sameth, D. B. Zucker, K. Kuehn, N. W. Evans, and W. Dehnen. The hidden giant: discovery of an enormous Galactic dwarf satellite in Gaia DR2. , 488(2):2743–2766, Sept. 2019. doi: 10.1093/mnras/stz1624.

M. Trenti, B. D. Smith, E. J. Hallman, S. W. Skillman, and J. M. Shull. How Well do Cosmological Simulations Reproduce Individual Halo Properties? *The Astrophysical Journal*, 711(2):1198–1207, Mar. 2010. doi: 10.1088/0004-637X/711/2/1198.

F. van de Rydt, S. Demers, and W. E. Kunkel. Pheonix: an Intermediate Dwarf Galaxy in the Local Group. *The Astronomical Journal*, 102:130, July 1991. doi: 10.1086/115861.

S. van den Bergh. The galaxies of the Local Group. *Cambridge Astrophysics Series*, 35, Jan. 2000a.

S. van den Bergh. *The Galaxies of the Local Group*. 2000b.

F. C. van den Bosch and G. Ogiya. Dark matter substructure in numerical simulations: a tale of discreteness noise, runaway instabilities, and artificial disruption. , 475(3):4066–4087, Apr. 2018. doi: 10.1093/mnras/sty084.

A. Venhola, R. Peletier, E. Laurikainen, H. Salo, E. Iodice, S. Mieske, M. Hilker, C. Wittmann, M. Paolillo, M. Cantiello, J. Janz, M. Spavone, R. D'Abrusco, G. van de Ven, N. Napolitano, G. Verdoes Kleijn, M. Capaccioli, A. Grado, E. Valentijn, J. Falcón-Barroso, and L. Limatola. The Fornax Deep Survey (FDS) with VST. VI. Optical properties of the dwarf galaxies in the Fornax cluster. , 625:A143, May 2019. doi: 10.1051/0004-6361/201935231.

M. Vogelsberger, S. Genel, V. Springel, P. Torrey, D. Sijacki, D. Xu, G. Snyder, S. Bird, D. Nelson, and L. Hernquist. Properties of galaxies reproduced by a hydrodynamic simulation. , 509(7499):177–182, May 2014. doi: 10.1038/nature13316.

D. A. Wake, M. Franx, and P. G. van Dokkum. Which galaxy property is the best indicator of its host dark matter halo properties? *arXiv e-prints*, art. arXiv:1201.1913, Jan. 2012.

D. Walsh, R. F. Carswell, and R. J. Weymann. 0957+561 A, B: twin quasistellar objects or gravitational lens? , 279:381–384, May 1979. doi: 10.1038/279381a0.

S. M. Walsh, H. Jerjen, and B. Willman. A Pair of Boötes: A New Milky Way Satellite. , 662(2):L83–L86, June 2007. doi: 10.1086/519684.

J. Wang, F. Hammer, M. Rejkuba, D. Crnojević, and Y. Yang. A recent major merger tale for the closest giant elliptical galaxy Centaurus A. , 498(2):2766–2777, Oct. 2020. doi: 10.1093/mnras/staa2508.

S. Weerasooriya, M. S. Bovill, A. Benson, A. M. Musick, and M. Ricotti. Devouring the Milky Way Satellites: Modeling Dwarf Galaxies with Galacticus. *The Astrophysical Journal*, 948(2):87, May 2023. doi: 10.3847/1538-4357/acc32b.

S. Weerasooriya, M. S. Bovill, M. Taylor, and A. Benson. Curious Case of Centaurus A: What Happened to Missing Satellites within 200 kpc. *The Astrophysical Journal*, b.

S. Weerasooriya, M. S. Bovill, M. Taylor, and A. Benson. Devouring the Centaurus A Satellites: Modeling Dwarf Galaxies with Galacticus. *The Astrophysical Journal*, in prep. a.

R. Weinberger, V. Springel, L. Hernquist, A. Pillepich, F. Marinacci, R. Pakmor, D. Nelson, S. Genel, M. Vogelsberger, J. Naiman, and P. Torrey. Simulating galaxy formation with black hole driven thermal and kinetic feedback. , 465(3):3291–3308, Mar. 2017. doi: 10.1093/mnras/stw2944.

D. R. Weisz, A. E. Dolphin, E. D. Skillman, J. Holtzman, K. M. Gilbert, J. J. Dalcanton, and B. F. Williams. The Star Formation Histories of Local Group Dwarf Galaxies. II. Searching For Signatures of Reionization. *The Astrophysical Journal*, 789(2):148, July 2014. doi: 10.1088/0004-637X/789/2/148.

D. R. Weisz, A. E. Dolphin, E. D. Skillman, J. Holtzman, K. M. Gilbert, J. J. Dalcanton, and B. F. Williams. The Star Formation Histories of Local Group Dwarf Galaxies. III. Characterizing Quenching in Low-mass Galaxies. *The Astrophysical Journal*, 804(2): 136, May 2015. doi: 10.1088/0004-637X/804/2/136.

D. R. Weisz, N. F. Martin, A. E. Dolphin, S. M. Albers, M. L. M. Collins, A. M. N. Ferguson, G. F. Lewis, D. Mackey, A. McConnachie, R. M. Rich, and E. D. Skillman. Comparing the Quenching Times of Faint M31 and Milky Way Satellite Galaxies. , 885(1):L8, Nov. 2019. doi: 10.3847/2041-8213/ab4b52.

A. Wetzel, C. C. Hayward, R. E. Sanderson, X. Ma, D. Angles-Alcazar, R. Feldmann, T. K. Chan, K. El-Badry, C. Wheeler, S. Garrison-Kimmel, F. Nikakhtar, N. Panithanpaisal, A. Arora, A. B. Gurvich, J. Samuel, O. Sameie, V. Pandya, Z. Hafen, C. Hummels, S. Loebman, M. Boylan-Kolchin, J. S. Bullock, C.-A. Faucher-Giguere, D. Keres, E. Quataert, and P. F. Hopkins. Public data release of the FIRE-2 cosmological zoom-in simulations of galaxy formation. *arXiv e-prints*, art. arXiv:2202.06969, Feb. 2022.

C. Wheeler, P. F. Hopkins, A. B. Pace, S. Garrison-Kimmel, M. Boylan-Kolchin, A. Wetzel, J. S. Bullock, D. Kereš, C.-A. Faucher-Giguère, and E. Quataert. Be it therefore resolved: cosmological simulations of dwarf galaxies with 30 solar mass resolution. , 490(3):4447–4463, Dec. 2019. doi: 10.1093/mnras/stz2887.

S. D. M. White and C. S. Frenk. Galaxy Formation through Hierarchical Clustering. *The Astrophysical Journal*, 379:52, Sept. 1991. doi: 10.1086/170483.

S. D. M. White and M. J. Rees. Core condensation in heavy halos: a two-stage theory for galaxy formation and clustering. , 183:341–358, May 1978. doi: 10.1093/mnras/183.3.341.

A. B. Whiting, M. J. Irwin, and G. K. T. Hau. A new galaxy in the local group: The antlia dwarf galaxy. , 114:996–1001, Sept. 1997. doi: 10.1086/118530.

M. I. Wilkinson, J. T. Kleyna, G. F. Gilmore, N. W. Evans, A. Koch, E. K. Grebel, R. F. G. Wyse, and D. R. Harbeck. Probing the Dark Matter Content of Local Group Dwarf Spheroidal Galaxies with FLAMES. *The Messenger*, 124:25, June 2006.

B. Willman, F. Governato, J. J. Dalcanton, D. Reed, and T. Quinn. The observed and predicted spatial distribution of Milky Way satellite galaxies. , 353(2):639–646, Sept. 2004. doi: 10.1111/j.1365-2966.2004.08095.x.

B. Willman, M. R. Blanton, A. A. West, J. J. Dalcanton, D. W. Hogg, D. P. Schneider, N. Wherry, B. Yanny, and J. Brinkmann. A New Milky Way Companion: Unusual Globular Cluster or Extreme Dwarf Satellite? , 129(6):2692–2700, June 2005. doi: 10.1086/430214.

J. Wolf, G. D. Martinez, J. S. Bullock, M. Kaplinghat, M. Geha, R. R. Muñoz, J. D. Simon, and F. F. Avedo. Accurate masses for dispersion-supported galaxies. , 406(2):1220–1237, Aug. 2010. doi: 10.1111/j.1365-2966.2010.16753.x.

K. A. Woodley, W. E. Harris, M. A. Beasley, E. W. Peng, T. J. Bridges, D. A. Forbes, and G. L. H. Harris. The Kinematics and Dynamics of the Globular Clusters and Planetary Nebulae of NGC 5128. , 134(2):494–510, Aug. 2007. doi: 10.1086/518788.

J. Zhang, O. Fakhouri, and C.-P. Ma. How to grow a healthy merger tree. , 389(4):1521–1538, Oct. 2008. doi: 10.1111/j.1365-2966.2008.13671.x.

D. B. Zucker, V. Belokurov, N. W. Evans, J. T. Kleyna, M. J. Irwin, M. I. Wilkinson, M. Fellhauer, D. M. Bramich, G. Gilmore, H. J. Newberg, B. Yanny, J. A. Smith, P. C. Hewett, E. F. Bell, H. W. Rix, O. Y. Gnedin, S. Vidrih, R. F. G. Wyse, B. Willman, E. K. Grebel, D. P. Schneider, T. C. Beers, A. Y. Kniazev, J. C. Barentine, H. Brewington, J. Brinkmann, M. Harvanek, S. J. Kleinman, J. Krzesinski, D. Long, A. Nitta, and S. A. Snedden. A Curious Milky Way Satellite in Ursa Major. , 650(1):L41–L44, Oct. 2006a. doi: 10.1086/508628.

D. B. Zucker, V. Belokurov, N. W. Evans, M. I. Wilkinson, M. J. Irwin, T. Sivarani, S. Hodgkin, D. M. Bramich, J. M. Irwin, G. Gilmore, B. Willman, S. Vidrih, M. Fellhauer, P. C. Hewett, T. C. Beers, E. F. Bell, E. K. Grebel, D. P. Schneider, H. J. Newberg, R. F. G. Wyse, C. M. Rockosi, B. Yanny, R. Lupton, J. A. Smith, J. C. Barentine, H. Brewington, J. Brinkmann, M. Harvanek, S. J. Kleinman, J. Krzesinski, D. Long, A. Nitta, and S. A. Snedden. A New Milky Way Dwarf Satellite in Canes Venatici. , 643(2):L103–L106, June 2006b. doi: 10.1086/505216.

F. Zwicky. Die Rotverschiebung von extragalaktischen Nebeln. *Helvetica Physica Acta*, 6:110–127, Jan. 1933.

VITA

Sachi Weerasooriya was born March 11th, 1994, in Kandy, Sri Lanka. She is the youngest daughter of Wijeratne Weerasooriya and Muthumenike Kulasekare. A 2013 graduate of Hillwood College Kandy, Sri Lanka. She received a Bachelor of Science degree with a double major in Mathematics and Physics from Midwestern State University, Wichita Falls in 2018. She completed a Master of Science in physics with a concentration in Astrophysics from Texas Christian University, Fort Worth in 2020. In August, 2018, she enrolled in graduate study at Texas Christian University, and is working towards her doctorate in Astronomy. Since August, 2018, she has been an teaching assistant in Astronomy and Physics.

Personal Background	Sachi Weerasooriya Fort Worth, TX Daughter of Wijeratne and Muthumenike Weerasooriya
Education	Advanced Level, Hillwood College, Kandy, Sri Lanka, 2013 Bachelor of Science, Physics and Mathematics, Midwestern State University,Fort Worth,TX,2018 Master of Science, Physics, Texas Christian University, Fort Worth, 2020
Experience	Teaching assistantship, Midwestern State University, Wichita Falls,TX,2015-2018 Math/Physics Tutor, Midwestern State University, Wichita Falls, TX,2015-2018 Teaching assistantship, Texas Christian University, Fort Worth, 2018-2020
Professional Memberships	American Astronomical Society International Students Association (Texas Christian University) International Students Association (Midwestern State University) Sigma Phi Sigma Pi Mu Epsilon

ABSTRACT

MODELING DWARF GALAXIES OF THE LOCAL VOLUME WITH THE SEMI-ANALYTIC MODEL GALACTICUS

by Sachi Weerasooriya, 2023
Department of Physics and Astronomy
Texas Christian University

Major Advisor, Dr. Mia Sauda Bovill, Associate Professor of Astronomy

Dwarf galaxies are ubiquitous and extremely sensitive to various internal and external feedback forms. Thus, studying dwarfs in various environments is critical for understanding galaxy evolution. The best-studied dwarfs are those of the Local Group (LG). The Local Group (LG) is home to some of the best-studied dwarfs, but thanks to recent surveys like SDSS, PAndAS, and DES, we now know of more than twice as many dwarfs as before. Concurrently, the Milky Way satellites have been successfully modeled with simulations (e.g. MINT Justice League, FIRE II); however, at a high computational cost. In this work, we run the Semi-Analytic Model (SAM) Galacticus on a Milky Way analog. We show, for the first time, with correctly chosen astrophysical prescriptions and parameters, Galacticus can reproduce the $z = 0$ properties and star formation histories of the Milky Way dwarfs, including the ultra-faints, allowing efficient modeling of even the faintest dwarfs with minimal computational cost. Recently, surveys such as SCABS and PISCeS have extended our understanding of dwarf satellite systems beyond the LG, such as the Centaurus A (Cen A) elliptical galaxy, which is located 3.8 Mpc away and has a M_{vir} of $10^{13} M_{\odot}$. By applying the same astrophysical assumptions and parameters used in

the Milky Way simulations, we can match the properties of the observed Cen A satellites and reproduce the shape of the Cen A luminosity function at distances beyond 250 kpc. However, our modeled luminosity function cannot replicate the steepening observed at $M_V < -12$ within 200 kpc. This can only be reproduced for higher temperatures of the Inter-Galactic Medium of Cen A system, suggesting it may result from Cen A's AGN.